LARGE EDDY SIMULATION OF TURBULENT DIFFUSION FLAMES AND POOL FIRES

A Thesis Submitted to the Faculty of Technology

of

Kingston University

by

YUN KANG

In Partial Fulfillment of the Requirement for the Degree

of

DOCTOR OF PHILOSOPHY

June 2004

ACKNOWLEDGEMENT

A milestone in my life is reached.

On completing my Ph.D study, I would first like to thank my supervisor, Professor Jennifer Wen, for her continuous support and encouragement throughout my research. I feel extremely fortunate to have had the opportunity to work with Professor Wen during the last five years. Her advice suggestions provide valuable help to me. Other members in the supervision team including Dr. S Lo and Dr. S Dembele have also offered their thoughtful comments on my research.

Many thanks to my colleagues and other supporting staff in the Department of Engineering, Kingston University. They have offered me their kind help, without which I cannot complete my study.

Here I would like to present my special thank to my wife, Xiujie Hou, who has been supporting me all the time with all her love. I have experienced ups and downs during these years and Xiujie accompanies me at every moment. Her understanding and encouragement have made me confident and positive to every difficulty in my study. Also to my parents, thank you for giving me endless support --- I could not have done this without you.

This Ph.D research is in collaboration with the National Institute of Standards and Technology, USA. Dr. K McGrattan and Dr. H Baum from NIST have provided me the LES software package FDS together with advice and suggestions. The discussion and information exchange between us benefit my research very much.

Table of Contents

LIST OF FIGURES

Nomenclatures

General Symbols

C	Smagorinsky constant
D	diffusivity
f	external force (including gravity)
h	enthalpy (J)
M	molecular weight
P	pressure (N/m^2)
P_0	back ground pressure
Pe	Peclet number
$\dot{q}'''$	heat release rate per unit volume (KW/m^3)
R	gas constant
R_e	Reynolds number
R_L	turbulent Reynolds number
r	stoichiometric air-fuel ratio
S	turbulence stress tensor
S_c	Schmidt number
T	temperature (K)
t	time (second)
u,v,w	velocity vectors (m/s)
$\dot{w}$	reaction rate (KW/s)
Y	mass fraction

Greek Symbols

ρ	density (kg/m^3)
ξ	mixture fraction
χ	scalar dissipation rate
τ	turbulent shear stress
μ	viscosity
σ	SGS quantity in momentum conservation equation

κ	SGS quantity in energy conservation equation
ζ	SGS quantity in species conservation equation

Subscripts

SGS	Sub-grid Scale
i,j,k	Cartesian directions
f	fuel
l	species
o	oxidizer
p	product
rad	radiant
st	stoichiometric
t	turbulence

ABSTRACT

KANG, Yun, Ph.D, Kingston University April 2004

Large Eddy Simulation of Turbulent Diffusion Flames and Pool Fires

Director of Study: Professor Jennifer Wen, School of Engineering, Kingston University

Second Supervisor: Dr. Sing Lo, School of Engineering, Kingston University

In this dissertation a study of numerical simulations of turbulent diffusion flames and pool fires is presented. In order to account for the physical coupling of turbulent mixing and combustion, the large eddy simulation (LES) technique is used. The subgrid-scale (SGS) modelling for both turbulence and combustion are examined in details and a modified version of SGS combustion model has been proposed. For SGS turbulence modelling, the dynamic approach is used. This approach allows the model coefficient to be updated temporally and spatially and it can be used to account for the energy back-scattering. For SGS combustion modelling, a conserved scalar approach, namely the laminar flamelet model is used. Due to the tiny scale of combustion, it could be infeasible for modern computers to execute a direct calculation of an industrial combustion application. By treating the fire flame as an assembly of thin flames (flamelets), the laminar flamelet model has managed to separate the chemical reaction from the turbulence mixing. The calculation of laminar flamelet approach is relatively independent of LES. The calculations of turbulence and combustion are interacted by a conserved scalar called mixture fraction.

Contribution has been made by the candidate to the application and optimisations of the SGS models. Those optimisations are based on the applications to pool fires and bluff body flows. In SGS combustion modelling, the variance of mixture fraction and the scalar dissipation rate are modelled from the mixture fraction rather than solving the governing equations. This simplification has dramatically cut the computational expense and has virtually turned the 3-D look-up table to a 1-D format. During the calculation of the heat release rate, the contribution of both reactants and products are considered. For pool fires, the constant thermodynamics pressure is used to effectively establish the relation between the temperature and density fields.

Pool fires with different burner diameters and various types of fuels have been simulated using LES with the above SGS modelling. All cases are studied under 3-D mode. In addition to the analysis of the distribution of mean flow quantities (temperature, density, velocities, etc), considerable effort has been directed towards the study of the time development and the dynamic behaviours. Different characteristics have been identified for medium and small pool fires. The dynamic approach of SGS turbulence modelling has also been applied to the simulation of bluff body flows.

The simulations were carried out using the LES package called Fire Dynamics Simulator (FDS), which is developed by the researchers in the National Institute of Standards and Technology (NIST), U.S.A. During the period of the Ph.D study, the FDS codes were updated several times by both the researchers in NIST and the candidate. The update covers the combustion modelling, radiation modelling, meshing and some other aspects. The simulations were carried out on a single processor Pentium IV PC with 2G-RAM. The number of cells in each simulation was

generally between 1 and 2 million with the finest grid resolution being in the order of millimetre.

The predictions are compared with the experimental measurement and other established simulation data. The ability of capturing the instantaneous flow movement and dealing with realistic geometries has made LES with appropriate SGS modelling an effective and promising tool for the numerical study of turbulence and combustion. The laminar flamelet approach of SGS combustion modelling has established progressive relationship between the modelling of turbulence and the modelling of combustion.

As a recommendation, the extending use of the dynamic approach has been proposed. With more accurate determination of the model coefficient in SGS modelling, LES is expected to cope with even higher Reynolds number flows in more complicated geometries.

Chapter 1 Introduction to CFD & LES of Fires

1.1 Computational Fluid Dynamics (CFD)

For many years, fluid dynamic problems have been widely encountered in many engineering applications including hydraulics, aeronautics, automotive and combustion. In those applications, identification of flow variables is required and is of major importance. A lot of experiments have been carried out, from which many valuable data are obtained. Although the experimental determination is appropriate and effective in some situations, it is difficult to rely on experimental measurement for all laboratory and industrial applications. In most of engineering applications, the major type of fluid motions is turbulent. The flow is regarded as being highly random, unsteady, diffusive, dissipative and three-dimensional [1]. With the limit of current electronic and thermal equipment, it could be unrealistic to get direct measurement in some complicated or large-scale flows. Especially when chemical reaction is involved in the flow, the uncertainties and fast changes in small scales are beyond the range to be captured by the experiments.

With the development of computer technology in the past decades, computational fluid dynamics (CFD) is increasingly becoming a good alternative to obtain flow information and to analyse fluid problems and all the related turbulence aspects. The principle of CFD is based on a set of second-order partial differential equations which govern the flow dynamics.

Conservation of Mass

$$\frac{\partial \rho}{\partial t} + \frac{\partial \rho u}{\partial x_i} = 0 \tag{1}$$

Conservation of Momentum

$$\left(\frac{\partial \rho u}{\partial t} + \frac{\partial (\rho u v)}{\partial x_i} \right) + \frac{\partial p}{\partial x_i} = f + \frac{\partial \tau_{ij}}{\partial x_i} \tag{2}$$

Conservation of Energy

$$\frac{\partial}{\partial t}(\rho h) + \frac{\partial (\rho h u)}{\partial x_i} - \frac{Dp}{Dt} = \dot{q}''' + \frac{\partial}{\partial x_i}(k \frac{\partial T}{\partial x_i}) + \frac{\partial}{\partial x_i}(\sum_l h_l (\rho D)_l \frac{\partial Y_l}{\partial x_i}) \tag{3}$$

Conservation of Species

$$\frac{\partial}{\partial t}(\rho Y_l) + \frac{\partial (\rho Y_l u)}{\partial x_i} = \frac{\partial}{\partial x_i}\left((\rho D)_l \frac{\partial Y_l}{\partial x_i} \right) + \dot{w}_l \tag{4}$$

Equation of State

$$p(t) = \rho T R \sum_l Y_l / M_l \tag{5}$$

The above equations are non-linear, and need various initial or boundary conditions for different applications to start calculation. Each of the above equations is numerically solved to obtain flow variables. However, they are related to each other so the numerical method generally consists of the Runge-Kutta method and evolutional integration. The details of solution procedure vary with different CFD methods and will be discussed in the following text.

The directly numerical solutions to the above equations are theoretically accurate. The only discrepancy comes from the system error or the truncation error of the numerical method. Once appropriate parameters and initial/boundary conditions are given for a certain case, the CFD program starts to run until the solutions from each time step remain almost unchanged. This end is scientifically referred to as "converged". The simulation results are then analysed by comparing with experimental data or previously proved simulation results. If there is no available data to be compared with, the simulation results should be able to describe the flow physics properly. Once the simulation results are found reasonable and grid independent, the CFD program is validated and can be used to predict other scenarios in which experimental information cannot be obtained directly.

Due to the fact that governing equations are solved numerically in CFD, the determination of computational grid resolution places essential impact on the accuracy of predictions. Ideally the computational grid should be smaller than the smallest scale of turbulence motion so that the very details of flow dynamics can be accurately captured. This calculation, however, is not feasible for modern computers due to the large amount of computational expense in most of the industrial applications. Compromising the computational efficiency and the accuracy, several distinct approaches of CFD have been proposed and developed by many researchers. Among them field modelling (traditional CFD), large eddy simulation (LES) and direct numerical simulation (DNS) are discussed in details in following sections.

1.2 Fire Modelling

The idea that the dynamics of a fire might be studied numerically dates back to the beginning of the computer age. Indeed, the fundamental conservation equations governing fluid dynamics heat transfer and combustion were fist written down over a century ago [2]. Compared to the general fluid dynamics, fire scenarios contain more complexity about heat and mass transfer, chemical reaction and product generation. The types of combustion could be various, including pool fires, jet flames, pre-mixed and non pre-mixed combustion, etc. The types of fuel and oxidisers can change in a wide range, giving different physical and chemical characters. The initial and boundary conditions also give determining impacts on the process, intensity and duration of the chemical reactions. Research is still underway to develop more advanced technique to capture the instantaneous information inside the fire flame and plume. However, the involvement of enormous parameters and initial/boundary conditions makes it extremely difficult to find a universal and efficient solver for all fire scenarios.

The general equations of fluid dynamics (equations (1)-(5)) describe a rich variety of physical processes, many of which have nothing to do with fires. In the interests of industrial applications, the equations governing the fluid dynamics in a fire scenario should be simplified to give an efficient calculation. Due to the existence of difficulty in the experimental study of large-scale combustion, computational simulation with numerical modelling is widely adopted as a dominant tool in the fire research. All the modelling methods in the computational simulation are based on the fluid governing equations, with different numerical procedures applied on it. The majority of various models can be summarised into four groups: zone modelling, field modelling, direct numerical simulation (DNS) and large eddy simulation (LES).

1.2.1 Zone Modelling

This mature modelling method is principally used to describe compartment fires. With a relatively simple geometry, each compartment is vertically divided into two zones, each of which is spatially homogenous. The upper layer is referred to as "hot zone" and lower layer as "cool zone". Mass and energy balances are enforced for each layer, with additional models describing other physical processes appended as differential or algebraic equations as appropriate. An excellent description of the physical and mathematical assumptions behind the zone modelling concept is given by Quintiere [3].

The physical and computational simplicity of the zone modelling has led to its widespread use in the analysis of fire scenarios. As long as no details of spatial distribution of physical properties are required, zone modelling reasonably approximates the reality and is acknowledged to be reliable [4]. However, by their nature, zone models cannot capture the physical process associated with the chemical combustion. Rather than as a research tool, zone models have more or less evolved as an enhancing tool used by designers who cannot afford the CPU requirement of other CFD models.

1.2.2 Field Modelling

With the rapid improvement of modern computers and the development of computer fluid dynamics (CFD), field modelling is increasingly applied to fire simulations. Generally speaking, field modelling is based on the Reynolds averaging of fluid governing equations. All the flow variables are time-averaged within a given period,

$$\overline{Q} = \frac{\int^{+\Delta t} Q(t)dt}{\Delta t} \tag{6}$$

For compressible flows, the density weighting applies (referred to as Favre-Averaging),

$$\widetilde{Q} = \frac{\int^{+\Delta t} \rho(t)Q(t)dt}{\int^{+\Delta t} \rho(t)dt} \tag{7}$$

When applied to the governing equations, this averaging process generates significant simplicity in calculation, which makes field modelling suitable for simulations of more complicated geometries and various physical phenomena. The averaged equations are referred to as Reynolds Averaged Navier Stokes (RANS) (no density weighting) or Favre Averaged Navier Stokes (FANS) equations. The time-averaging process generates fluctuation items to close the equations. Those fluctuation items need to be modelled for the numerical solutions.

Pioneered by Launder and Spalding [5] and further developed by Patankar [6], "k - ε" model is one of the typical field models. The "k - ε" model, along with other two-equation models [7], give meaningful and practical simulation results in industrial applications. Those two-equation models are based on the assumption that the turbulent stresses are proportional to the mean velocity gradients (suggested by Boussinesq [8]). Detailed description of two equation models have been given by many researchers [9,10,11].

However, the above two-equations models have been found under-predicting the spreading rate of vertical thermal plumes [12] and over-predicting that for horizontally stratified flows [13]. The reason was that the buoyancy-generated turbulence was insufficiently accounted for in the Simple Gradient Diffusion (SGD) formula or even the Generalised Gradient Diffusion Hypothesis (GGDH) formula embedded in those models [7]. Liu and Wen proposed a four-equation turbulence model that demonstrated the significant effects of turbulence modelling on the simulation of buoyant diffusion flames [7]. This model has partly improved the anisotropy problem encountered by eddy viscosity methods and it has been proved successfully in simulating buoyancy driven cavity flows and buoyant fire plumes [14,15].

As large amount of momentum and kinetic energy is possessed in the large-scale motions, the time averaging of resolved quantities is proved to be accurate enough for many industrial applications. As the instantaneous fluctuation has already been filtered out through averaging, the simulation results from field modelling are generally appeared smoothly, even with the most highly resolved fire simulations. The smallest resolvable length scales are determined by the product of the local velocity and the averaging time, rather than the spatial resolution of the underlying computational grid [2]. This makes it possible to use field models for some high Reynolds-number flows, which are found infeasible to direct numerical simulation.

Unfortunately, the instantaneous changes and the evolution of flow variables are lost inevitably with the time averaging, as is the prediction of local transient phenomena. Some of those instantaneous changes are found of importance in many fires and combustion systems. It is argued that the smooth appearance of simulation results

from field modelling may have lost the fidelity to real scenarios, especially for chemical reactions. Another systematic disadvantage of field modelling is the involvement of many empirical models and constants. The values of those constants are obtained from the statistics of previous sets of experiments, or from the induction of other models. Due to the variety of chemical reactions in both space and time, the single-valued constants are found insufficient to describe various fire scenarios.

1.2.3 Direct Numerical Simulation (DNS)

Opposite to field modelling, direct numerical simulation aims at solving the original governing equations directly and thoroughly. The equations are solved numerically at all levels of scales. It is thought to be the ideal target of computational modelling. In fact, DNS has shown success in simulating some low Reynolds number flows [16,17].

Some advantages of DNS are highlighted here. Firstly, as the equations themselves are theoretically precise, the only error of DNS lies in the truncation error of the numerical method. Secondly, DNS has the mechanism to capture the instantaneous fluctuations of all the variables inside the flow field. Thirdly, during the simulation the parameters can be controlled and adjusted easily and precisely, which is very difficult in experiments. Finally, it can be used for some cases that could not be experimented in reality.

However, the feasibility of DNS is always limited by the capacity of modern computers. There are enormous vortices at different sizes existing in the flow field. As stated before, motions at all length scales need to be solved numerically. The largest scale is normally comparable to the characteristic length L (usually the scale of

computational domain). And the smallest scale is defined as the Kolmogorov scale $\eta = (\nu^3/\varepsilon)^{1/4}$ [18]. It has been proved in turbulence statistics that the total grid number is determined by the turbulent Reynolds number,

$$N \propto \left(\frac{L}{\eta}\right)^3 \propto \mathrm{Re}_L^{9/4} \qquad (8)$$

The computational time required is proportional to $Re_L^{3/4}$, leading to the total calculation expense proportional to $Re_L^{9/4} * Re_L^{3/4} = Re_L^3$. Giving that the completion of a single-cell calculation along one dimension on a $R_L = 5*10^5$ case (which is typical for industrial combustion) needs 100 iterations, the computer has to carry out $100*(5*10^5)^3 = 1.25*10^{19}$ calculations for a 3-D case. It takes about 4 weeks for a fastest computer (around $6*10^{12}$ calculations per second) to complete the above simulation. So it is practically expensive or even infeasible to carry out DNS for most of the industrial flows with high-Reynolds-number. The main purpose of applying DNS on some low Reynolds flows is to provide turbulence details for validating and improving other turbulence models. Detailed discussion on DNS can be found in several review articles by, e.g., Rogallo and Moin [19], Reynolds [20] and Schumann [21].

1.2.4 Large Eddy Simulation (LES)

Large eddy simulation is a technique intermediate between DNS and RANS approaches. All the instantaneous quantities inside the flow are divided into two parts, the large-scale part that can be solved numerically and the sub-grid scale (SGS) part that needs to be modelled,

$$Q = \overline{Q} + Q' \qquad (9)$$

The resolved scale is generated by a filtering process,

$$\overline{Q}(x) = \int_{\Omega} Q(x')G(x,x')dx'$$

$$\widetilde{Q}(x) = \frac{\int_{\Omega} \rho(x')Q(x')G(x,x')dx'}{\int_{\Omega} \rho(x')G(x,x')dx'} \qquad (10)$$

where G(x,x') is the filtering function. Similarly to traditional CFD time averaging, a tilde is used to denote the density weighting.

The accuracy of large eddy simulation relies on the amount of directly solvable scales and the appropriateness of SGS models. Theoretically speaking, the smaller scale it can solve directly, the better prediction is expected. On the other hand, however, the smaller scale it solves, the more computational expenses it requires. So the application of LES is the compromise of computational accuracy and efficiency.

Comparing to DNS, the impressive advantage of LES is that it can be applied to high Reynolds number flows. With the SGS quantities filtered out, the computational expense is reduced to an acceptable level for present computers. It is well believed that turbulence flows are dominated by energy-bearing large eddies. The SGS scales are more homogeneous and more likely to be described by universal models. The accuracy of LES has been proved by many researchers at various applications [19,22-24].

Although filtering process is applied on both RANS approach and LES, there is a systematic difference that needs to be addressed. The filtering process in RANS approaches, generally regarded as time averaging, gives an average of a variable over

a certain period. All the instantaneous information is lost and the result of the filtering does not represent the on-the-spot movement of the flow, which harms the accuracy of the simulation. In LES, an instantaneous fluid motion is regarded as a superimposed outcome of the large scales and the sub-grid scales, both of which represent the instantaneous motion. The flow variable is spatially averaged over the domain.

1.3 Large Eddy Simulation

As stated above, there are two main issues in LES: the filtering process and the SGS modelling.

1.3.1 Filtering Process

The smallest resolvable scale is determined by the filter width Δ. Scales smaller than the filter width are filtered out and need to be modelled. The filtering, indicated by eq. 10, is formally and quite generally expressed by a convolutional integral. Different filtering functions generate different levels of filtering, with different levels of computational complexity and accuracy. It has to be pointed out that although the filter width does not have to be in consistence with the computational cell size, practically the computational cell size should be no larger than the filter width. Detailed discussion of filtering process has been described by Shi [25].

Various filtering functions have been proposed during last 40 years. One of the most popularly used filters is the box filter. The large scale is generated by averaging the instantaneous value over a 3-D domain regulated by Δx_1, Δx_2 and Δx_3,

$$G(x',x)=\begin{cases}\dfrac{1}{\Delta x_1 \Delta x_2 \Delta x_3}, & |x\text{-}x'| \le \Delta x_i/2, \quad i = 1,2,3 \\ 0, & |x\text{-}x'| \ge \Delta x_i/2, \quad i = 1,2,3\end{cases} \tag{11}$$

Box filter is easy to be numerically coded. And it has been proved practically efficient. However, its Fourier transfer has negative values in some regions, which causes computational instability. And due to the inconsistency of filter function at different regions, it is difficult to carry out differentiation at the edge of the box unit.

In the spectra, the box filter can be written as Fourier Truncation Filter by simply cutting off all the waves with an absolute value bigger than K_0. The description of other filtering functions can be referred to Shi [25].

1.3.2 SGS Modelling

After the filtering process being applied to the flow governing equations, the simplified N-S equations are written as following:

Conservation of Mass

$$\frac{\partial \bar{\rho}}{\partial t}+\frac{\partial \bar{\rho}\tilde{u}}{\partial x_i}=0 \tag{12}$$

Conservation of Momentum

$$\left(\frac{\partial \bar{\rho}\tilde{u}}{\partial t}+\frac{\partial(\bar{\rho}\tilde{u}\tilde{v})}{\partial x_i}\right)+\frac{\partial \tilde{p}}{\partial x_i}=\tilde{f}+\frac{\partial \tilde{\tau}_{ij}}{\partial x_i}-\sigma_{ij} \tag{13}$$

Conservation of Energy

$$\frac{\partial}{\partial t}(\overline{\rho}\widetilde{h}) + \frac{\partial(\overline{\rho}\widetilde{h}\widetilde{u})}{\partial x_i} - \frac{D\widetilde{p}}{Dt} = \widetilde{q}''' + \frac{\partial}{\partial x_i}(k\frac{\partial \widetilde{T}}{\partial x_i}) + \frac{\partial}{\partial x_i}(\sum_l \overline{h}_l(\overline{\rho}D)_l \frac{\partial \widetilde{Y}_l}{\partial x_i}) - \kappa_{ij} \tag{14}$$

Conservation of Species

$$\frac{\partial}{\partial t}(\overline{\rho}\widetilde{Y}_l) + \frac{\partial(\overline{\rho}\widetilde{Y}_l\widetilde{u})}{\partial x_i} = \frac{\partial}{\partial x_i}\left((\overline{\rho}D)_l \frac{\partial \widetilde{Y}_l}{\partial x_i}\right) + \widetilde{w}_l - \zeta_{ij} \tag{15}$$

Equation of State

$$\widetilde{p}(t) = \overline{\rho}\widetilde{T}R\sum_l \widetilde{Y}_l / M_l \tag{16}$$

The last items in eqs 13-15 represent the SGS contribution of momentum, energy and mass transfer, respectively. They are added into the equations to keep the system closed.

With the increasing requirement of detailed information about fluid dynamics and structures, the influence of SGS quantities can no longer be neglected. All the SGS items need to be modelled using solved scales and/or some empirical constants,

$$Q' = f(\overline{Q}, c_1, c_2, ...) \tag{17}$$

There are several issues that make the refinement of SGS modelling necessary. Firstly, in the experimental works on some small fires some researchers found that the energy

backscattering from SGS quantities into the main flow is responsible for the discrepancy between traditional simulation results and experimental measurements. Secondly, in 3-D studies, where eddies are affected interactively at all directions, the SGS contribution plays a critical role in balancing the whole system. Finally, when chemical reaction is involved in the flow, the scale of combustion is normally much smaller than the size of a computational cell, which makes it a compulsory requirement to have an appropriate SGS combustion model to describe the reaction process properly.

Since the first SGS turbulence model developed by Smagorinsky in 1963 [26], which was originally used for climate analysis, there have been hundreds of SGS models developed and applied to different applications. Initially started with SGS turbulence models, there is similarity between the construction of SGS turbulence models and other SGS models (energy and mass). In this chapter the varieties of SGS turbulence modelling and SGS combustion modelling are presented.

1.3.2.1 SGS Turbulence Modelling

There are several different types of SGS turbulence models in terms of construction principles. The methods of constructing a SGS model vary in a relatively wide range. In general there are three main streams: eddy viscosity models (EVM), Scale Similarity Models (SSM) and Dynamic Approach.

Eddy Viscosity Models (EVM) are based on a local equilibrium mechanism that on spot inside the flow, there is a balance of molecular diffusion between the resolved scales and the SGS.

The sub-grid scale turbulence stress is given by,

$$\sigma_{ij} = \mu_t \left(\frac{\partial \bar{u}}{\partial x_j} + \frac{\partial \bar{v}}{\partial x_i} \right) \tag{18}$$

In eq. 18, the eddy viscosity μ_t has to be modelled. There are several ways of modelling the eddy viscosity, which will be described later.

It is clearly seen from the mechanism that eddy viscosity models have good behaviours in fully developed turbulence, which has been proved by other researchers [27-29]. While in the laminar or transition regions, where the energy transport is mostly not in an equilibrium state, eddy viscosity models may be inadequate [30].

As most of them are easy to be implemented into numerical codes, eddy viscosity models have been widely used in turbulence analysis and other relative applications. Typical eddy viscosity models include Smagorinsky model [26], Ferziger model [22] and the Gradient model [31,32]. From eq. 18, the difference between those SGS models exists in the modelling of sub-grid scale viscosity μ_t. In the Smagorinsky model,

$$\mu_t = \rho (C_S \Delta)^2 |S| \tag{19}$$

where C_s is the Smagorinsky constant, Δ is the filter width and |S| is a measure of the local strain rate,

$$\Delta = (\Delta x \Delta y \Delta z)^{1/3} \tag{20}$$

$$|S|^2 = 2\left(\frac{\partial \bar{u}}{\partial x}\right)^2 + 2\left(\frac{\partial \bar{v}}{\partial y}\right)^2 + 2\left(\frac{\partial \bar{w}}{\partial z}\right)^2 + \left(\frac{\partial \bar{u}}{\partial y} + \frac{\partial \bar{v}}{\partial x}\right)^2 + \left(\frac{\partial \bar{u}}{\partial z} + \frac{\partial \bar{w}}{\partial x}\right)^2 + \left(\frac{\partial \bar{v}}{\partial z} + \frac{\partial \bar{w}}{\partial y}\right)^2 \quad (21)$$

Another filtering width ($\Delta = \sqrt{\Delta x^2 + \Delta y^2 + \Delta z^2}$) was also tested for comparison but no significant difference had been found [30].

It was found that the Smagorinsky model exhibited better behaviours when the turbulence integration length is less than filter width Δ. To meet the requirement of larger integration length, Ferziger [22] proposed the following modification:

$$\mu_t = C\Delta^{4/3} L^{2/3} \left[\frac{\partial \bar{u}}{\partial x_j} \left(\frac{\partial \bar{u}}{\partial x_j} + \frac{\partial \bar{v}}{\partial x_i} \right) \right]^{1/2} \quad (22)$$

where $L = K^{3/2}\varepsilon^{-1}$ is the characteristic integral length

$K = 0.5(u^2+v^2+w^2)$ is the kinetic energy

$\varepsilon = (u^2+v^2+w^2)^2/2$ is the dissipation rate of K

C is a model constant.

The Gradient model was first proposed by Clark *et al.* [31] and revised by Liu *et al.* [32]:

$$\mu_t = \frac{1}{12}\Delta^2 \left(\frac{\partial \bar{u}}{\partial x_k} \right) \left(\frac{\partial \bar{v}}{\partial x_k} \right) \left(\frac{\partial \bar{u}}{\partial x_j} + \frac{\partial \bar{v}}{\partial x_i} \right)^{-1} \quad (23)$$

It comes from the Taylor expansions of the similarity model ($\sigma_{ij} = \overline{\overline{uv}} - \overline{\overline{u}}\,\overline{\overline{v}}$), which is believed to be less dissipative than EVM.

$$\overline{\overline{uv}} = \overline{\overline{u}}\,\overline{\overline{v}} + \frac{1}{24}\Delta^2 \partial_{kk}(\overline{\overline{uv}}) + O(\Delta^4) \tag{24}$$

$$\overline{\overline{u}} = \overline{u} + \frac{1}{24}\Delta^2 \partial_{kk}\overline{u} + O(\Delta^4) \tag{25}$$

$$\sigma_{ij} = \overline{\overline{uv}} - \overline{\overline{u}}\,\overline{\overline{v}} \approx \frac{1}{12}\Delta^2(\partial_k \overline{u})(\partial_k \overline{v}) \tag{26}$$

This model is chosen because of its higher efficiency in actual simulations when compared to the similarity model [27].

Although they are popularly used in many industrial applications, eddy viscosity models do have some shortcomings. The first one is the dependence on empirical constants. For example, the Smagorinsky constant C_s has been suggested different values for different flows and boundary conditions [22,27,33,34]. Instead of assigning a constant, some dynamic approaches have been developed to determine the coefficient locally[27,35]. Details about dynamic approaches will be discussed later.

Another disadvantage of eddy viscosity models is that they do not have the mechanism to represent the energy backscattering from SGS quantities to the main flow. The eddy viscosity remains positive during the simulation. As a result of that, the simulation predictions with eddy viscosity models usually look too dissipative to the experimental measurement [27,30].

As a proposed solution to the over-dissipation, another mechanism of constructing SGS models called Scale Similarity Models (SSM) is introduced to represent the effect of energy backscattering. Scale similarity models are based on the assumption

that the velocities at different levels of scales give rise to turbulent stresses with similar structure [27]. So one can use the smallest resolved scale to simulate the SGS quantities,

$$\sigma_{ij} = \overline{\overline{uv}} - \overline{\overline{u}}\,\overline{\overline{v}} \tag{27}$$

The SGS stress in the above equation can be either positive or negative, which represent energy entering or coming out from the SGS quantities, respectively. Because the double filtering is significantly more computationally expensive in some cases, it is difficult to apply pure SSM to simulations. Some improvement has been done by other researchers [31,32] and more work is on the way. Another disadvantage of SSM is the computation instability observed (Vreman *et al* [36]).

Some more advanced ways are required for SGS modelling to combine the advantages of EVM and to rectify their shortcomings. The dynamical approach proposed by Germano [37] is believed to be one of them. Prior to the dynamic approach, some researchers suggested a mixed model, simply combining an EVM with a SSM,

$$\sigma_{ij} = \mu_t\left(\frac{\partial \bar{u}}{\partial x_j} + \frac{\partial \bar{v}}{\partial x_i}\right) + \alpha\left(\overline{\overline{uv}} - \overline{\overline{u}}\,\overline{\overline{v}}\right) \tag{28}$$

In eq. 28 α is a coefficient balancing the participation of EVM and SSM in the mixed model. The value of α needs adjustment with different applications. And this model has difficulty in numerical coding.

Finalising the above discussion, an appropriate SGS turbulence model should possess the following characteristics:

1) Universal for different applications (Spatially universal)
2) Suitable for different stages within a reaction (Temporally universal)
3) Able to represent the energy backscattering
4) Numerically stable and minimal systematic error
5) Computationally effective and efficient

Based on Smagorinsky expression, a dynamic approach aiming at solving the above problems was proposed by Germano et al [37]. Similar dynamic approaches have been developed and implemented by many researchers as a solution to the deficiency caused by EVM and SSM [21-24]. In the current Ph.D research, a dynamic approach based on Germano's proposal has been modified and numerically constructed by the author. The details of the numerical procedure are described in Chapter 2, while the application of this dynamic approach is illustrated by a bluff body burner case in Chapter 5.

1.3.2.2 SGS Combustion Modelling

Apart from LES on buoyancy-driven flows, the prediction on fire scenarios is another big issue in the current research. The involvement of chemical reactions increases the complexity and uncertainty inside the flow. Accounting for chemical reactions in LES requires knowledge of the distribution of reactants within each LES grid cell. Inside the reaction zone, the flow characters are dominated by the reaction rate rather than the turbulence mixing. There are many parameters that could affect the reaction rate: physical properties of reactants, concentration of reactants, boundary conditions,

initial conditions, radiation, etc. For example, Sinai [38] has reported the instabilities of pool fires with and without cross-wind. Briefly, there are some distinctive characters of reacting flows that differ them from the non-reacting flows:

1. In the reaction zone, the flow properties are dominated by the chemical reaction rather than by buoyancy. In the fully developed turbulence area, however, the flow is driven by density stratification.

2. There are much more uncertainties lying in the reaction zone.

3. The combustion scale (0.1mm – 1mm) is generally much smaller than the computational grid scale (1mm -- 10mm) currently acceptable by most computers. So it is impossible to solve the combustion scales directly. The combustion has to be modelled.

4. Due to the variety of chemical reactions, mathematical models of the fire process require a wide database for verification and guidance.

Several approaches have been proposed to describe the combustion [2,39-44]. The key issue in combustion modelling is the proper description of the combustion process. As stated above, the combustion scale is one order in magnitude smaller than the computational grid. The direct calculation of combustion is computationally impractical and the chemical reaction needs modelling. Briefly, the following approaches were used for applications in industry and laboratory studies.

Thermal particles

In the early stage of fire simulation, the pool fire was described as an assembly of thermal particles ejecting out of the burner. They were carrying an initial velocity, determined by the heat input rate and the fuel properties. The burn-out time was set for those particles and they vanished after the reaction. At the same time step, the species concentration was then adjusted by the heat release rate [2],

$$Y_i = Y_i + \Delta t * sfac * Q / \rho \tag{29}$$

where Δt is the time step, sfac is a transfer coefficient and Q is the heat release rate assigned by the user.

The big advantage of this approach is the simplicity in the calculation. It was found to be an effective tool to simulate the large-scale fire when the overall distributions of mean quantities (temperature, velocity, etc) are of the main interest of research. However, describing fires as thermal particles inevitably prevents this approach from being used for more detailed research. The reaction rate term in eq. 15 was omitted when solving that equation. The burn-out time sets the life duration of each particles, making it impossible to represent the re-iginition. The ejecting particles are less sensitive to the entrained air, causing the huge discrepancy to the experimental measurement [30].

Arrhenius Law Based On Filtered Quantities

Low Reynolds number, non-premixed combustion is one of the typical types of combustion phenomena. A lot of attention has been paid on the filtered reaction

rate $\overline{\dot{w}}$. The simplest approach is called "Arrhenius law based on filtered quantities" [45], which neglects sub-grid scale contributions.

$$\overline{\dot{w}} = A\overline{\rho}^{2}\overline{Y_i}\overline{Y_o}\overline{T}^{b}\exp(-\frac{E}{R\overline{T}}) \tag{30}$$

where A is the pre-exponential constant, E the activation energy and R the perfect gas constant. This assumption is generally used in the cases where chemical time scale is longer than turbulent time scale [45] (Da<1).

Extension of Favre Average Models

Another simple approach for the reaction rate in non-premixed combustion is the extension of the Magnussen model [45],

$$\overline{\dot{w}} = \alpha\rho\frac{1}{t_{SGS}}\min(Y_f, \frac{Y_o}{r}, \beta\frac{Y_p}{1+r}) \tag{31}$$

where r is the stoichiometric air-fuel ratio. It has to point out that equation 31 is based on the assumption of one-step, irreversible combustion.

Although it looks attractive, such a simple expression may have some deficiencies because of the neglect of so many parameters (type of fuel, boundary conditions, etc.). In practice, eqs. 30 and 31 have not been extensively tested yet.

Linear Eddy Model

A popularly used combustion model in LES is Linear Eddy Model (LEM) [45], which has some characteristics different from other field models:

- The key principle of LEM is to retain the distinction between molecular diffusion and turbulence stirring. The advantages of LEM appear when one wants to get a more efficient study of Schmidt number.

- Molecular diffusion is implemented by the numerical solution of the diffusion equation over the linear domain for each species [46], using Fick's Law:

$$\frac{\partial Y_i}{\partial t} = \rho D \frac{\partial^2 Y_i}{\partial x_i} \tag{32}$$

when used for combustion, a reaction rate should be involved :

$$\frac{\partial Y_i}{\partial t} = \rho D \frac{\partial^2 Y_i}{\partial x_i} + \dot{w}_i''' \tag{33}$$

- Turbulent stirring is represented by the spatial rearrangement of the species field within a specified segment. It is characterised by the spatial position x_0, length of segment l, PDF of length distribution f(l) and rate parameter λ. Values of f(l) and λ for high Reynolds number flows were given by [47]:

$$f(l) = \frac{5}{3} \frac{l^{-\frac{8}{3}}}{\eta^{-\frac{5}{3}} - L^{-\frac{5}{3}}} \tag{34}$$

$$\lambda = \frac{54}{5} \frac{\nu \mathrm{Re}_L}{L^3} \left(\frac{L}{\eta} \right)^{\frac{5}{3}} \tag{35}$$

- The linear eddy model aims at resolving all relevant scales [43]. When applied in LES, only sub-grid scales are involved. Other processes called splicing events are incorporated to represent the convective transport across each grid cell.

- In LES, the domain for LEM is usually chosen as the smallest resolved scale (e.g. a single grid cell). The smallest unresolved length scale is decided by Kolmogorov scale. Thus, the scalar information of LEM can be described with a one-dimensional array of length N [46],

$$N = \frac{L}{\eta} \tag{36}$$

- LEM is generally carried on in one dimension because it is really a time-consuming process. DNS is required within each computational cell.

- As described before, chemical time scale in non-premixed combustion is generally shorter than turbulent mixing time scale, which leads to a much higher frequency of LEM spatial re-arrangement and Fickian diffusion process than the large scales. So it is expected that a number of LEM processes are performed between each time step in LES [47].

Probability Density Function

Another simulation approach for non-premixed combustion is probability density function (PDF), which is under the assumption that the species mass fraction Y_i and the temperature T are functions of passive scalar Z,

$$Z = \frac{\phi \frac{Y_F}{Y_F^{\,0}} - \frac{Y_O}{Y_O^{\,0}} + 1}{\phi + 1} \tag{38}$$

where ϕ is the chemical equivalence ratio,

$$\phi = \frac{rY_F^0}{Y_O^0} \tag{39}$$

When incorporated with Dirac δ-function, the species mass fraction can be expressed as [48],

$$\begin{aligned} Y_F(x,t) &= \int_0^1 Y_F(\psi)\frac{1}{\rho}\int_{-\infty}^{+\infty}\rho(\psi)\delta(Z(x',t)-\psi)G(x-x')dx'd\psi \\ &= \int_0^1 Y_F(\psi)P(\psi,x,t)d\psi \end{aligned} \tag{39}$$

The probability density function P(ψ,x,t) may be either determined by assumption [44] or derived from a transport equation [49]. Little work has been done so far to test the PDF.

Laminar Flamelet Model (LFM)

The principle of LFM is to use a conserved scalar ξ, called mixture fraction, its variance, $\overline{\xi^2}$, and scalar dissipation rate χ to simulate filtered species concentration $\overline{Y_i}$ and reaction rate $\overline{\dot{w}}$. There is some transport equation for filtered species concentration $\overline{Y_i}$ (such as the filtered version of eq. 33). To solve such an equation, the filtered reaction rate $\overline{\dot{w}}$ needs to be modelled.

The mixture fraction ξ and scalar dissipation rate χ are defined as following [50],

$$\xi = \frac{Y_f - \frac{Y_o}{r} + \frac{Y_{o2}}{r}}{Y_{f1} + \frac{Y_{o2}}{r}} \tag{40}$$

$$\chi = \frac{1}{P_e} \nabla \xi \cdot \nabla \xi \tag{41}$$

where subscripts f, o and p represent fuel, oxidizer and product, respectively. Y_{f1} is the species concentration of fuel in the fuel stream and Y_{o2} is the species concentration of oxidizer in the oxidant stream. P_e is the dimensionless Peclet number representing the relative strengths of convection and diffusion. It has to point out that eqs. 40 and 41 are based on two-feed non-premixed combustion with single fuel.

Assuming the flame is locally steady, and that ξ is a monotonic function of the local coordinate normal to the flame, the species concentration of the fuel Y_f can be expressed in terms of ξ. Eqs. 33, 40 and 41 combine to give [50],

$$\chi(\xi, t) \frac{d^2 Y_f}{d\xi^2} = \dot{w}_f \tag{42}$$

Several items in eq. 42 have been neglected when Da >> 1 [50]. From its definition, it is easy to get the following boundary conditions [50],

$$Y_f(\xi, \chi_0)|_{\xi=0} = 0 \tag{43}$$

$$Y_f(\xi, \chi_0)|_{\xi=1} = Y_{f1} \tag{44}$$

The species concentration of oxidizer and product then can be obtained by [51],

$$Y_o = Y_{o2}(1-\xi) + r(Y_f - \xi Y_{f1}) \tag{45}$$

$$Y_p = (r+1)(\xi Y_{f1} - Y_f) \tag{46}$$

Then the filtered quantity is given by [50],

$$\overline{Y_i} = \int Y_i(\xi, \overline{\chi_0}) P(\xi) d\xi \tag{47}$$

where P(ξ) is called probability density function (PDF). Calculation of $\overline{\chi_0}$ (the filtered value of the local peak of χ within the layer χ_0) is described later in Chapter 2. A similar way is applied to obtain $\overline{\dot{w}}$.

In LFM, both $\overline{Y_i}$ and $\overline{\dot{w}}$ are modelled by $\overline{\xi}$, $\overline{\xi^2}$ and $\overline{\chi}$. On the other side, LES is running to get $\overline{\xi}$, $\overline{\xi^2}$ and $\overline{\chi}$. To get the right relations between $\overline{\xi}$, $\overline{\xi^2}$, χ and $\overline{Y_i}$, $\overline{\dot{w}}$, a look-up table has to be constructed before running LES calculation. Details of the construction of a look-up table are presented in Chapter 2.

Mixture fraction model in FDS (Fire Dynamics Simulator)

The mixture fraction combustion model was devised and implemented by the FDS developer McGrattan and his colleagues [2] and thus already embedded in FDS. It is based on the same concept of mixture fraction as defined in eq. 40 and assumes that the chemical reaction is controlled by the mixing process of reactants. However, the governing equation for mixture fraction is written in a more simplified form,

$$\overline{\rho} \frac{D\overline{\xi}}{Dt} = \nabla \cdot \overline{\rho} D \nabla \overline{\xi} \tag{48}$$

Similar to the laminar flamelet approach mentioned earlier, combustion can only take place at the stoichiometric surface. As the model was originally designed for simulating large fires, some simplifications have been applied. Firstly, the combustion

is assumed to be infinitely fast, which means the fuel and oxidiser do not co-exist on the stoichiometric surface. This leads to the "state relation" between the oxygen mass concentration and the mixture fraction [2],

$$Y_o(\xi) = \begin{cases} Y_{o_2}(1 - \dfrac{\xi}{\xi_{st}}) & \xi < \xi_{st} \\ 0 & \xi > \xi_{st} \end{cases} \tag{49}$$

Once the mixture fraction is calculated, the oxygen mass concentration can be determined by eq. 49. Then the mass concentration of fuel and products are obtained accordingly.

Secondly, the SGS term in the governing equation of mixture fraction is omitted. This is believed to be suitable if only the large-scale effect of the combustion is of interest [2]. Finally, the heat release rate is calculated from the oxygen consumption rate following Huggett [52].

$$\dot{q}'''_{ijk} = -\Delta H_o \left. \frac{d\overline{Y_o}}{d\overline{\xi}} \right|_{\xi<\xi_f} \frac{\left(\overline{\rho}D\right)_{i+\frac{1}{2},j,k} \dfrac{\left|\overline{\xi_{i+1,j,k}} - \overline{\xi_{i,j,k}}\right|}{\delta z}}{\delta x \delta y \delta z} \tag{50}$$

1.3.2.3 Summary of SGS modelling

In the large eddy simulation of fire scenarios, the computational effectiveness and efficiency of both SGS turbulence modelling and SGS combustion modelling play determining roles on the quality of simulation results. When the simulation scale of interest becomes smaller and smaller, the importance of SGS modelling has gone far beyond just keeping the governing equations closed. The including of SGS contribution can remedy to some extend the shortcomings brought by the coarse mesh.

As the current capacity of modern computers is hard to cope with the full DNS calculation for high Reynolds number flows, the precision of large eddy simulation relies very much on an appropriate representation of SGS motions. Especially when chemical reaction is involved, the minor scale of combustion makes the modelling a compulsory requirement for the current simulations.

Various approaches of SGS turbulence modelling have been listed in this Chapter. Most of them are using the resolved scale to obtain the SGS quantities. Choosing an adequate SGS model has to consider various parameters such as numerical feasibility, prediction accuracy and computational efficiency. In terms of SGS turbulence modelling, the EVM are good in numerical coding while the SSM possess better mechanism of representing energy backscattering. In the current Ph.D research, the formulation of Smagorinsky model is used due to its numerical efficiency. Effort has been paid for a dynamic approach based on an EVM formulation. The dynamic approach has included some double filtering process that is usually employed in SSM to determine the model coefficient dynamically. Comparing to the EVM, the dynamic approach increases the computational expense but is expected to generate a better model coefficient. The details of constructing the dynamic approach are explained in following chapters.

The SGS combustion modelling adopts a similar formulation as the SGS turbulence modelling. Comparing to the turbulence movement, the tiny scale of combustion brings more difficulties to the modelling. The detailed numerical description of combustion process is not possible due to the number of uncertainties and the high frequency of changes. Furthermore, the interaction between combustion and

turbulence covers different magnitudes of scales, which is extremely difficult for numerical calculation. Some SGS combustion models listed in this Chapter deliberately separate the turbulence and combustion to simplify the calculation. Among them, the laminar flamelet model has been found successful in pool fire simulations.

1.4 Objectives and Structure

Based on the overall understanding of CFD and LES, the main objectives of this dissertation stay in the development and application of SGS modelling in the large eddy simulation on turbulent diffusion flames and pool fires. In nowadays the applications of fire and plumes have been extended to various branches of industry. The numerical simulations on fire and plumes have turned to a compulsory requirement in modern research. Traditional CFD approaches have been gradually proved to lose the advantages with the increasing demand on studying the dynamic behaviours inside the fires. As an enterprising numerical tool, LES has been increasingly acknowledged in the simulations involving combustion. It keeps the numerical calculation while taking into account the SGS contributions. Given a proper mesh resolution, LES could produce reasonably good predictions for some high-Reynolds flows. As the SGS contribution in LES is of critical importance to the accuracy of predictions, the appropriate use and refinement of SGS models could significantly improve the profile of turbulence/combustion modelling.

The main branches of contribution within the current Ph.D research can be summarised as following,

1. Both SGS combustion modelling and SGS turbulence modelling have been systematically studied. Based on the laminar flamelet model [144], some modifications have been applied to make the new combustion model more efficient to simulate pool fires and bluff body jets. The modifications exist in the filtering out of acoustic effects, formation of look-up table and the interaction between turbulence and combustion.

2. The dynamic approach of SGS turbulence modelling has been numerically constructed and applied to the simulation of bluff body fires. The involvement of double-filtering and the third-dimensional average process have improved the prediction accuracy systematically. However, they have also brought difficulties in numerical coding and computational efficiency.

3. The dynamic behaviour together with the statistic characteristics of pool fires have been analysed in details using large eddy simulation. In this dissertation the simulation of pool fires is validated by the experimental data and other established numerical works. During the validation, the advantages of LES over traditional CFD have been highlighted.

4. The application and optimisation of FDS codes have been done in terms of simulating pool fires and bluff body flames. Various types of combustion models, radiation equations and meshing tools have been experienced. The current research has composed a rich bunch of simulation works (which may not be listed in the dissertation in total). The comparison drawn from those simulations has fulfilled the optimisation of a fire-simulating LES package.

Chapter 2 Numerical Modelling

Based on the overview of CFD and LES, the present research focuses on the SGS modelling in LES. The SGS modelling includes the test and validation of existing models, physical analysis of each model, construction and coding of new models and incorporation of new models into existing LES software package. The new models are generally tested and validated by other available simulation results and experimental measurements.

The LES software package used for the simulation was developed by McGrattan and his colleagues at National Institute of Standards and Technology (NIST), U.S.A. The package is called 'Fire Dynamics Simulator' (FDS). It is being tested and validated by users all over the world. It aims to simulate the industrial fire applications at relatively large scales. The governing equations in FDS are based on filtered N-S equations (eqs. 12-15), with some necessary simplifications. The pressure is practically replaced by the background pressure to filter out the acoustic effects and the flow is treated incompressible. The simplified equations, developed by Rehm and Baum [53], have been widely adopted by the larger combustion research community. They are referred to as the "low Mach number" combustion equations.

In FDS, the simplified version of filtered N-S equations (eqs. 12-16) is numerically solved. However, the conservation equation of energy (eq. 14) is not solved directly. Instead, an equation of divergence constraint is calculated,

$$\frac{\partial \tilde{u}}{\partial x_i} = \frac{1}{\overline{\rho} C_p \tilde{T}} \left(\frac{\partial}{\partial x_i} \left(k \frac{\partial \tilde{T}}{\partial x_i} \right) + \frac{\partial}{\partial x_i} \left(\sum h_l \left(\overline{\rho D} \right)_l \frac{\partial \tilde{Y}_l}{\partial x_i} - \frac{\partial \tilde{q}_r}{\partial x_i} + \tilde{q}''' \right) \right) + \left(\frac{1}{\overline{\rho} C_p \tilde{T}} - \frac{1}{\tilde{p}_0} \right) \frac{d\tilde{p}_0}{dt} \qquad (51)$$

The airflow described by those equations is moving at a speed lower than the sound speed. The acoustic effect in the original N-S equations has been filtered out. In FDS, Damköhler number [45] is introduced to identify different types of combustion,

$$D_a = \frac{\tau_t}{\tau_c} \tag{52}$$

Where τ_t is the turbulence time scale and τ_c is the combustion time scale. The Damköhler number compares the different time scales of turbulent mixing and chemical reaction in combustion. In most non-premixed combustion cases, reactions typically take place within thin diffusion zones at a fast rate. The chemical time is much shorter than turbulent time, which leads to Da>>1.

As the diffusion zones where the majority of reaction takes place are usually too thin to be resolved by a LES mesh, combustion needs to be modelled to take into account the distributions of each reactant. Complexity and uncertainty of combustion phenomena make it difficult to construct a proper model for the general use of all types of combustion. However, much work has been done by other researchers for equilibrium chemistry [35,44,54-55] and non-equilibrium chemistry [56-59]. The present study will start with the one-step, irreversible combustion,

$$F + rO \rightarrow (1+r)P \tag{53}$$

with F, O and P representing fuel, oxidiser and product, respectively.

The numerical program is coded by the author using FORTRAN 90. There are two branches of SGS modelling involved in the present research: SGS turbulence modelling and SGS combustion modelling.

2.1 Dynamic Approach in SGS Turbulence Modelling

The details of various SGS turbulence modelling have been described in Chapter 1. The SGS turbulence model adopted in FDS is the Smagorinsky model [26] due to its relatively simple application into real simulations. The model constant C_s is set to 0.17, which is believed to be reasonably good for most of the large fire applications [2]. Some comparative tests have been carried out by the author on buoyancy driven flows with different values of C_s, ranging from 0.1 to 0.2. No significant difference has been found in terms of the predictions on main flow characters (temperature, velocity, etc.). Following this, the constant for the Smagorinsky model is set to 0.17 for all cases in the dissertation where the model is used.

As stated in Chapter 1, however, the systematic shortcomings of Smagorinsky model bring out the necessity of improvement on SGS turbulence modelling. The insufficiency of representing energy backscattering makes the Smagorinsky model (and other EVM) too dissipative for the prediction on laminar/transition flows. And the constant coefficient is found inadequate for various flows or even for the same flow with time-changing conditions. Based on the formation of Smagorinsky model, Germano *et al* proposed a dynamic approach for the determination of model coefficient (named "G4 closure" in his paper [37]). This dynamical approach is based on the combination of SSM and EVM. However, it is not as simple as a pure "add-

together". The format of the dynamical approach comes from the EVM, with a double filtering process applied, which is similar to that in the SSM.

The dynamical approach aims to determine the value of model coefficient instantaneously using the smallest resolved quantities. As stated in Chapter 1, a double-filtering process is applied in the dynamical approach. In LES, the large-scale (numerically resolved) quantities are obtained by the convolution of the velocity and pressure fields with a filter function. In the dynamical approach, two different filtering operators are defined: one is the grid filter $\overline{G}$, denoted by an overbar. The integral is carried out over the entire computational domain. The other is usually called the test filter $\widetilde{G}$, denoted by a tilde,

$$\widetilde{Q}(x) = \int Q(x')\widetilde{G}(x,x')dx' \tag{54}$$

The test filter width is usually larger than that of the grid filter. Different ratios of the two filter widths ($\alpha = \frac{\widetilde{\Delta}}{\Delta}$) were examined and simulation results at $\alpha = 2$ were found in best agreement with the experimental measurements [37].

Practically, the double filtering process can be implemented by $\widetilde{\overline{G}} = \overline{G}\widetilde{G}$ [37].

Similar to the SGS stress term in LES ($\tau_{ij} = \overline{u_i u_j} - \overline{u}_i \overline{u}_j$), the SGS stress term after applying the double filtering process $\widetilde{\overline{G}}$ to the original Navier – Stokes equations is written as,

$$T_{ij} = \widetilde{u_i u_j} - \widetilde{\overline{u}}_i \widetilde{\overline{u}}_j \tag{55}$$

The resolved turbulent stress is defined as,

$$L_{ij} = \widetilde{\overline{u}_i \overline{u}_j} - \widetilde{\overline{u}}_i \widetilde{\overline{u}}_j \tag{56}$$

Combining eqs 55 and 56 results in following algebraic relation [60],

$$L_{ij} = T_{ij} - \widetilde{\tau}_{ij} \tag{57}$$

According to its definition, the resolved turbulence stress L_{ij} represents the contribution to the Reynolds stress by the scales whose length is intermediate between the grid filter width and the test filter width. The advantage of introducing L_{ij} is that it can be calculated directly.

As already used in LES, the Smagorinsky model for the grid-filtering SGS stress is written as,

$$\tau_{ij} - (\frac{\delta_{ij}}{3})\tau_{kk} \approx m_{ij} = -2C\overline{\Delta}^2 \left|\overline{S}\right| \overline{S_{ij}} \tag{58}$$

Similar to it, the test-filtering SGS stress is modelled as,

$$T_{ij} - (\frac{\delta_{ij}}{3})T_{kk} \approx M_{ij} = -2C\widetilde{\overline{\Delta}}^2 \left|\widetilde{\overline{S}}\right| \widetilde{\overline{S}}_{ij} \tag{59}$$

Combining eqs. 58 & 59 and contracting $\overline{S_{ij}}$ on both sides, eq. 57 is re-written as,

$$L_{ij}\overline{S}_{ij} = -2C\left(\widetilde{\overline{\Delta}}^2 \left|\widetilde{\overline{S}}\right| \widetilde{\overline{S}}_{ij}\overline{S}_{ij} - \overline{\Delta}^2 \left|\widetilde{\overline{S}}\right| \widetilde{\overline{S}}_{ij}\overline{S}_{ij}\right) \tag{60}$$

In eq. 60 C is a function of location (x,y,z) and time t. $\overline{S}_{ij}$ is introduced to ensure the calculation stability.

However, it has been found in calculation that the quantities inside the parentheses in eq. 60 could become zero, which makes the coefficient C indeterminate or ill-conditioned. Therefore, C is determined by carrying out a Eulerian average process for eq. 60 along the third direction, in which all the variables are assumed to be homogeneous,

$$C(x,y,z,t) = -\frac{1}{2}\frac{\left\langle L_{kl}\overline{S}_{kl}\right\rangle}{\widetilde{\overline{\Delta}}^2\left\langle\left|\widetilde{\overline{S}}\right|\widetilde{\overline{S}}_{mn}\overline{S}_{mn}\right\rangle - \overline{\Delta}^2\left\langle\left|\widetilde{\overline{S}}\right|\widetilde{\overline{S}}_{pq}\overline{S}_{pq}\right\rangle} \tag{61}$$

The above dynamic approach (known as "G4 closure" in the LES society) is based on the Smagorinsky formulation, but allows for temporal and spatial variability of the coefficient. It has been used to compute high Reynolds number channel flows [61], buoyancy-driven flows [62-64], turbulent recirculating flows [65] and stratified Ekman layer flows [66]. Moin *et al.* [67] have also extended it to compressible flows.

Initially the application of G4 approach was obstructed by its complexity of computation. It needs double-filtering within each time step and the coupling iteration between governing equations. Some simplified models have been proposed for particular applications [48,68]. The difference on the computational efficiency is obvious. The usage of dynamic approach should be the compromise of accuracy requirement and computational efficiency. On the view of future development, however, dynamic approach is believed to be the ultimate solution for SGS turbulence

stress in LES. In the present research, the applications of the dynamic approach are described in following Chapters.

2.2 SGS Combustion Modelling

2.2.1 Laminar Flamelet Model

In the laminar flamelet model, the calculation of SGS combustion (referred to as "LFM calculation") is relatively independent from the LES calculation. A look-up table that relates the species concentrations to the mixture fraction is constructed in the LFM calculation. Once the instantaneous mixture fraction and other parameters are determined in the LES calculation, the corresponding species concentrations could be obtained from the look-up table. The detailed numerical procedure of constructing a look-up table is described below.

I. Choose values of $\bar{\xi}$, $\overline{\xi^2}$, $\bar{\chi}$ as inputs.

II. Calculate F(ξ) and P(ξ) using the following equations,

$$F(\xi)=\exp\{-2[erf^{-1}(2\xi-1)]^2\} \tag{62}$$

$$P(\xi)=\frac{\xi^{a-1}(1-\xi)^{b-1}}{B(a,b)}, \qquad a=\bar{\xi}\left[\frac{\bar{\xi}(1-\bar{\xi})}{\xi_v^{\,2}}-1\right],$$

$$b=\frac{a}{\bar{\xi}}-a, \qquad \xi_v^{\,2}=\overline{\xi^2}-\bar{\xi}^2 \tag{63}$$

III. The local peak of χ can be expressed as [51],

$$\chi = \chi_0 F(\xi) \tag{64}$$

The filtered value of the local peak of χ within the layer χ_0 $\left(\chi_{0\min} \le \chi_0 \le \chi_{0\max}\right)$ is obtained by [50],

$$\overline{\chi_0} = \frac{\overline{\chi}}{\int_0^1 F(\xi) P(\xi) d\xi} \tag{65}$$

IV. Replace χ by $\overline{\chi_0} F(\xi)$ in eq. 42 and use the boundary conditions in eqs. 43 and 44 to get $Y_f(\xi, \overline{\chi_0})$. Please note that reaction rate in eq 42 is based on Arrhenius expression in eq 30.

V. Use eq. 47 to get filtered value $\overline{Y_f}(\overline{\xi}, \overline{\xi^2}, \overline{\chi})$.

VI. Construct the look-up table by repeat steps I-V for the full range of $\overline{\xi}$, $\overline{\xi^2}$, $\overline{\chi}$ as expected by LES.

In compressible flows, one has to take into account the variance of density and temperature. For most of combustion, the Mach number is low, yet the density may vary due to heat release other than flow velocity. In low Mach flows, the state equation for ideal gas can be simplified as [51],

$$p^{(0)} = \rho T \tag{66}$$

The first-order of thermodynamic pressure $P^{(0)}$ is expected to remain constant in space and time if the combustion takes place in an open domain [51,69]. In such a regime, a relation can be established between T, ρ and Y_f, ξ. Full description can be found in [51]. Instead of solving eq. (14) directly, the temperature is linked to Y_f and ξ by,

$$T = \left[T_1 - T_2 + \frac{(\gamma - 1)}{\gamma} h_f \right] \cdot \xi + T_2 - \frac{(\gamma - 1)}{\gamma} h_f \cdot Y_f \tag{67}$$

The methodology for compressible flows is listed blow [50],

I-V. The same as steps I-V for incompressible flows

VI. Insert LFM solution $\overline{Y_f}(\overline{\xi}, \overline{\xi^2}, \overline{\chi})$ into eq. 67 to get the temperature.

VII. Use eq. 66 to get density.

VIII. With ρ and P(ξ) known, a Favre-filtered process is applied to re-calculate $\widetilde{\xi}, \widetilde{\xi}^2$,

$$\widetilde{\xi} = \frac{\int \rho \cdot \overline{\xi} \cdot P(\xi) d\xi}{\int \rho \cdot P(\xi) d\xi} \tag{68}$$

$$\widetilde{\xi}^2 = \frac{\int \rho \cdot \overline{\xi^2} \cdot P(\xi) d\xi}{\int \rho \cdot P(\xi) d\xi} \tag{69}$$

IX. Repeat steps I-V using $\widetilde{\xi}, \widetilde{\xi}^2$ to get the tabulated value $\overline{Y_f}(\widetilde{\xi}, \widetilde{\xi}^2, \overline{\chi})$

X. Repeat steps I-IX for a full range of $\overline{\xi}$, $\overline{\xi^2}$, $\overline{\chi}$ as expected by LES.

Various modifications of LFM have been proposed in recent years [61, 70,71] including the modifications on the definition of mixture fraction [70], the calculation of scalar dissipation rate [61] and the conditional source term in the governing equation of mixture fraction [72]. However, these modifications would inevitably increase the computational expense. As the boundary conditions of the pool fires and the bluff-body flames in current research are well defined and the flow structure is usually stable, the original form of LFM is believed to produce sufficient accuracy.

2.2.2 Modified Laminar Flamelet Model

The SGS combustion model employed in the present research is called "modified laminar flamelet model (MLFM)". It is based on the theory of laminar flamelet model . When put into numerical programming, the LFM has been modified to make the SGS combustion model more efficient for the pool fire simulations. The major modifications can be briefed as following:

1) As the laminar flamelet approach is interacting with the SGS turbulence calculation in LES, some simplifications made in FDS codes are accepted in the LFM calculation as well. For example, the acoustic effect has been filtered out.

2) The combustion dealt with in FDS is assumed infinitely fast, which causes it impossible for the fuel and oxidant to co-exist on the spot of combustion [12]. Although the laminar flamelet model has been extended to cope with premixed and equilibrium combustion [50,51,69], in the current research it has been modified to solve the non-premixed, "fast", irreversible reactions as they are typical in pool fires.

3) In the current research, energy is calculated according to eq. 66. To take into account the effect of the radiant heat loss, eq. 66 is modified as,

$$T = \left[T_1 - T_2 + \frac{(\gamma - 1)}{\gamma} h_f \right] \cdot \xi + T_2 - \frac{(\gamma - 1)}{\gamma} h_f \cdot Y_f + \Delta T_{rad} \qquad (70)$$

Where ΔT_{rad} represents temperature change due to radiative heat loss and its calculation will be described later in the paper. When using eq. 70 to calculate the flow temperature, the computational time is reduced without impacting the simulation quality.

4) Some simplifications are introduced to the governing equation of the mixture fraction to further increase computational efficiency. As stated in LFM calculation, $\bar{\xi}$, $\overline{\xi^2}$, $\bar{\chi}$ are chosen as inputs. As stated in Chapter 1, $\bar{\xi}$, $\overline{\xi^2}$, $\bar{\chi}$ are obtained from LES calculation. $\bar{\xi}$ is obtained through its transport equation,

$$\frac{\partial \bar{\rho}\bar{\xi}}{\partial t} + \frac{\partial (\bar{\rho}\bar{\xi}\bar{u})}{\partial x_i} = \frac{1}{\mathrm{Re}\, Sc} \frac{\partial}{\partial x_i} \left(\mu \frac{\partial \bar{\xi}}{\partial x_i} \right) + \zeta_\xi \qquad (71)$$

In eq. 71 ζ_ξ represents the sub-grid scale quantities,

$$\zeta_\xi = \frac{\partial}{\partial x_i}(\overline{\rho\xi u} - \overline{\rho\xi}\,\overline{u}) \tag{72}$$

In analogue to SGS turbulence modelling, the transport equation of mixture fraction is re-written as follows. Here the modelled turbulent viscosity μ_t is used to replace μ and therefore includes the contribution from SGS term ζ_ξ.

$$\frac{\partial \overline{\rho}\overline{\xi}}{\partial t} + \frac{\partial(\overline{\rho}\overline{\xi}\overline{u})}{\partial x_i} = \frac{1}{\mathrm{Re}\,Sc}\frac{\partial}{\partial x_i}\left(\mu_t \frac{\partial \overline{\xi}}{\partial x_i}\right) \tag{73}$$

$\overline{\xi^2}$ can be obtained either by solving a transport equation [51] or by modelling [73]. In the present study, the following model is used to get $\overline{\xi^2}$.

$$\overline{\xi^2} = \overline{\xi}^2 + C_\xi \overline{\rho}\Delta^2 \nabla\overline{\xi}\cdot\nabla\overline{\xi} \tag{74}$$

where C_ξ is a model constant and Δ is the filtered length in LES.

Generally, $\overline{\chi}$ is obtained by modelling [50,51,73]. The present investigation uses the following model [73],

$$\overline{\chi} = \left(\frac{\mu}{Pe} + \frac{\mu_t}{Sc_t}\right)\left(\frac{\partial \overline{\xi}}{\partial x_i}\right)^2 \tag{75}$$

As both $\overline{\xi^2}$ and $\overline{\chi}$ can be obtained from the derivative of $\overline{\xi}$, the originally 3-D look-up table in LFM calculation could be mapped to a 1-D look-up table.

The species concentration can be located by the mixture fraction only. This simplification brings significant advantages in computational efficiency.

2.3 Radiation

Another important issue in SGS modelling is the proper description of radiative heat loss. In fire applications, part of the heat generated by the chemical process is lost by radiation. The determination of the amount of radiation loss plays a critical role in the prediction on heat and energy transfer of a fire scenario. The radiation calculation in FDS has experienced a series of improvement. In the earlier version of FDS, a constant fraction of 35% was simply used to account for the radiation loss. This approximation did make contribution to the simplification of the whole calculation. However, it had been found inappropriate for an advanced simulation. The radiation percentage is a function of fuel properties, boundary conditions, combustion process and the reaction time. The heat may be absorbed by the soot and/or the surrounding walls. Depending on the reference temperature, the absorption rate to the wall varies. In certain cases the heat is released back to the flow from the wall if the main flow experiences a quick temperature drop (for example, fire extinguishment).

The constant ratio of radiative heat loss was later replaced by a simple radiation transport algorithm that uses randomly chosen rays between radiation sources and targets, a method commonly known as "ray tracing". This method has two major problems. This first is that in this method only the fire itself radiates. There is no wall-to-wall or wall-to-gas radiative heat transfer. Secondly, the method becomes computationally expensive when the fire begins to occupy a large fraction of the space.

In the latest version of FDS, a set of Radiation Transport Equations (RTE) are employed to represent the radiation part. The radiation transport equation (RTE) for a non-scattering gas is,

$$s \cdot \nabla I_{\lambda}(x,s) = k(x,\lambda)[I_b(x) - I(x,s)] \tag{76}$$

where $I_\lambda(x,s)$ is the radiation intensity at wavelength λ. $I_b(x)$ is the source term given by the Planck Function, s is the unit normal direction vector and k(x) is the absorption coefficient. The above spectral dependence is difficult to be solved accurately in practical simulations since the number of wavelengths could not go infinitely. Instead, the radiation spectrum is divided into a relatively small number of bands, in which the most important bands of CO_2 and H_2O are supposed to be accurately represented. The band specific RTE's are now,

$$s \cdot \nabla I_n(x,s) = K_n(x)[I_{b,n}(x) - I(x,s)], \quad n = 1,\ldots, N \tag{77}$$

where n represents the integration over band n. The total intensity is calculated by summing over all the bands,

$$I(x,s) = \sum_{n=1}^{N} I_n(x,s) \tag{78}$$

It was found from a series of experiments that six bands (N=6) are usually sufficient for numerical solution. The increase of band number (N) will significantly increase the computational expense. In fact, even with a reasonably small number of bands, the solution of N RTEs is very time-consuming.

For the cases in which soot is the most important factor controlling the thermal radiation from the fire and hot smoke, it is possible to assume that the gas behaves as a grey medium. As the radiation spectrum of soot is continuous, the spectral dependence is lumped into one absorption coefficient (N=1) and the source term is given by the blackbody radiation intensity,

$$I_b(x) = \sigma T(x)^4 / \pi \tag{79}$$

The band-mean absorption coefficient, K_n, is calculated in FDS by a narrow-band model RADCAL. The boundary condition for the radiation intensity laving a grey diffuse wall is given as,

$$Iw(s) = \varepsilon I_{bw} + \frac{1-\varepsilon}{\pi} \int_{s' \cdot n_w < 0} I_w(s') |s' \cdot n_w| d\Omega \tag{80}$$

where $I_w(s)$ is the intensity at the wall, ε is the emissivity, and I_{bw} is the black body intensity at the wall.

The one-band radiation transport equation is solved using a technique called Finite Volume Method (FVM). So the radiate loss term in the energy equation is,

$$-\nabla \cdot q_r(x) = \kappa(x)[U(x) - 4\pi I_b(x)], \qquad U(x) = \int_{4\pi} I(x,s) d\Omega$$

$$\Delta T_{rad} = \frac{-q_r(x)}{C_p} \tag{81}$$

The assumption of "grey medium" in the above solution is believed to cover most of the fuels in large and medium scale combustion. In optically thin flames, however, where the amount of soot is small compared to the amount of CO_2 and water, it may

produce significant over-prediction of the emitted radiation. The total heat source is then revised by deducting the radiation loss.

Although the pool fires and bluff body flame in current research could be regarded as medium/small fires, the chosen fuels are thought to be sooty. So the RTEs are used for all the simulations stated in the following chapters. It has been found that the RTEs are suitable for the applications considered here hence no modification has made to them.

2.4 Summary of Modelling

The numerical procedure of constructing SGS models has been introduced above. Based on the combination of EVM and SSM, a dynamic approach of SGS turbulence modelling was coded. The involvement of double filtering enables instantaneous update of the SGS turbulence model coefficient. The increase of computational expense could be compensated by the improvement of prediction accuracy. To perform a large eddy simulation of combustion, the SGS combustion model needs to be implemented into the existing codes. Arrhenius expression in eq. 30 and the extension of the Magnussen model in eq. 31 are easy to be programmed although their accuracy may not be good enough. LEM with the aid of PDF is quite a good way but computationally expensive. With a look-up table prepared, LFM is expected to produce a higher efficiency than LEM. The full operation of LFM, of course, needs the combination of Arrhenius expression and PDF.

Chapter 3 Medium Pool Fires

3.1 Introduction

Dynamic behaviours of buoyant jets/plumes and diffusion flames are of importance in many engineering applications such as combustors, cooling systems of energy conversion devices and the exhaust of aeroplanes, and in natural phenomena such as accidental fires and release of buoyant gases in industry from exhaust stacks. It is well known that such flow systems exhibit a periodic oscillatory behaviour close to their origin, often referred to in the literature as "puffing" [74-77]. These periodic oscillations result in the formation and shedding of large-scale (of the order of the plume/burner diameter) vertical structures at a short distance from the burner surface. It is believed that these structures have significant influence on the air entrainment, turbulence mixing, combustion efficiency, flame height and external radiation field and as a result they modify the downstream flame behaviour [38,74,78].

Most early works (prior to 1960) on buoyant plumes were conducted in the fully turbulent far field. From 1960s to the 1980s, Gebhart and co-workers [79] have pioneered the study of buoyant plume/jet instabilities and flow transitions in wall-bounded and unbounded buoyant flows. More recently, these phenomena have been experimentally investigated by Cetegen and co-workers for buoyant plumes [78], and by Weckman and Sobiesiak [76], Cegen and Ahmed [74], Malalasekera *et al* [77], Hamins et al. [75] and Mandin and Most [80] for buoyant diffusion flames and pool fires. Reviews on pool fire pulsation, flame and plume structures can be found in Pagni [81] and Joulain [82]. These earlier investigations have led to the development of

correlations that relates oscillation frequency to the convection time scale for the flame. Utilising the experimental data of Hamins et al. [75], Delichatsios [83] has given an explanation of the different frequency scaling for non-reacting plumes and pool fires based purely on dimensional analysis. But the mechanism involving this instability does not seem to be completely understood [83]. This is partly because experimental measurements are difficult for tracing time histories of all the flow variables and the coupling between buoyancy and the fully 3-D vortex dynamics.

Theoretical analysis of the instability of plumes and flames in the literature is scarce [77]. Buckmaster and Peters [84] predicted buoyancy-driven instability of an idealised planar flame sheet and obtained oscillation frequencies of comparable magnitude to the experiment. Davis *et al.* [85] conducted direct numerical simulation (DNS) of an axis-symmetric, low-speed propane-air jet diffusion flame and showed that both flame flicker and double-peaked temperature profiles were closely associated with buoyancy-induced vortices outside the flame surface. Their model, however, predicted a faster development of the inner and outer vortex structures than experimental observation. Blunsdon et al. [86] used the RANS based CFD approach to simulate the transient behaviour of buoyant turbulent diffusion flames. They considered a flame above a honeycomb mesh, and assigned 'inlet' values (to those quantities) that were thought to be rather high [38] and the results did not capture the large, toroidal vortices that were closely related to puffing. The recent CFD simulation of Sinai [38] did not assume any extraneous supply of turbulence energy at the pool and captured the torodial vortices at a frequency that agreed to experiments but the predicted temperature was found to decay too slowly with height. Ghoniem et al. [87] conducted vortex-based simulation of an axis-symmetric fire plume and their

analysis suggested that puffing results from an intrinsic flow instability which was a Kelvin-Helmholtz type mechanism is associated with the formation of an axis-symmetric vortex sheet along the boundary between the inner hot mixture and the outer colder gases. Mell et al. [88] and Jiang and Luo [89] carried out DNS on axis-symmetric and planar plumes. But similar to the vortex-based study of Ghoniem et al. [87], the applications of the simulations were limited by the 2-D characteristics of the calculations. More recently, Jiang and Luo have successfully applied DNS to 3-D calculations with encouraging results [90]. As experimentally observed, fire plumes are not truly axially symmetric [91]. Furthermore, DNS is still limited to small Reynolds numbers and the RANS or FANS based approaches are unable to simulate the interaction between the many length and time scales which exist in turbulent reacting flows [92]. Large eddy simulation (LES) is a promising alternative, which is computationally less expensive than DNS, but still capable of tackling the scale-dependent dynamic behaviour. Baum et al. [93] conducted LES of fire plumes with the fire itself prescribed as an ensemble of thermal elements ejecting from the burning surface at an initial velocity and radiation prescribed as a fixed percentage heat loss. In a later publication [94], a grey-gas P1 approximation for the radiation transport equation (RTE) has been implemented. Zhou et al. [95] also performed LES of reacting jet plumes. Although the exploratory studies [87,89,95] have captured some important dynamics of reacting plumes, further studies including quantitative comparison with experimental data is desirable to enhance our confidence of the numerical models.

In this chapter the research aims at using LES to gain insight of the underlying physical and chemical processes associated with the periodic instability of small to medium-scale pool fires and their structures. The LES based Fire Dynamics Simulator

(FDS) is used while a modified laminar flamelet model (MLFM) is adopted to model the combustion. As the main interest is to obtain the inside profile of medium pool fire flow field and to test and validate the SGS combustion model, a constant-coefficient (C_s=0.17) Smagorinsky model is chosen as the SGS turbulence model. Simulations have been conducted for several laboratory-tested pool fires. Comparisons with published data as well as some established correlations are presented.

3.2 Numerical Modelling

3.2.1 Governing Equations

The fluid flow is controlled by the Navier-Stokes equations governing the conservation of continuity, mass, momentum and energy transfer. The governing equations used in LES are the filtered and simplified expression of those equations (eqs. 12-16). The scales smaller than the filter width have been "filtered out" resulting in that only large scales remain to be solved numerically. Some sub-grid scale (SGS) models representing the contribution of small scales are required to close the filtered equations.

Eqs. 12-16 are simplified from the general N-S equations with all acoustic effects being filtered out. The reason for the simplification is that the general N-S equations describe a rich variety of physical process, many of which have nothing to do with fires. Involving of those process will inevitably increase the computational expense without giving reasonable benefit to the predictions. The equations are set to deal with low Mach number combustion, where the low speed motion of a gas is driven by chemical heat release and buoyancy forces.

3.2.2 Filtering process

As described in eq. 11, the box filter developed by Deardorff [95] was applied in the filtering process. The filter width is connected to the grid resolution and the research requirement. Within each cell the flow characteristics (velocity, temperature, etc.) are assumed to be spatially uniform, changing with time only. Comparing to other filter functions [25], the box filter is easier to be embedded into the numerical solutions. With the support from a fairly good grid resolution, the box filter is regarded as a satisfactory filtering tool for the LES of pool fires.

3.2.3 SGS Turbulence Modelling

Various SGS models for momentum, species and energy have been tested and adopted by many researchers. The SGS stress models which represent the momentum contribution from the small scales are of special interests to pool fire simulations. In this simulation, Smagorinsky model [26] as described in eq. 19 is used for SGS turbulence modelling. Previous work has proved the Smagorinsky model a suitable tool for LES in turbulence. As recommended by FDS, the model coefficient C_s=0.17 is fairly good for the majority of fire applications. Furthermore, The established Smagorinky model in FDS codes could bring much computational convenience to the test and validation of the SGS combustion model. The reduction on computational expense could also make it feasible for high-resolution calculations.

3.2.4 SGS Combustion Modelling

Two combustion models were implemented in the current simulation. One was developed in the National Institute of Standards and Technology (NIST) USA for the FDS codes [2, 97] (referred to as "mixture fraction model") and the other was modified

by the author based on Cook and Riley's laminar flamelet theory [51] (hereby referred to as "modified laminar flamelet model (MLFM)").

In both models mixture fraction was used to describe the reaction process. Chemical reaction was assumed to take place only at the stoichiometric surface where the mixture fraction reached the stoichiometric value,

$$\xi_{sf} = \frac{Y_{o2}}{rY_{f1} + Y_{o2}} \qquad (81)$$

where Y_{f1} and Y_{o2} are the ambient species concentration of fuel and oxidant, respectively. r is the stoichiometric coefficient. The laminar flames located at the stoichiometric surface were treated as one-dimensional. The whole flame was treated as an assembly of those thin flames (literately referred to as "flamelet"). The evolution of mixture fraction is controlled by the governing equation generated from the combination of its definition and the governing equation of species concentration.

The numerical details of MLFM and the mixture fraction model could be referred to Chapter 2 and FDS User's Guide [2], respectively. The differences between the two SGS combustion models could be summarised as following:

The governing equation of mixture fraction

In the mixture fraction model, mixture fraction that represents the chemical reaction is solved by the simplified governing equation (eq. 48). In that equation the SGS contribution was filtered out. This is fairly reasonable for large-size fires as most of the energy stays in the large eddies. And the ignorance of SGS quantities could also brings advantage to computational efficiency. For smaller size fires, however, the

importance of SGS contribution increases and the neglect of it could damage the accuracy of prediction. Therefore in MLFM the calculation of mixture fraction is governed by eqs. 70 and 71, which take full consideration of the SGS quantities.

The calculation of heat release rate

In the mixture fraction model, the assumption of "infinitely fast reaction" implies that the oxygen and fuel cannot co-exist at any local point. This leads to the "state relation" between the oxygen mass fraction Y_o and the mixture fraction (eq. 49). Following this, the heat release rate was calculated from the mass consumption rate and the heat of combustion of the oxygen [2] (eq. 50). While in MLFM, the calculation of heat release rate is based on both the reactants and the products,

$$q'''_{ijk} = \sum_n \Delta H_n \left. \frac{d\overline{Y_n}}{d\overline{\xi}} \right|_{\xi<\xi_f} \frac{\left(\overline{\rho D}\right)_{i+\frac{1}{2},j,k} \frac{\left|\overline{\xi_{i+1,j,k}} - \overline{\xi_{i,j,k}}\right|}{\delta z}}{\delta x \delta y \delta z} \qquad (82)$$

where n = f, o and p, respectively.

3.3 Experiments Considered

A methanol pool fire of Weckman and Strong [98] and a set of propane gas fires of Cetegen and Ahmed [74] are simulated. The propane pool fire set of Cetegen and Ahmed [74] had variable diameters from 10 to 60 cm. The flow rate of fuel was controlled to give different input heat ranging from 20 to 120 KW. The methanol pool fire of Weckman and Strong [98] was set on a circular burner with a diameter of 30.5 cm. Methanol was fed at a constant rate to give a total heat release rate of 24.6 KW. Both the propane and the methanol fires were set in open air at the room temperature.

3.4 Computational Domain and Grid Sensitivity Study

In the current simulation, the fire is basically modelled as the ejection of pyrolyzed fuel from a sold surface or vent that burns when mixed with oxygen. Depending on the physical phase of the fuel, either a heat release rate per unit area or a heat of vaporization at the fuel surface is specified. The stoichiometry of the reaction is set to identify the fuel type. All species associated with the combustion process are accounted for by way of the mixture fraction variable. The heat release rate per unit area is used to control the burning rate and initial velocity of the fuel in the case of a prescribed fire using a gas burner (propane fires). While for a methanol fire, the heat of vaporization is used in the case that the burning rate of the fuel is dependent on the heat feedback from the fire.

For the methanol fire, a rectangular computational domain was set with dimensions of 1.6m(W) X 1.6m(D) X 3.2m(H) in a Cartesian co-ordinates. Except the ground, all other boundaries are set open. The atmosphere air is still at the beginning of the simulation. The dimensions of propane fires were adjusted proportionally according to the burner size.

The determination of such a computational domain came from a series of sensitivity studies. It has been found that narrow width/depth (less than 4 times of burner diameter) limited the development of eddies and gave incomplete description of air entrainment. The large domain (more than 8 times of burner diameter in width/depth), however, reduced the mesh resolution due to the computational affordability of computers. During the analysis of the results from the current simulation, no visible

eddies were found at the edge of the computational domain, which demonstrated that the domain was big enough for the turbulent mixing. Around two million cells (128 X 128 X 144) were employed in the simulation giving an average mesh resolution of 1.3 cm. Cells within the centre of fire were further stretched to obtain finer resolution of 1 cm.

The comparison of simulation results of mean temperature at different heights from different grid resolutions was shown in Fig. 3.1 (methanol pool fire). The medium grid resolution (referred to as "Kang and Wen [30]"), which contained 64 X 64 X 96 cells, was found to generated relatively poor agreement with the experimental data. The resolution of 128 X 128 X 144, as employed in the present study, was found to give better prediction. To validate the grid independence, another grid resolution of 108 X 108 X 128 was tested for the same case and the results were plotted on the same graph. No significant difference was found in comparison with the results from the resolution of 128 X 128 X 144. Hence the grid resolution of 128 X 128 X 144 is used for the validation and comparison of combustion models.

Considering the pulsation periods for such medium-scale pool fires are generally less than 1 second, the computational time was set to 20 seconds to give enough time for the fire to reach the fully developed stage. During the simulation, the time step was dynamically adjusted by the instantaneous velocities ($DT < \min(\frac{\Delta x}{u}, \frac{\Delta y}{v}, \frac{\Delta z}{w})$). The instantaneous results were monitored regularly and fire was assumed to have reached quasi steady state when the instantaneous values appeared periodically.

3.5 Results and Discussion

In this section, firstly, the MLFM will be presented by the mean quantities of the pool fires. The predicted temperature, velocity, density and heat release rate will be analysed in comparison with experimental measurement and simulation results from mixture fraction model. These will be followed by the dynamic behaviour study on puffing frequency, the variation of Strouhal number versus Froude number and the predictions of air entrainment. The grid resolution used in mixture fraction model simulation was the same as that used in the simulation with MLFM. Due to the availability of experimental data, the majority of simulation was carried out for the methanol pool fire. By default, the following analyses are for methanol fire unless specifically indicated for propane fires.

Calculated from the burner diameter, the pulsation period of the current methanol pool fire is about 0.32 seconds. The simulation time was set to 20 seconds to give the system enough time to reach a stable status. The cyclic behaviour of axial velocity at a certain point within the fire was shown in Fig. 3.2a. The instantaneous values formed regular cycles, indicating that the simulation has reached the convergence. The data were recorded after 10 seconds of simulation (the starting point of 0 at the time axis represents the 10th second of simulation). All the time-averaging processes are carried out over five converged pulsation periods. Comparison has been made between the average values from different numbers of puffing cycles and no significant difference was observed. Calculated from Fig. 3.2a, the puffing frequency was 2.68 Hz, which agreed well with Malalasekera's correlation [77].

In additional to fig. 3.2a, the spectra of temperature fluctuations and the frequency of crossing a range of reference temperatures were shown in figs. 3.2b and 3.2c,

respectively. In fig. 3.2b, a clear dominant frequency of nearly 3 Hz is evident at almost all the heights, which agreed well with the frequency of 2.68 Hz obtained from fig. 3.2a. This distribution is similar to the experimental measurement done by Cox and Chitty [143], in which it was claimed that the frequency was determined by the flammable volume controlled by the fire size. In fig. 3.2c, the peak frequency of crossing 1000C occurs at Z'=0.06, where is believed to be the reaction zone. The peak frequency of crossing 500 and 750 C occurs within the intermittent regime ($0.08 < Z' < 0.2$) while the peak frequency for 250C at the fully developed plume area ($Z' > 0.2$). These computational results illustrate that the majority of combustion takes place in the reaction zone. While in the intermittent zone the fire is extinguishing and the heat transfer there is dominated by the turbulence mixing. In the plume zone almost no combustion exists and temperature drops quickly towards the ambient value. Experimental measurement of Cox and Chitty [143] are also listed in fig. 3.2c and they are in good accordance with the current simulation results at all temperature levels.

3.5.1 Mean Quantities

3.5.1.1 Temperature

In Fig. 3.3 the mean temperature at different heights (6,12, 20 and 30 cm) were presented. The simulation results from the two SGS combustion models were compared with the experimental measurements. Both simulation results exhibited good agreement with the experimental data. The peak temperature was located in the centre of the fire, and the peak values decreased with the height. This was in accordance with the fire physics that the reaction takes place in the centre of the fire and the reaction rate is reduced along the height as fuel is consumed. At the same

height, the temperature decreased along the radius because more cold air was entrained from the outside region and the reaction rate decreased.

The change of centreline temperature was shown in Fig. 3.4. The highest temperature occurred at 6-8 cm above the burner and then decreased with the height. The gradient of the decreasing was going down, showing that the temperature was reaching the ambient value very far downstream. There was no significant difference between predictions from the two combustion models. However, the simulation result from the MLFM was showing a better agreement with the experimental data [98].

3.5.1.2 Velocities

Similar to Fig. 3.3, the distribution of axial velocities was presented in Fig. 3.5. The magnitude of axial velocity was determined by vortex movement and density stratification. At the lower heights the flow was dominated by the chemical reaction. Eddies were generated at the burner rim then entrained towards the fire centre. Driven by the combining effect of molecular mixing and density stratification, the vortices were moving upwards while evolving, which resulted in a relatively high axial velocity in the centre. The axial velocity decreased along the radius as the buoyancy becomes weaker at larger radius. In the region above the reaction zone, where the majority of the flow was in the fully developed turbulence regime, the intensity of turbulence mixing and the buoyancy effect caused a rapid increasing of the axial velocity. At the lower heights, where the flow was believed to be in the transitional region, the mixture fraction model seemed to under-predict the axial velocity while in the reaction zone and fully developed turbulence region, the mixture fraction model over-predicted the velocity in the centre of the fire and underestimated at the outside

region. For all the heights listed in Fig. 3.5, the MLFM gave a better prediction.

Mean radial velocities at different heights were shown in Fig. 3.6. At the lower region, air was entrained into the centre and mixed with the fuel. With the height increasing, the intensity of fuel-air mixing increases, making the stoichiometric surface of the mixture fraction drifting outwards. As a result, more combustion took place in the outer region, causing the fire "expanding". Accordingly, the peak value of radial velocity was moving outwards with the height. At the lower height (6cm), the peak values of radial velocity predicted by both models were similar. In the predictions from the mixture fraction model, the peak value occurred closer to the fire centre (r = 3cm). At the radius of 5 cm, the radial velocity reduced close to 0, showing the tendency of fire to "expand" outwards. In the predictions from the MLFM, the peak value of radial velocity occurred at r = 5cm. And the majority of the absolute values of the radial velocities at all the shown radial locations were over 0.4 m/s, indicating a main stream of air entrainment. At the reaction zone (height = 20cm), the radial velocity estimated by the MLFM became close to 0 at the centre of the fire, demonstrating the existence of vortices generated by the combustion. While in the outer region, the radial velocities were still negative, indicating that more air was entrained into the system as required by the combustion. In terms of the prediction of radial velocities, the mixture fraction model generated good agreement with the MLFM at the outer region but in the centre it over-predicted the magnitude of radial velocity. When it reached the height of 30cm, both models gave similar prediction on radial velocity at all radial locations. The magnitude of radial velocity in the centre was still high. This was due to the remains of incomplete combustion. At the outer region the radial velocities were becoming more homogeneous.

As shown in Fig. 3.7 (measurements taken at r = 15cm), the magnitude of radial velocity at the lower heights was much bigger than that in the higher region, showing a considerable amount of fresh air being entrained into the fire centre due to the combustion. The main flow below and within the reaction zone was dominated by rapidly rising and expanding eddies from chemical reactions. While in the upper area, where the main flow field was characterised by the turbulent mixing, the intensity of air induction decreased. In Fig. 3.7, both SGS combustion models exhibited similar distribution of air entrainment velocities. However, the mixture fraction model over-predicted the air entrainment velocity near the burner base and under-predicted it within and above the reaction zone.

The radial velocity contours were listed in Fig. 3.8. The distribution of radial velocity from both simulation predictions were similar with that observed in the experiment. The highest radial velocity occurred near the burner rim at a radial position of 12cm, where the air entrainment rate was expected to reach the maximum. The radial velocities in the centre of the fire were also high due to the chemical reaction. The magnitude of radial velocity decreased with the height and the peak value moved towards the centre at the same time. This was thought to be the result of the completion of combustion and the development of vortices. Comparing to those from the mixture fraction modelling, the simulation results from the MLFM were found closer to the experimental measurement. However, the magnitudes of radial velocities from both simulations were larger than the experimental data. The exact cause is not clear. It may be linked to some simplifications in the momentum equation where the hydrostatic pressure gradient was subtracted and the neglect of the baroclinic torque

due to the non-alignment of density and pressure gradients. Those simplifications were believed to have more impact on the predictions of radial velocities than the axial velocities. However, the relatively large discrepancy may also come from the uncertainties in the experimental measurements. As can be seen from the following paragraph, the predicted air entrainment rate calculated from the radial velocity agreed well with the established correlation.

3.5.1.3 Air Entrainment

In Fig. 3.9, the predicted mean air entrainment rates were compared with the correlation of Delichatsios [100], the data fit of Delichatsios & Orloff's [99] and the experimental data of Beyler [102]. The related radial velocity was taken at a radial position of 15cm. According to Delichatsios [100], air entrainment in pool fires can be divided into three different regions. The parameters that could affect the air entrainment behave differently in each region. Delichatsios suggested that the dimensionless air entrainment rate m_{ent} (normalized by the fuel supply rate mf) up to a vertical distance Z above the fuel source was determined by the Stoichiometric number S, the Froude number Fr_f and the normalized height Z/D. He proposed that $\frac{m_{ent}}{(s+1)m_f} Fr_f \sim \frac{Z}{D}$. Since the air entrainment rate was proportional to $\rho_\infty A U_{ent}$, Delichatsios [100] further argued that the correlation between air entrainment rate and the height varied at different regions. Near the burner base, where $A \sim D^2$, the air entrainment rate was proportional to $(Z/D)^{1/2}$. At the "neck-in" area, where most reaction took place, the air entrainment rate was proportional to $(Z/D)^{3/2}$ since the entrainment area "A" there was proportional to "ZD". In this region, air entrainment rate relied heavily on height. The air entrainment rate increased quickly with the height and most of fuel was burned here, resulting in the so-called "neck-in" area.

And at the upper part of the fire, where the air entrainment was dominated by the turbulent mixing and had little to do with burner diameter, the air entrainment rate was proportional to $(Z/D)^{5/2}$. In this region, less fuel was left and height-related buoyancy became the dominant factor for air entrainment. The simulation results from both SGS combustion models were listed. Both predictions behaved similarly while in lower region the present study gave more reasonable description of air entrainment velocity. The results from current simulation agreed well with Delichatsios's analysis in all three regions, suggesting that the MLFM generated fairly accurate prediction for the air entrainment rates and the combustion processes in pool fires.

3.5.1.4 Density

In an open fire, as suggested by Cook and Riley [51], the product of temperature and density (literately called thermodynamic pressure) was spatially and temporally constant. This theory was strongly supported by the stratification of mean density in Fig. 3.10. The lowest value of density occurred in the fire centre near the burner base, where most of the reaction took place and the temperature reached the peak value. The density increased along the height and the radial direction, which agreed well with the temperature distribution. The coloured contours of density were shown in Fig. 3.11. It was clearly indicated by the colour that the vertical gradient of density at lower heights was much steeper than that at higher places. This was due to the chemical reaction that generates lots of heat and made the temperature increase rapidly in the reaction zone. In the upper turbulence area, most of the combustion ceased and no more heat was expected to generate. The isotherms of density "expanded" horizontally due to the turbulence mixing, causing a relatively homogeneous distribution in the radial direction. Simulation results from both models

exhibited similar characters. Compared with the mixture fraction modelling, the MLFM did manage to give more detailed illustration of mean density.

3.5.1.5 Heat Release Rate Per Unit Volume (HRRPUV)

The comparison of predicted HRRPUV from two combustion models are listed in fig.3.12. In fig. 3.12 (a), the highest heat release rate per unit volume was found in the outer region of the flame near the pool base, where the mixture contained abundant fuel gas/vaporised fuel. As revealed in the current prediction as well as that of Zhou et al. [95], the oxygen concentration was also high there because of the strong inflow of air towards the centre near the base induced by the sharp pressure gradient between the flame and the surroundings. Near the base, the heat release rates in the centre were relatively low due to lack of oxygen. Further up, with more fresh air being entrained by the rising flame and brought into the centre by the evolving vortices, the heat release rate reached the highest in the fire centre. In consistent with previous findings, the combustion intensities were strongest in the "neck-in" region about a half diameter height above the pool surface. Following that, combustion continued but the high heat release regions were becoming gradually smaller before the combustion processes almost fully completed at a height of approximately 1.8 m, i.e. approximately 6 diameters above the pool surface. Along the radial direction apart from immediately above the pool, the intensity of combustion decreased gradually from centre outwards, leading to the reduction of volumetric heat release rates, as well as mean temperature and axial velocity (Figs. 3.3 and 3.5). The mixture fraction modelling also gave the similar distribution. However, it under-predicted the HRRPUV and provided less details due to the difference of mechanism in calculating HRRPUV.

3.5.2 Dynamic Behaviours

Four consecutive plots of instantaneous temperature contours and velocity vectors were listed in Figs 3.13 and 3.14 to demonstrate the dynamic behaviours of the fire after it reached the stable status. The time interval between two adjacent plots is 0.08 seconds, which was determined by the puffing frequency. As calculated from Fig. 3.2, the puffing frequency of the current methanol fire was 2.56 Hz, leading to a puffing period of 0.32 seconds. To give four continuous contours of velocity vectors within one pulsation period, 0.08 seconds were chosen as an interval.

In the temperature contours (Fig. 3.13), hot eddies were formed at the edge near the base of the burner. Small eddies were then rolling into the centre of the fire with the air entrainment and rising upwards. During their movement, the eddies continue to evolve. At the height of approximately one pool diameter, the eddies started to separate from the plume and gradually vanished in the turbulent fire plume. The well-known phenomena of pool fire "neck-in", where the air entrainment velocities reached peak values and visible flame there shrank as a neck, was identifiable from the instantaneous velocity fields. The fluctuation of the "neck-in" height from about half to one pool diameter above the base can also be seen. Most of the burning completed before the separation point at a height between one to two pool diameters and just after the fire had "necked-in" (Fig. 3.13). Some isolated pockets of hot eddies can still be seen above that. This was believed to be linked to the existence of fuel-rich pockets. In the mean time, new eddies started to form near the base. The periodical motion of hot eddy generation and shedding was thought to be the dominant cause of the fire pulsation. The above findings were consistent with

previously reported experimental results [74,103] and numerical simulation of Ghoniem *et al.* [87] using a vorticity-based approach.

The predicted instantaneous fields of velocity vectors at four successive times were shown in Fig. 3.14. The results have confirmed previous experimental observations that such pool fires were not axially symmetric but instead they were fully 3-D [91]. Air was entrained from the outside region into the fire at all heights. Intermittent shedding of small vortices is seen around the perimeter of the source and the circulation in these vortices was from the outer flame edge towards the centre. This was in the opposite direction to the circulation of the large flame puffs downstream. Also in consistent with the experimental observation, the predicted scale of these vortices was small compared with those of flame puffs. As the vortices rolled upwards from the instability region near the base, the rate of reaction increased with more entrained air and higher degree of turbulence mixing. To give a better demonstration of the "neck-in" area, four line plots of instantaneous air entrainment velocities against the height were presented in Fig.3.15, representing four instantaneous moments within a pulsation period. The velocities were taken at the edge of fire (radial position = 15 cm). The negative values of velocity represented the air being entrained into the fire centre. The maximum air entrainment velocity occurred near the base of the burner, with the second peak value puffing between the heights of a half and one diameter. Even at a certain point, the air entrainment velocity was changing periodically, showing the pulsation caused by the generation and development of vortices. The results also suggested that the "neck-in" were linked with the large flame puffs as well as the shedding of small vortices near the pool

surface. Previous studies suggested that most combustion reaction took place near and within the "neck-in" area [100,104].

3.5.3 Puffing Phenomena

As suggested by Cetegen [78], the burner diameter played a dominating role in affecting the puffing frequency. In Fig. 3.16, the variation of puffing frequency with the pool diameter was plotted along with the experimental data of Cetegen and Ahmed [74] and the recommended correlation of $f=1.68*D^{-0.5}$. It should be pointed out that when this correlation was first derived by Cetegen and Ahmed [74], the recommended coefficient was 1.5. Later analysis of Malalasekera et al. [77], which included a wider range of pool fire experimental data, suggested a better fit with the coefficient set to 1.68 and this modified coefficient was hence used here. Some of the experimental points in Fig. 3.16 were obtained from pool fires with fuel other than methanol. This was made feasible since the type of fuel has less influence on the puffing frequency.

The variation of Strouhal number St with the inverse of the Froude number 1/Fr was also plotted on the same graph which compared the present predictions with the well known correlation of $St=0.52*(1/Fr)^{0.506}$ [77], and the Strouhal numbers derived from the experimental data of Weckman and Strong [98] for methanol pool fires. Generally good agreement was seen between predictions from the MLFM and the correlation and the experimental data.

Although the puffing frequency was influenced by several parameters including burner diameter, fuel properties and inflow velocity, etc., previous research has

suggested that the burner diameter plays a dominant role [74,75,77]. The influences of fuel properties and flow rates were considered as marginal and they could thus be neglected for a simplified industrial application. As shown in Fig. 3.17, where the puffing frequency versus different fuel flow rate was plotted for three different burner diameters, the prediction from the MLFM was in line with this belief.

3.6 Concluding Remarks

Detailed numerical studies have been conducted for medium size methanol and propane pool fires. Two SGS combustion models were employed and compared in the current simulation. Both models used mixture fraction to describe the combustion process. The combustion was computationally separated from the turbulence, which made the calculation of high-Reynolds flows feasible. Based on the improvement on the SGS contribution of mixture fraction and the methodology of calculating mass fraction, the MLFM has showed its advantage in capturing both the dynamic behaviour and the distribution of mean flow variables. Generally compared with the mixture fraction model, the MLFM showed its improvement on predictions primarily in the reaction and turbulence zone, while in the laminar/transitional zone the discrepancies between predictions from two models seemed to get smaller. Quantitatively judged by the experimental measurement, the MLFM has improved the prediction on mean temperature and axial velocities by up to 20% and the radial velocities by up to 30% over the mixture fraction model.

LES with the MLFM has captured the toroidal vortices closely related to the large scale puffing as well as the accompanying smaller vortices. The generation and development of energy-containing eddies were clearly shown in the instantaneous

snapshots of temperature and velocity vectors within one pulsation period. The predicted puffing frequency and the variation of Strouhal number versus the inverse of Froude number were in good agreement with experimental data and correlation. The pulsating nature of air entrainment was demonstrated by the air entrainment velocity fluctuations and the instantaneous velocity vectors. The predicted variations of air entrainment at different heights agreed well with some published data on propane and methanol pool fires and the correlation of Delichatsios [101]. The predictions also confirmed previous experimental observation that such pool fires were not fully axially symmetric.

The turbulence model used in the simulation was Smagorinsky model with a constant coefficient 0.17. Although argued to be too dissipative and to have no mechanism to represent the energy backscattering, this model was believed to give a fairly reasonable description on the turbulence development in the current case. The work of developing and applying a dynamic approach of SGS turbulence model is illustrated in the following Chatpers.

Chapter 4 Small Pool Fire

4.1 Introduction

The mechanism of air entrainment in pool fires has attracted considerable attention because of its relevance to flame extinguishments and instability near the pool surface. For small pool fires with burner diameter generally less than 30 cm, the characteristics of the flow field have been found to show considerable difference from medium or large fires. Additional difficulty arises for the accurate measurement. For example, the technique used should not quench the chemical reactions and the fuel should not be too sooty in order to avoid strong soot emissions. Numerical simulation of small pool fires will inevitably require higher grid resolution and this could increase the risk of computational instability.

Zhou and Gore [104] performed a series of laser-doppler-velocimetry (LDV) and particle-image-velocimetry (PIV) measurements and obtained a velocity map around a liquid pool fire of 7.1cm diameter. Cetegen [107] developed a unique optical measurement system and obtained a series of velocity fields for pulsating buoyant plumes of helium-air mixtures over a 10-cm-diameter nozzle. In his study Cetegen found that the flow structure of buoyancy-controlled pool fires could be simulated by flow moving upwardly against a quiescent air environment. Those measurements gave insight to the air-entrainment and flame anchoring of small pool fires. Bouhafid *et al.* [108] suggested that air entrainment near the base leads to fuel-air mixing by convection, giving the flame a premixed character and causing small pool fires to be anchored. However, the reliability of their experiments was partly impaired by the quenching area caused by the temperature probes. By using a particle-track laser-sheet

technique (PTLS) with a high-speed video camera (500 frames/s and 25° view angle), Venkatesh *et al.* [109] carried out a series of experiments of small pool fires with diameters ranging from 1.5cm to 20cm. They managed to visualise the flow field near the pool base and suggested that it is the premixing of fuel and air near the base that is responsible for the anchoring and stabilisation. They observed double flame and suggested different mechanisms of air entrainment at different heights.

The majority of previously reported simulations of small pool fires were considered within the traditional computational fluid dynamics (CFD) or large eddy simulation (LES) domains. Rehm and Forney [110] applied a zone fire model on a small pool fire and gained a fairly reasonable profile of temperature distribution. To calculate the heat release rate and the position of the flame, Hu and Fukuchi [111] developed a combustion model based on the calculation of gaseous fuel and air mixing. This model has been implemented into an existing CFD code with LES option on a 25-cm pool with diesel oil. Three major zones of pool fires have been identified. However, the detailed features inside the flame were not captured. Kang *et al* [99] carried out detailed LES simulations of the medium-scale methanol pool fire experimentally investigated by Weckman et al. [98] and achieved reasonably good agreement with the experimental data on the mean and fluctuating axial velocities and temperature distributions. However, relatively large discrepancies were found in the predictions of the radial velocities. The present simulation is partially inspired by the experimental work of Venkatesh et al. [109]. It aims to shed further light on the characteristics of such small pool fires and to demonstrate the capability of the current LES model for their predictions. Based on the previous simulations of medium-scale pool fires [99], a

modified version of Cook and Riley's laminar flamelet model [51] is used as the SGS combustion model and the Smagorinsky model is used for the SGS turbulence closure.

4.2 Flame Location and Structure

McCaffrey [112] and Cox and Chitty [113] proposed the three-zone structures for pool fires (see Fig. 4.1): a continuous flame zone, an intermittent flame zone and a plume zone. For small pool fires, Venkatesh et al. [109] further divided the continuous flame zone into three sub-zones: the quenching zone, the primary anchoring zone (PAZ) and the post PAZ. The quenching zone is just above the burner rim with a sub-millimetre size. In the quenching zone, the fuel and air are premixed by molecular diffusion. Above that, the cross-sectional area of PAZ is about 1cm height by 1cm wide in radial direction, consisting of a millimetre-size visible leading flame edge and an extended flame zone which is believed to be diffusion controlled. Due to the premixing in the quenching zone, the visible flame was not seen attached directly to the burner rim in the experimental investigations. The anchoring of flame at PAZ is believed to be the unique characteristic that distinguishes small pool fires from medium/large-scale fires. Apart from the anchored flame, small pool fires are also demonstrating characteristics such as double flames and axial symmetry which are also rarely seen from medium pool fires [99].

4.3 Numerical Modelling

The LES approach applied here is based on a set of spatially filtered, time-dependent conservation equations (eqs. 12-16). The Smagorinsky's eddy viscosity model [26] is used as the SGS turbulence model with a coefficient (C_s) of 0.17 following McGrattan et al. [2]. In the current study, two models have been adopted for SGS combustion

modelling. One is the laminar flamelet model of Cook and Riley [51] and is modified by the authors for present use. The other is a simple global mixture fraction model developed by Mell et al. [88] and already embedded in FDS. The details of numerical procedures of SGS turbulence and combustion modelling were presented in previous Chapters.

4.4 Experiments Considered

A series of small pool fire experiments were conducted by Venkatesh *et al.* [109] with various burner diameters, ranging from 1.5cm to 20cm. Within the above diameter range, all the pool fires were found to exhibit a similar flame structure. Detailed measurements were carried out on the 5.7cm-diameter burner made of stainless steel with a height of 2cm. The burner wall temperature was kept at 20 ± 2°C by wrapping the pan's outer wall with a 4mm-diameter copper tube and circulated water through the tube. The fuel is supplied underneath the burner at a constant rate to give a consistent heat input of 909 kW/m^2 into the system. The fuel surface in the burner is kept 0.5mm below the burner rim which is found by tests to give the most stable fire.

Hexane was chosen as the fuel because it is less sooty than many other fuels. It has to be pointed out that, however, the thermocouples at the height of 10mm were coated by the soot, which caused relatively large radiation losses and uncertainties in the thermocouple temperature measurement.

4.5 Computational Details

The computational domain is set to give enough space for the development of the fire and its plume. On the other hand, the grid resolution should be fine enough to capture

the flow movement at the smallest possible scale. In order to compare the simulation results with the experimental measurement [109], the dimension of a single cell in the fire centre is required to be no bigger than 1~2 mm. Following previous observations that pool fires are not truly axisymmetric [91], the full circle of the file is simulated. Compromising the computational accuracy with the efficiency, a total of 128 × 128 × 144 grids were employed in a 0.24m × 0.24m × 0.37m computational domain. This gives an average resolution of 1.9mm (for a single cell). The grids inside the fire were stretched to give a better resolution of 1.2mm, equivalent to 47 computational cells across the pool diameter. Although this resolution is still coarser than that employed in the experimental measurement, the predictions show some encouraging details of the flow movement. For the purpose of sensitivity study, another grid resolution (128 × 128 × 128) is also employed for temperature and velocity analysis. No significant difference has been found between simulation results from these two resolutions.

The domain is set to open at walls and the ceiling. The burner is defined at the ground and given appropriate heat input. According to Malalasekera's correlation [77], the pulsation frequency for a 5.7-cm diameter pool fire is 7.04 Hz, giving a puffing period of 0.142 seconds. The computational time is set to 20 seconds to ensure that it reaches the stable and converged status. The time step is dynamically adjusted by the instantaneous velocities (DT < $\min(\frac{\Delta x}{u}, \frac{\Delta y}{v}, \frac{\Delta z}{w})$). The instantaneous results are monitored regularly and the fire is assumed to have reached Quasi-Steady state when the instantaneous values appear periodically.

When defining the physical dimensions of the burner, the circular burner is approximated by the assembly of small squares. The mechanism of approximation can cause systematic errors at the edge of the circle. However, this is thought to be insignificant as there are 47 cells across the pool diameter.

4.6 Results and Discussion

In this section, discussion will first focus on some experimentally observed unique characteristics of small pool fires such as flame anchoring, double flame and axis-symmetry. For comparison, some qualitative comparison is made with the characteristics of medium-scale pool fires. This will be followed by some investigation on the effect of SGS combustion models in the LES predictions. Comparison will be made between the predictions using the laminar flamelet approach modified from Cook and Riley's model [51] and the mixture fraction model of Mell *et al* [91].

4.6.1 Flame Anchoring

The common understanding is that premixing near the burner base of small pool fires is responsible for flame anchoring and stabilisation. Takahashi and Schmoll [114] have shown that for the turbulent jet flames, the mechanism of anchoring depends on the formation of shear stress related circulation. However, Venkatesh et al. [109] suggested that in a pool fire, the fuel and oxidizer velocities at PAZ are much smaller than those in turbulent jet diffusion flames, perhaps insufficient to produce shear stress. They found a quenching zone just above the burner rim and believed that the flame anchors at that area due to the existence of fuel-air premixed zones.

The coloured temperature contours near the burner base are shown in Fig. 4.2. The temperature in the centre of the fire, just above the pool, is relatively low (indicated by blue and light green colour), showing the existence of the quenching zone. It is even more obvious at the beginning and end of the pulsation period. In plots (a) and (d), the flame (indicated by the red colour) is not attached directly to the burner rim. The temperature drops quickly to about 400 K, causing the flame to anchor here.

4.6.2 Double Flame or Triple Flame?

In small pool fires, the initially separated streams of fuel and oxidizer may mix by molecular diffusion after flowing past a divider. The theoretical structure of the flame near the base or the burner rim resembles a wall-quenched triple flame, consisting of two pre-mixed flames, one lean and the other rich, and another diffusion flame occurring at the stoichiometric surface. In the experiment [109], the double flame rather than the triple flame was observed. The possible reasons have been argued by some researchers [115-118]. One argument that was supported by the experiment of Venkatesh *et al.* [109] and the present simulation indicates that the flow velocity at the air-side is one order of magnitude larger than the velocity of fuel vapour in the fuel side and the visible flame sheet is located in the air side. This can be clearly seen in Fig. 4.3 (velocity vectors near the burner base). The air-side premixed flame is expected to be much larger than the fuel-side premixed flame. Previous analysis [115] has suggested that the flame at the primary anchoring zone possesses characteristics of the counter-diffusion flame, yet the existence of the cold wall quenches the flame and likely distorts the normal triple flame into the double flame. For comparison, the previous predictions [99] for the velocity vectors of a medium-scale methanol pool fire are also shown in Fig. 4.3. The velocities in the centre of the fire are larger than those in the

outer regions. The velocities in the outer region drop quickly to zero at some heights, showing the existence of vortex. This comparison demonstrates that in medium-scale pool fires air is entrained by turbulence mixing (vortices) and combustion takes places in the centre, while in small pool fires some fuel and air are premixed by laminar convection in the outer region (air-side) and double flames are formed.

The above argument is supported by the predicted contours of temperature and mixture fraction of both the present predictions and our earlier simulations of a medium-scale pool fire as shown in Figs. 4.4 4.5 and 4.6. In Fig. 4.4a, the temperature contour shows that the highest temperature (about 1500 K) is located about 10mm above the burner, at a radial position of 18mm. With the height increasing, the location of the peak temperature moves towards the centre of the flame as more cold air is entrained into the system. The temperature decreases radically along both directions (inwards and outwards the fire centre), showing that a premixed flame (PF) is formed near the edge. The gradient towards the airside is steeper than that towards the fuel side. The slow decrease of temperature towards the fuel side implies the characteristics of the counter-diffusion flame.

In Fig.4.4b, the temperature contour of a medium-scale pool fire with 30.5cm diameter from previous simulations [99] is shown for comparison. Although the dimension and co-ordination of Fig. 4.4b is different from those of Fig. 4.4a due to the grid resolution and simulation settings, the difference of the temperature distribution is clearly demonstrated. The peak temperature of the medium pool fire is located in the centre and decreases along the radius. This is consistent with the experimental observation of Weckman and Strong [98]. It can be attributed to the fact

that the reaction intensity and speed are much higher than those in small fires. The combustion in medium or large fires is thought to be "infinitely fast" [21]. The fuel and air cannot co-exist and hence there is no premixing zone. The intensity of reaction decreases from centre to outside regions. In the small pool fire the temperature in the pool centre is relatively low and the radial position of peak temperature is moving towards the centre with the increase of height. The flow near the burner rim demonstrates the counter-diffusion characteristics. More air is entrained into the PAZ by smooth laminar flow suction and the entrainment rate is comparable to the combustion rate. This results in the stoichiometric surface lying outside the centre of the fire and the premixed flames formed around the sides of the stoichiometric surface. The visible flame boundaries, which are indicated by a temperature of 600K, are clearly seen at both the fuel- and air- sides. This comparison demonstrates that the double flame induced by molecular diffusion is a unique character of small pool fires.

The above analysis can be further supported by the coloured temperature contour near the burner rim (fig. 4.5). The central diffusion flame is indicated by the red colour while two premixed flames (one at each side) are represented by the light yellow and green. Although the location and size of the flames are not perfectly illustrated due to the limit of graphic resolution, this coloured contour agrees well the distribution shown in fig. 4.4a. The diffusion flame stays between the two premixed flames with higher temperature. The locations of flames drift into the fire centre due to the relatively strong velocity at the airside.

The stoichiometric value of mixture fraction for hexane is 0.1. In the contour of mixture fraction shown in Fig. 4.6, the isotherm line of $\xi = 0.1$ is located at a radial

position of 2.5 cm near the burner base, then getting closer to the centre with the increase of height. The mixture fraction near the burner base exhibits a wide range, indicating the existence of pre-mixed region. It has been noticed that the maximum temperature isotherm is located coincidentally with the stoichiometric line of mixture fraction in Fig. 4.6, indicating the existence of double flame. The gradient of the reaction rate toward the quenching surface is so high that the location of maximum reaction rate practically coincides with the quench point. This is strongly supported by the isotherm of mixture fraction. Within the very short distance above the burner rim, the mixture fraction changes rapidly and the stoichiometric line, which represents the maximum reaction rate, lies in the quenching zone. In agreement with the experimental observation and analysis of Venkatesh *et al* [109], the existence of the cold wall quenches the flame and distorts the normal (or free boundary) triple flame into the double flame.

The position of the flame may vary, depending on the overall stoichiometry. At a mixture fraction co-ordinate, ξ=0 means the pure oxidizer stream and ξ=1 represents the pure fuel stream. Usually the stoichiometric line of mixture fraction is used to identify the locus of the flame. The stoichiometric coefficient r represents the mass unit of air consumed with the complete combustion of one unit mass of fuel. It is either greater or smaller than unity. For the hexane fire (r=9.5, ξ_{st}=0.0952), the flame lies on the oxidizer side in the mixture fraction co-ordinate. In both the experimental observation [109] and the current simulation the diffusion flame is located on the airside, which agrees well with the theoretic analysis [115,116].

4.6.3 Temperature Structure

In Fig. 4.7, the peak temperature occurs at about 15-25 mm in radial position at different heights. The radial position of the peak temperature is moving towards the centre of the fire with the increase in height. The peak value increases along the height as it is reaching the PAZ and post PAZ. There is a steep temperature gradient on the airside, which coincides well with the temperature contour in Fig. 4.3. The rate of temperature increase with height slows down when approaching the turbulent area, leading to a more uniform distribution.

4.6.4 Axial symmetry

The mean temperature contour of the whole computational domain (Fig. 4.8) shows a good axisymmetric shape, which was not seen in medium-scale pool fires [91,108]. The non-axial symmetry of medium and large pool fires in the three-dimensional simulation was shown in the calculation of Baum *et al.* [93] and Kang *et al* [99]. The present finding is also in agreement with the previous analysis [93] which suggested that the smaller the pool diameter, the more axially symmetric the fire.

4.6.5 Air Entrainment

Convective air entrainment likely occurs at PAZ to satisfy mass conservation because of the rapid acceleration of the buoyant gases in the flame interior [108]. The intensity of air entrainment is illustrated by the radial velocities. In Fig. 4.9, the radial velocities at different heights are shown. The maximum value of radial velocity is found at a radial location of around 2.5 cm from the centre, very close to the edge of the burner. The radial position of maximum radial velocity is moving towards the centre of the fire with the height while its magnitude is decreasing. The positive

values of radial velocity, which represent the flow expanding outwards from the flame, are showing at a range of heights below 12.5 mm. This is because that more fuel is sucked into the PAZ and mixed with the air, causing the flow "expanding" outwards. Above 12.5 mm, where the main part of combustion takes place, more air is needed for the chemical reaction. The radial velocities along all radial positions are negative, showing the large demand of air coming into the reaction region. Comparing the distribution of z = 12.5 mm with that of z = 20 mm, there are some interesting differences. The radial velocity in the outer region at z=12.5mm is higher; showing that large amount of fresh air is entrained from the ambient environment for the reaction near the edge. While inside the flame the magnitude of radial velocity is relatively small. At a height of 20mm or above, where most of the combustion is supposed to have completed, the flow is turning to be dominated by the buoyancy induced mixing. The magnitudes of radial velocities inside the flame are becoming larger due to the rapid rise of vortex.

The distribution of radial velocities shows that within the PAZ (usually below 12mm) air is entrained into the flame by laminar convection. The mechanism of air entrainment within the PAZ is different from that in a turbulent jet flame. In a jet flame, the air in entrained by the shear stress near the burner rim. However in the pool fire, as seen from Fig. 4.9, the inner radial velocities (r < 12mm) at PAZ (z < 10mm) exhibit positive values, implying that the flow in the centre is sucked outwards due to the relatively high intensity of combustion near the burner rim. In the outer region, air is entrained into the fire at a magnitude up to 4 m/s. This is due to the laminar convection caused by the rapid acceleration of the buoyant gases in the flame interior. At heights between 10mm and 20mm in the post PAZ region, radial velocities at all

radial locations fall into negative values. The magnitude decreases with the increase in height and the location of peak value gradually moves towards the centre. This demonstrates that at post PAZ the air is entrained into the system generally by diffusion.

The air entrainment velocity profile against height is shown in Fig. 4.10. The velocity is taken at a radial position of 2.59cm, close to the burner edge (r= 2.85 cm). The negative values show the air coming into the flame. The maximum rate of air entrainment occurs at a height about 5mm above the burner. The main part of air entrainment, represented by the high absolute values of negative radial velocity, is found to cover a region of height ranging from 2mm to 12mm, where the PAZ is. It agrees well with the experimental observation [109] that the air entrainment primarily happens at the PAZ by a smoothly laminar flow suction. Above the PAZ, the radial velocity decreases with the height implying that the vortex are forming and developing.

4.6.6 Comparison Between Two Combustion Models

To investigate the effect of SGS combustion modelling on the predictions, comparison is made between the simulations with the MLFM and the mixture fraction model of Mell et al. [88]. Additionally under the sensitivity study, some of the results are also compared to those from another grid resolution (128 ? 128 ? 128). At this grid resolution the SGS combustion model employed is also the MLFM and is referred to in the figure caption as "modified laminar flamelet model 2M".

Comparison has been made in terms of temperature, velocity and Heat Release Rate Per Unit Volume (HRRPUV). The radial distributions of temperature, radial velocity and HRRPUV at different heights are analysed in Figs. 4.11, 4.12 and 4.13, respectively. In addition to the line-plots, the contours of temperature and velocity vectors are also studied (Figs.4.14 and 4.15).

It is found that the differences between the two models are more obvious in the reaction zone. For all the three examined heights (2.5mm, 7.5mm and 20mm), the main discrepancy between the two models lies at radial positions between 14mm-18mm. The radial position of peak temperature gets closer to the centre of the fire with the increase in height. At the peak temperature region, where the majority of combustion takes place, the MLFM produces better prediction than the mixture fraction model. The under-prediction of peak temperature by the mixture fraction model is likely to be due to the omission of the SGS term in the governing equation of mixture fraction (see Section 3.3.3).

At the lower (2.5mm) and higher (20mm) heights in Fig. 4.12, there is little difference between the predictions of the two models. At the height of 7.5mm, the mixture fraction model underpredicts the magnitude of radial velocity. This is in accordance with the distribution of temperature.

The comparison of HRRPUV near the burner base is presented in Fig. 4.13. At all the three heights both models give similar predictions on HRRPUV. The mixture fraction model overpredicts the HRRPUV at all radial locations. This is because that the heat absorbed by the generation of products was not included in the mixture fraction model.

In Fig. 4.14 where the temperature contours are plotted, double flames are also captured by the mixture fraction model. However, the prediction of peak temperature is lower than that from modified laminar flamelet model and the predicted extent of the premixed flame near the burner rim is shorter than that of the MLFM. More importantly, the predictions of the mixture fraction model indicate a higher and more centred premixed flame near the burner rim. This is likely to be due to the different treatment in the governing equations of mixture fraction and the heat release.

In Fig. 4.15, comparison is made on the predicted velocity vectors. It is seen that the mixture fraction model predicts higher velocities in the centre of PAZ. The simplified approach of the mixture fraction model, which did not result in too much differences with the MLFM in our earlier simulations of bluff-body burners and medium-scale pool fires [119,120] seems to be causing more discrepancy here in the simulations of the small pool fires.

4.6.7 The first order of thermodynamic pressure $P^{(0)}$

As stated in eq. 66, in an open pool fire the first order of thermodynamic pressure $P^{(0)}$ is supposed to be constant in both time and space, which comes from the simplification of the state equation for ideal gas in low-Mach flows. This is numerically supported by the current research. The contour of $P^{(0)}$ is listed in fig. 4.16. In the majority of the computational domain (most of them are turbulence), $P^{(0)}$ remains a value around 400 Kg℃/m^3. At lower heights (where is believed to be laminar or transitional flow) the value of $P^{(0)}$ drops. Also at the edge of the computational domain $P^{(0)}$ drops to around 300 Kg℃/m^3, which is due to the mixing

with cold air. The time development of $P^{(0)}$ is presented in fig. 4.17. The sample point is located in the central line of the pool at a height of 15cm. The instantaneous data are collected from the 10^{th} second to the end of the simulation (the 20^{th} second). The stabilized values around 400 Kg℃/m^3 strongly proves the temporal constancy of $P^{(0)}$.

4.7 Conclusion and Recommendations

Large eddy simulations have been carried out for a small pool fire experimentally tested by Venkatesh et al. [109]. The Smagorinsky model is used for SGS turbulence closure and a laminar flamelet model based on the Cook and Riley approach [50,51] is used for SGS combustion modelling. Detailed analysis has been carried out on the structure and unique characteristics of small pool fires. To investigate the effect of SGS combustion modelling on LES predictions, comparison has also been made between the predictions using MLFM and the relatively simpler mixture fraction model of Mell et al. [88].

The predicted flow fields have captured the three distinctive characteristics of small pool fires observed in the experiment of Venkatesh et al. [109]. The existence of the premixed zone of fuel and air, which is thought to be the reason for flame anchoring, is evidenced by the low gradient of temperature and mixture fraction near the burner rim. The experimentally observed double flame can be seen from both the predicted temperature contour and velocity vectors. In line with experimental measurements, steep gradients of the mean temperatures are found in the air stream.

Unlike previous predictions of medium-scale pool fires [93,99], the mean temperature and density fields are nearly axially symmetric. This finding is in line with the analysis that the smaller the pool diameter, the more axially symmetric the fire.

Comparison of the predictions with the two different SGS combustion models shows that in the reaction zone the MLFM improves the predictions of temperature, velocities and HRRPUV by up to 30%. The relative positions of the double flames as predicted by the MLFM are also in better agreement with the experimental observation. This improvement can be partially attributed to the inclusion of SGS contribution in the governing equation of mixture fraction and the solution process of the look-up table, which are of particular importance in the simulation of small pool fires.

The study has demonstrated that the present LES approach with the modified laminar flamelet model is capable of capturing the fine details and unique characteristics of small pool fires.

Chapter 5 Bluff Body Flame

5.1 Introduction

Bluff-body flames have relevance to many combustion systems including aeroplane combustors, automobile industry and power plants [121]. Bluff body burners rely on re-circulating flows to stabilise the flame. It generally has simple and well-defined initial and boundary conditions. The flame is stabilised to the fuel orifice within a relatively complex flow structure. As the chemical reaction of reacting flows in a bluff body burner is mainly dominated by turbulent mixing, it is well acknowledged that the re-circulation zone plays an important role in influencing the combustion process [121]. For example, the existence of re-circulation zone is believed to improve the combustion efficiency and reduce the NO_x emissions for coal burners [122].

As the numerical simulation of chemical process has advanced significantly in recent years, bluff-body flows received particular attention under various simulation environments [41,123-129]. Standard k-ε model has been used in both non-reacting and reacting flows and some encouraging results have been reported [123]. Martins and Ghoniem [126], using a k-ε based vortex model, found that in a 2-D axisymmetrical simulation for incompressible, non-swirling flows, the flow structure in the re-circulation zone relies heavily on the fuel/co-flow air velocities and the diameter ratio. Similar experimental work has also been carried out by Sharif and Gu [130] for a V-shaped flame stabiliser. Other k-ε based models, such as those based on the Monte Carlo PDF approach, have been tested by Wouters *et al* [122]. When coupled with the PDF method and second-moment turbulence closure, the Monte Carlo approach was found good at predicting flow fields for inert flows. However, its inconsistent

predictions of reacting flows indicated that the finite-rate kinetic effects and partial premixing in such flows cannot be captured by the conserved-scalar chemistry model. Other combustion models such as simple chemical reacting system (SCRS) and eddy break-up (EBU) model have been tested by Lopes *et al* [125] for bluff-body flames. However, the systematic deficiencies of the standard k-ε model limited the accuracy of its predictions [127]. Under the Boussinesq hypothesis [7], a non-linear relationship between the Reynolds stresses and the strain rate and vorticity tensors was proposed in a series of cubic turbulence models [129,131], with terms up to the third order. The cubic models (de)stabilizes turbulence by streamline curvature. However, some of those cubic models may violate reliability conditions [127]. Based on the earlier models of Craft et al. [131] and Shih et. al. [129] , Merci *et al.* [127] proposed a new cubic model for piloted and bluff-body diffusion flames. Although the new cubic model showed satisfactory agreement with the experimental measurements, it under-predicted the levels of turbulent shear stress and kinetic energy. Hossain [142] and his colleagues have employed a couple radiation/flamelet combustion model when simulating a bluff-body non-premixed flame. Although a significant improvement in the prediction of OH was achieved when radiation heat transfer was included, discrepancy still existed in the predictions of mean flow quantities such as temperature. It seems unlikely that any two-equation RANS model will ever be able to predict all flow quantities correctly in the complete domain of a bluff-boy flame.

Proposed by Bilger [132] and Klimenko [133] independently, the conditional moment closure (CMC) approach is becoming increasingly popular for modelling turbulent reacting flows. The CMC model solves the transport equations of conditionally averaged quantities. The variables on which the chemical reactions are known to

depend on are chosen to be the conditioning variables. Within the frame of the RANS CFD approach with the k-ε turbulence model, Kim et al. [124] used CMC model and stationary laminar flamelet model (SLFM) to simulate a 2-D non-premixed methanol bluff-body flame. Although CMC was found to give reasonably good predictions of the conditionally averaged temperature and major species concentration at all spatial locations, solving the transport equations in the conditioning space adds a further dimension to the calculation. This, to some extent, is hindering the wider application of CMC to 3-D flow simulations.

Large eddy simulations of bluff-body flames carried out by Fureby *et al* [41] showed that chemical reaction played a determining role on the velocity field. But they also revealed that the 2-D LES could not mimic accurately the physical and chemical process in bluff-body flames. Similar 2-D large eddy simulation of bluff-body stabilized diffusion flame was carried out by Papailiou *et al* [144] with a partial equilibrium/two scalar exponential probability density function combustion model. They managed to catch the finite-rate chemistry effects such as local extinctions and reignitions but quantitative discrepancies increased in the prediction of mean temperature and major species. In other related applications, however, 3-D LES calculations have achieved considerable success. For example, Pitsch and Steiner [128] used the Lagrangian Flamelet Model as a combustion model for large-eddy simulations of turbulent jet diffusion flames. The predictions of the flow structures were in good agreement with experimental measurement, despite a slight over-prediction of the consumption rate of the reactants.

In the present study, detailed analysis of the dynamic behaviour and structure inside a bluff-body flame has been carried using LES techniques. The Fire Dynamics Simulator (FDS) is used as the basic LES frame while new sub-grid scale (SGS) models for combustion and turbulence modelling have been added by the author. The effect of SGS turbulence and combustion modelling on LES calculations is investigated by comparing the predictions with Germano's dynamic procedure with that of the Smagorinsky model and experimental data; and the predictions of the modified laminar flamelet model with that of the mixture fraction model and the experimental data. Further qualitative comparison is also carried out with the experimental data on some specific flame characteristics of the bluff-body flame such as the double flame phenomenon and the existence of the re-circulation region.

5.2 Numerical Formulation

The LES approach applied here, through the NIST FDS code, is based on a set of spatially filtered, time-dependent conservation equations (eqs. 12-16). In those equations the acoustic effect has been filtered out for the efficient simulation of fire phenomena.

For SGS turbulence closure, the Germano's dynamic approach is adopted. The Smagorinsky model is used for some comparative study with the model coefficient set to 0.17 following McGrattan *et al* [21]. The numerical details of implementing the dynamic approach should be referred to Chapter 2.

In the current study, two models have been used for SGS combustion closure. One is the laminar flamelet model of Cook and Riley [50, 51] which is modified by the authors

for present use (referred to as "modified laminar flamelet model (MLFM)" in the text). The other is a simple global mixture fraction model developed by Mell *et al* [91] which is already embedded in FDS (referred to as "mixture fraction model" in the text). The numerical details and the comparison between those two SGS combustion models could be found in previous Chapters.

5.3 Experiments Considered

The experimental work used in the current study was conducted by Masri *et al* [134]. As seen from the schematic plot in Fig. 5.1, the diameter of fuel jet orifice is 3.6mm and the bluff body diameter is 50mm, giving a diameter ratio ($\alpha = D_e/D_b$) of 0.072. The fuel jet velocity is 118 m/s and the co-flow air velocity is 40m/s. The fuel is a mixture of CH_4 and H_2, with a volume ratio of 1:1. The addition of H_2 to the CH_4 is intended to produce a re-circulation zone clean from soot.

Other experiments with different parameters (diameter ratio, flow velocities, fuel types etc.) have also been carried out by Dally *et al* [135, 136] from the same group. The present case is chosen due to its clean re-circulation zone and the availability of measurement in a relatively wide domain.

5.4 Computational Details

The whole domain is a rectangular block of 150mm ? 150mm ? 300mm. It is divided into 15 sub-blocks with various grid resolutions to allow finer grids in the critical regions. The mesh consists of 328,000 grid cells in total with the finest resolution in the flame centre to be 1mm. Grid sensitivity study has been conducted with other grid

resolutions and our preliminary tests suggested that the present resolution is sufficient to capture the fine details of the bluff-body flames.

The reason that sufficient grid resolution is achieved with only 328,000 cells is mainly because of the multi-block facility. Otherwise, the total number of grids would have to be more than 1 million to ensure the same resolution inside the flame. Although in some critical parts the cells can be stretched, the suppressing of vortices and the integration discontinuity at the edge of stretched and unstretched parts could potentially lead to the reduction in simulation accuracy. It was found in the sensitivity study that the use of the multi-block facility could significantly reduce the CPU time by reducing the number of grids while retaining the simulation accuracy.

Considering that the pulsation period of such a bluff body burner is less than 1 second, the computational time is set to 20 seconds to give enough time for the convergence. The time step is dynamically adjusted by the instantaneous velocities (DT < $\min(\frac{\Delta x}{u}, \frac{\Delta y}{v}, \frac{\Delta z}{w})$). The instantaneous results are monitored regularly and the convergence is achieved when the instantaneous values appear periodically.

The bluff body burner is set in an open space . The co-flow air surrounding the burner is set to have a uniform initial velocity of 35 m/s. The flow velocity at the outside boundary is also set to 35 m/s. This value should remain unchanged during the simulation to ensure that the inner regions are not affected by any external forces.

5.5 Results and Discussion

In this section, the comparison between the results from different SGS turbulence and combustion models will be presented first. This is to illustrate the improvement achieved by the dynamic approach and MLFM, respectively. In additional to those by the Smagrinsky model, the predictions by the dynamic approach are further compared with data from previous CFD simulations [124,127,142,145] and large eddy simulation [144].

5.5.1 Comparison Between the Two SGS Turbulence Approaches

For the comparison here, the MLFM is used as the SGS combustion model. As shown in Fig. 5.2 where the radial distance is normalised by the bluff body radius, the dynamic approach shows some improvement over the Smagorinsky model and other CFD simulations [127, 145] for the predictions of the axial velocity distributions at different heights. Overall, the predictions using the Germano's approach are marginally closer to the experiments data than the Smagorinsky model. The discrepancy between the dynamic approach and the Smagorinsky model is relatively bigger at the low height (z/D = 0.06) where the flow is believed to be going through the laminar to turbulence transition. It is difficult for the Smagorinsky model with a constant coefficient to capture the flow characteristics in those regions [72, 99]. Quantitatively, the dynamic approach has improved the accuracy of prediction on axial velocities by up to 15% near the fuel jet. Both sets of predictions are, however, slightly lower than the experimental data. This may be partially because the modelling structure of the dynamic approach is still based on the Smagorinsky model and the mechanism of representing energy backscattering is to some extent still restricted. When it reaches the main reaction zone in the re-circulation region at z/D=1 and 1.2, the advantages of the dynamic approach have been highlighted by the comparison with previous CFD simulations. Although Merci *et al* [127] did a fairly good job in

predicting the radial distribution of axial velocity at z/D=1, the dynamic approach manages to compensate the underestimation by adjusting the model coefficient instantaneously. At the height of z/D=1.2, Muradoglu *et al* [145] underpredicted at most of the radial positions, especially near the centreline. This was due to the relatively poor ability of representing the flow movement in laminar regions for constant-coefficient SGS turbulence models. It is well believed that in laminar/transient regions a considerable amount of energy is born in small scale quantities and the Smaorinsky-like SGS turbulence models are usually too dissipative. Possessing the mechanism of representing the energy backscattering and adjusting the model coefficient according to the local velocities and time, the dynamic approach has made a remarkable improvement by refining the predictions up to 25%. After all it has to point out that the complex nature of the re-circulating flows in those regions may have caused further difficulty in both the numerical computations and experiments.

In Fig. 5.3 the advantages of the dynamic approach are further demonstrated by comparing the distribution of radial velocities at different heights (normalised by the bluff body diameter) with those from the Smagorinsky model and other CFD simulations [127, 145]. All of the simulation results exhibit similar distribution of radial velocity as the experimental measurement [134] at almost all the studied heights. At lower heights (z/D=0.06 and 0.2), radial velocity near the centreline remains close to zero as there is little combustion and air entrainment occurring in that region. The horizontal movement of flow is generated by the pressure gradient caused by the axial velocity difference of fuel jet and the surrounding air. Although applying a new cubic model, Merci *et al* [127] did not produce satisfactory simulation results of centreline velocity at z/D=0.2. Slightly doing better, Muradoglu *et al* [145] also experienced the

discrepancy of axial velocity prediction near the fuel jet. In the reaction zone (z/D=1.0 and 1.2) all models behave similarly with Merci *et al* [127] and Muradoglu *et al* [145] being too dissipative. While in the fully developed turbulence area (z/D=2.4), relatively big discrepancy exists in the outer radius between the previous CFD results [127, 145] and the experimental data [134]. Not surprisingly, the predictions of the Germano's dynamic approach are generally in closer (up to 30%) agreement with the data especially in the re-circulation zone (within one to two burner diameter). The distribution of radial velocities represents the air entrainment and turbulence mixing. These results demonstrate the reliability of the current modelling approach in capturing the physics of air entrainment.

The comparative predictions of the mean temperature at different heights are shown in Fig. 5.4. Although the velocity of the fuel jet is high, there is an initially stagnation region between the central fuel jet and the co-flow air. The flow is believed to be within the laminar to turbulent transition region at the lower height at z/D=0.2. The Smagorinsky model gives relatively poor prediction because it is difficult to capture the flow characteristics with a constant coefficient in that region [72, 99]. Although Merci *et al* [127] generated reasonable predictions, the dynamic approach gives better predictions at z/D=0.2 for almost all the radial locations. Vertically, the improvements are more distinctive at the laminar regions. At height z/D=0.2, the dynamic approach has refined the predictions by up to 35% percent. While in the re-circulation zone, an overall 5-10% improvement is observed. At z/D=1.0 and 1.2, the predictions of previous CFD simulations [124, 127, 142] are generally lower than the experimental data, which is in accordance with the characteristic of being dissipative for Smagorinsky-like models. Particularly at z/D=1.2, the results from a 2-D large eddy simulation are

presented [144]. Being slightly over-dissipative near the centreline, the 2-D LES managed to give encouraging results at the outer region. For all the studied heights, the LES with dynamic approach shows a remarkable improvement on predicting the mean temperature. This improvement is particularly distinctive near the centreline.

Similar to the temperature predictions, the dynamical approach gave better predictions of the mixture fraction as shown in Fig. 5.5. At all heights the predictions from the dynamic approach were in good agreement with the experimental data while the Smagorinsky model under-predicted it. The largest discrepancy of 20% percent was found at radial positions between 1-9mm, where the majority of combustion took places.

To give more straightforward view on the dynamic approach, the calculated dynamic coefficient was illustrated spatially and temporally in figs. 5.6 and 5.7. The values in fig. 5.6 were ensemble averaged. In the contour of the dynamic coefficient (fig. 5.6a), the general values of the dynamic coefficient at all heights were smaller than the constant 0.17, which was adopted by the Smagorinsky model. This proved that the dynamic approach had made the SGS turbulence model less dissipative, which was strongly supported by the improvement on the predictions of mean flow variables. In the radial distribution (fig. 5.6b), the dynamic coefficient was larger at lower heights (laminar/transitional regions), showing that the flow characters were not that universal and a considerable part of kinetic energy in this region was stored in small-scale vortices. The values of the dynamic coefficients decreased considerably to around 0.06 when approaching the reaction zone (z/D =1 and 1.2). This was due to the interactive enhancement of turbulence and combustion, which caused the majority of

energy born by turbulence. When reaching the fully developed turbulence area (z/D = 1.8 and above), the values of the dynamic coefficient became vertically stable and the radial difference started vanishing. This represented that turbulence turned to dominate the flow and the flow field was getting more homogeneous. In fig. 5.7, instantaneous values of the central line dynamic coefficient at the height of z/D=1.2 were recorded. The instantaneous values exhibited a stable oscillation around an average value of 0.06, with some values appearing negative. This demonstrated that the coefficient behaved flexibly with the time and it had the mechanism to represent the energy backscattering.

5.5.2 Comparison Between the Two SGS Combustion models

To ensure consistency, the Germano's dynamic approach is used for turbulence closure along with both SGS combustion models here. As the main difference between the MLFM and the mixture fraction model is the lack of SGS contribution in the later, the difference of the results is expected to be more significant in the turbulence area rather than the lower laminar and transition region. This is supported by the computed results of temperature, mixture fraction, velocity and heat release rate.

The predictions of axial and radial velocity distributions are shown in Figs. 5.8 and 5.9, respectively. In Fig. 5.8, there is not much difference in the axial velocity predictions between the two combustion models. This is partly due to the dominant effect of the high speed of the fuel jet and co-flow air. The only exception happens at the heights of z/D = 1 and 1.2 within the reaction zone where the effect of combustion chemistry is expected to be most significant, the mixture fraction model over-predicts

the axial velocity within the mixing zones by up to 30%. At lower heights (e.g. z/D = 0.06 and 0.2), there are steep gradients of axial velocity at the inner edge of the co-flow air (r/R = 1). There is a region between the fuel jet and co-flow air where the axial velocity is zero indicating that the fluid still remains to be accelerated by combustion. With the increase of height, more air is entrained into the central region and accelerated by the hot combustion products. When the height reaches the extinguishing zone (z/D = 4.4), where most combustion has completed, the velocities at all radial positions become more uniform due to the decay of turbulence.

The story of mean radial velocity is slightly different. As shown in Fig. 5.9, the biggest difference between the predictions of the two models is located at the inner edge of the co-flow air (r/R = 1). In the reaction zone and lower heights, both models achieve better agreement with the experimental data in the region between the central fuel jet and the co-flow air ($0.2 < r/R < 0.6$). The predictions of the mixture fraction model (absolute values) are slightly higher at all heights. The magnitudes of the radial velocities are generally much smaller than that of the axial velocity. This would make the radial velocity more sensible to the influence of the evolution of large eddies. This disturbance is expected to be smaller in the central cone where the fuel jet velocity has dominant effect.

The comparison of the mean temperature is shown in Fig. 5.10. At all five heights, the temperature predictions of the mixture fraction model are lower than those of the MLFM. This may be attributed to the fact that the heat release rate is only calculated from the fuel in the former. The discrepancy increases outside the reaction zone. Although both models gave reasonably good predictions in comparison with the

experimental measurement within the fully developed turbulence region (z/D = 1 and 1.2), the modified laminar flamelet model gives better predictions in the transition region (z/D = 0.06).

Similar profile could be found in the comparison of heat release rate per unit volume (HRRPUV). As seen in Fig. 5.11, the HRRPUV at 5 different heights were listed. Due to the unavailability of published experimental data, only the predictions are presented. The distribution of HRRPUV exhibits higher axis-symmetry outside the reaction zone (z/D = 0.06, 0.2 and 4.4) while it is more likely to be affected by the turbulence mixing in the reaction zone (z/D = 1 and 1.2). Starting from the bluff body burner base, the radial location of peak HRRPUV is moving towards the centre of the fire as more combustion takes place in the centre. While it is reaching the extinguishing zone, the magnitude of HRRPUV decreases. At z/D = 4.4, the majority of combustion ceased. The HRRPUV at the radial position of 18mm is a result of some remaining chemical reaction. Both models predict similar distributions with the predictions of the mixture fraction model being slightly higher. This is expected as the inclusion of heat loss by the generation of combustion products in eq. 82 brings down the total amount of HRRPUV.

The comparison of mixture fraction is shown in Fig. 5.12. At the lower heights (z/D = 0.06 and 0.2), both simulation results give good agreement with the experimental data. In the re-circulation region at z/D = 1 and 1.2, the MFLM gives better prediction. The difference between the predictions of the MLFM and the experimental data are mainly located in the middle of the radial positions, while in the inner region near the fuel jet and the outer region near the co-flow air, the differences are marginal. At all heights,

the mixture fraction model gives lower predictions than the MLFM. This may be partially explained by the fact that in the mixture fraction model, the SGS contribution is only included in the filtered equation and these is no SGS term in the transport equation of ξ.

5.5.3 Predictions of the Flame Structure

5.5.3.1 Velocity

The instantaneous axial velocity vectors are presented in Fig. 5.13 where two groups of vortices can be clearly seen near the bluff body burner, one close to the fuel jet and the other close to the co-flow air. These vortices are formed due to the pressure difference between the flow streams and the initially still air above the bluff body burner. The vortex near the co-flow air is smaller than that near the fuel jet because the co-flow air velocity is smaller than the fuel jet velocity and there is less combustion taking place. The existence of two vortices is supported by the previous experimental observation of Dally et al [138] and it is also in line with the observation of double flame [134, 139, 139]. Also in agreement with the experimental observation, the length of the re-circulation zone is found to be about one to two diameters.

The distributions of mean axial velocities at different height are shown in Fig. 5.14. At radial positions less than 0.08, the axial velocity is as high as 126 m/s in the centre of the fuel jet, close to the burner surface. This is largely due to the acceleration caused by the sudden drop of pressure. In the outer region (r/R >1), where the co-flow air is, the axial velocity tends to have a uniform distribution of 35 m/s, as initialised by the boundary condition. With the height increasing, the peak value of the axial velocity along the central line decreases. This is a combined result of the combustion-

driven outward expansion and gravity. As more air is entrained into the reaction zone, mixing with the fuel and facilitating the combustion, more vortices are generated and developed due to turbulence mixing and chemical reaction, which slows down the fuel jet velocity. In separate study about pool fires, a so-called "neck-in" region has been observed at the height of about one pool diameter [99]. At the "neck-in" region the visible flame shrinks because of the high intensity of vortices generated. Similar structure is observed here at the height of one diameter, showing the location of the highest reaction rate. The only exception occurs at z/D=1.2, where the centreline axial velocity is slightly higher than that at z/D=1. This trend was also observed in the experiment as shown in Fig. 5.2 [134]. It may be due to the high intensity of the vortex movement generated in the region.

In the middle radial positions ($0.15<r/R<1$), the axial velocities start with negative values, showing that the air is being "pushed" towards the bluff body burner due to the high flow speed at both sides. The air in the affinity to both streams (fuel and co-flow) turns upward, while the air direction in the very middle part ($0.4 < r/R < 0.8$) remains downward. This distribution of velocity indicates the existence of vortices generated by the high-speed side-flows along the bluff body burner. The "negative" region for axial velocity gets smaller and smaller with the heights and disappears at the height of $z/D = 1.8$ representing the end of the re-circulation. At the heights over 4 times of the diameter, the axial velocities at all radial positions become nearly uniform at around 30 m/s.

The distribution of mean radial velocities at different heights is shown in Fig. 5.15. There are considerable differences between the distributions of radial velocities at

lower heights and that in the higher regions. The negative value represents the flow coming into the domain while the positive values showing the opposite direction. At a height of z/D=0.06, the radial velocity is mainly affected by the high-speed up-ejecting flows at both sides. Due to the initially parabolic distribution of axial velocities at the exit of the fuel orifice, the radial velocities within the small inner region close to the central fuel jet are negative with a very small magnitude. The majority of the air entrainment occurs at a radial position of 2.5mm (r/R = 0.1), just outside the fuel jet. The radial velocity reaches as high as 4 m/s. This is because of the low pressure inside the fuel jet vacuumed by the high-speed fuel stream. At the outside region ($0.8 < r/R < 1$), air is being "expelled" out for similar reason.

With the height increasing, the surrounding air in the region close to the central fuel jet is expanding outwards due to the high intensity of chemical reactions, while more co-flow air is entrained into the reaction zone for the combustion. During the process of combustion, the temperature of the mixture is increasing; more vortices are generated and evolving, turning the flow into turbulence. The maximum radial velocity can reach up to 4 m/s. And the turning point of radial velocity, where the outgoing and incoming air meet, is at the same radial position of r/R = 0.6 for all the heights below z/D = 2.

Above z/D = 2, most of the combustion completes and the axial velocity is becoming more uniform with the main flow stream moving upwards due to buoyancy. As shown in Figs. 5.3, 5.9 and 5.15, the radial velocities at z/D = 2.4 are close to zero at all radial positions as consistent with the characteristics of the extinguishing zone which starts approximately from the height of z/D = 2.2 according to the present prediction.

5.5.3.2 Temperature

Four instantaneous snapshots of temperature contours are listed in Fig. 5.16. It can be clearly seen that the main part of chemical reaction occurs between the fuel jet and co-flow air, at a height lower than 1-1.5 times of bluff body diameter. This region is usually referred to as the "re-circulation zone". Further down the re-circulation zone, there is little reaction and the temperature gradient decreases due to mixing with the cold air. At the far end, the radial distribution of temperature tends to be uniform and close to the ambient value. The snapshots also reveal that the temperature distribution exhibits a high degree of axis-symmetry.

The temperature distribution at different heights is shown in Fig. 5.17. The mean temperatures at all heights have a similar radial distribution. The lowest temperature occurs in the centre, where the fuel jet is and there is little air mixed with the fuel to facilitate the combustion. The temperature increases along the radius and drops to the ambient value in the co-flow stream. At the radial positions between the fuel jet and co-flow air, the temperature reaches its highest value, indicating the existence of chemical reactions. The peak value of around 2000K is found at z/D = 1. Another quantity that can be used to measure the strength of chemical reaction is the difference between the highest and lowest temperature at the same height. This comparison is made by using the temperature at r = 0 (usually the lowest one) and the peak value of temperature at that certain height. The temperature values at r > 20mm are not considered because they are described as boundary conditions and should remain the ambient value regardless of the combustion. At the reaction zone (z/D = 1), the difference between the highest and lowest temperatures is about 1500K, and the

temperature gradient near the reaction zone is steep. At the lower heights (z/D = 0.06 and 0.2), where fuel and air are still mixing and less combustion happens, the temperature difference is less (about 1200K). In the extinguishing zone (z/D = 4.4), where most of the combustion ceases, the radial distribution of temperature tends to be uniform and the temperature variation is as small as 410K.

Another typical characteristic of the bluff body burner flame is that the radial position of peak temperature is moving outwards with the heights until it reaches the reaction zone, and then moving back towards the centre when approaching the extinguishing zone. At the height of z/D = 0.2, the peak temperature of 1600K is found at r = 15mm. At the height of z/D = 1, the peak position moves to r = 20mm. Finally at the height of z/D = 4.4, the radial position for the peak temperature moves back to the radial position of 12mm. This is in line with previous experimental observations [128, 138-141]. At the lower height the mixing of fuel and air is controlled by molecular diffusion while higher up it is controlled by turbulence mixing. More vortices are generated and evolving, speeding up the mixing and reaction process. The stoichiometric line of mixture fraction is then moving outwards, causing the location of the highest intensity of combustion and highest temperature to shift accordingly. After the majority of combustion completes, the turbulence is driven by the density stratification caused by the temperature difference. Hot air is quickly mixed with the surrounding cold air, leading to more uniform temperature distributions.

Similar to the predicted axial velocity in Fig. 5.14, the centreline temperature at z/D = 1.2 is slightly lower than that at z/D = 1 as predicted by the simulation. At the higher

region (z/D = 4.4) where the flow is fully developed turbulent and the majority of the combustion ceases, the temperature tends to be uniform at all radial locations.

The existence of double flame observed by Masri *et al* [139] can be seen from the contour of mean temperature in Fig. 5.18. The outer flame is located at a radial position about 15mm and the inner flame is near the centre of fuel jet. The scale of outer flame is larger than the inner one and the two flames tend to mix in the reaction zone. At the far side of downstream, the coarse contour lines indicate the homogeneous distribution of temperature. It is also seen that the temperature distribution exhibits a fair axis-symmetry.

5.5.3.3 Mixture Fraction

Similar to that of the mean temperature, the mixture fraction in Fig. 5.19 has an axis-symmetric distribution as well. The stoichiometric mixture fraction is about 0.25. The mixture fraction in the central fuel jet is close to 1 near the burner surface, where little air is mixed with fuel. It decreases with height as more air is entrained in and more fuel consumed. At the height about one and a half times of bluff body diameter, where the re-circulation zone exists, the mixture fraction near the central fuel jet drops to almost the stoichiometric value of 0.25, indicating that most of the combustion takes place in this region. In addition to the mean temperature contour, the double flame and two homogeneous mixture zones observed by Masri and his colleagues [138, 139] are also supported by the mixture fraction contour in Fig. 5.20 where close to stoichiometric mixture fraction values are seen in the regions of the double flame above the burner surface as well as in the inner core. Near the burner surface, the stoichiometric value of mixture fraction is in the outer region between the central fuel

jet and the co-flow air (15mm < r < 25mm). Within the heights between 50mm and 70mm, the mixture fraction in the centre of the flame is around the stoichiometric value, indicating that the majority of combustion takes place within the reaction zone. These predicted regions of stochiometric mixture fraction value coincide with those of the maximum predicted temperatures.

At the lower heights (Z/D = 0.06, 0.2 and 0.6), the fuel/air mixing is mainly controlled by diffusion and the process is relatively slower than further up where turbulent mixing dominates. As a result, very pointed distributions of mixture fraction are seen in the lower height. Little oxygen has penetrated into the region near the central fuel jet and the mixture fraction is as low as 0.12 near the centre which is below the flammability limit.

It is also seen from the contour of mean mixture fraction that the mixing rate of fuel and air occurs very close to the burner and decreases very quickly outwards. This is in accordance with the fast combustion assumption. For equilibrium combustion, however, more complicated distribution of mixture fraction is expected.

5. 6 Concluding Remarks

Details of the downstream flow structure generated by a bluff body burner are studied using the large eddy simulation techniques. In line with previous experimental observations, the analysis of temperature, velocities and mixture fraction demonstrates the existence of re-circulation and extinguishing zones. The former exists at a height of 1-1.5 times of burner diameter, where most of the combustion takes place and the combustion process is mainly controlled by turbulent mixing. As

the ratio of the fuel orifice to the burner diameter is fairly small (0.07) and the combustion is treated as infinitely fast reactions, the mixture fraction reaches its stoichiometric value quickly in the re-circulation zone. Little fuel is left to penetrate into the extinguish zone so no re-ignition zone is observed. The experimentally observed double flame phenomenon is also numerically demonstrated.

Quantitatively, the predicted distributions of the axial and radial velocities, the temperature and mixture fraction are all in generally good agreement with the experimental data with the only exceptions being the temperature at low heights close to the burner surface (z/D = 0.2) and the axial velocity distribution at z/D = 1.2 in the re-circulation region. The discrepancy could be possibly attributed to the great uncertainties in the flow and combustion in those regions and the difficulties associated with capturing them.

Comparison has also been carried out to evaluate the effect of SGS turbulence and combustion modelling. For comparison of the SGS turbulence models, the MLFM is used as the SGS combustion model and the same grid resolution is used. Some predictions of previous CFD and LES simulations [124,127,142,144,145] are also included. It is found that in the laminar and transitional regions at the lower heights and in the re-circulation region where the combustion is most intense, the Smagorinsky model and previous CFD simulations under-predict the velocity and temperature. Germano's dynamic approach generated up to 10% improvement on the prediction of velocity fields in the re-circulation zone. While in terms of mean temperature, the maximum improvement figure raised to 20%. The most severe under-predictions on mixture fraction occur in the re-circulation region and amount to around 35%. Having a

mechanism to determine the model coefficient from local and up-to-date flow variables, Germano's dynamic approach achieves reasonably good predictions at all locations for both velocity and temperatures. In the post-flame extinguishing region, however, the differences between the two models are marginal.

For comparison of the SGS combustion models, Germano's dynamic approach is used for SGS turbulence closure and again the same grid resolution is used. Although both models have achieved reasonably good agreement with the experimental data and correctly predict the distribution trends of velocity, temperature and mixture fraction, the MLFM has demonstrated its potential to improve the predictions. This is, in particular, reflected in the predictions on the axial velocities in the re-circulation region where the mixture fraction model over-predicts the velocity by up to 30% and in the radial velocities where up to 15% discrepancies are seen between the prediction of the mixture fraction model and that of the MLFM which is generally very close to the experimental data. Relatively little difference is seen between the predictions of temperature and mixture fraction. In summary, both models are considered as capable of offering sufficient accuracy for the current application while the predictions of the MLFM are marginally closer to the experimental data.

Overall, the study has demonstrated that the present LES approach with the dynamic SGS turbulence closure and the MLFM is capable of capturing some fine details of the flame and flow characteristics of the bluff-body flames and achieve quantitatively good predictions with the experimental data. It has also demonstrated that with the multi-blocking facility, significant savings can be made in CPU time through the reduction in grid numbers without affecting the accuracy of the predictions.

Chapter 6 Conclusion and Recommendations

6.1 Concluding Remarks

This dissertation aims at the development and application of SGS turbulence and combustion models in the large eddy simulation of turbulent diffusion flames and pool fires, from which the importance of SGS modelling in large eddy simulation can be summarised into the following fields.

Rapid increase of the demand of detailed research on small-scale movement inside the flows has accelerated the development of SGS modelling. It has been widely acknowledged that traditional RANS approaches (or other similar CFD techniques) inevitably lose the information about instantaneous fluctuations, which leads to the damage of accuracy in simulation predictions. LES has made a systematic improvement by capturing the on-the-spot flow information. The instantaneous update within each computational cell during the calculation is made available by modelling the SGS movement. Theoretically speaking, the less amount of movement that needs modelling, the better simulation results are expected. Due to the current limitation of computer capability, however, full-scale calculation for high-Reynolds-number flows is unpractical and the modelling of SGS movements becomes a compulsory requirement and a critical component for LES. Although it has been argued that the SGS modelling may be ignored if the filtering process is accurate enough, the omission is suitable only for certain applications and cannot be used as a general treatment. Especially when studying the small-scale flows, the absence of SGS contribution could lead to a considerable degree of discrepancy (see Chapter 4). The

effectiveness and efficiency of SGS modelling are of special importance to the predictions.

Another aspect that highlights the importance of SGS modelling is the involvement of chemical reactions. In additional to the SGS turbulence modelling, the SGS combustion modelling is also a critical issue in the current research. The typical length scale of combustion is much smaller than the smallest resolvable computational cell, making the direct simulation of industrial combustion practically impossible at the current stage. A SGS combustion model that properly describes the chemical process plays a determining role on fire simulations. An appropriate model should monitor the reaction process in a reasonable manner and give good description on the consumption/production rate of reactants/products. The actual air entrainment and vortex generation should also be properly represented. During the LES, the accuracy of predictions relies considerably on the interaction between the SGS turbulence model and the SGS combustion model.

From the detailed work illustrated in previous chapters, the concluding remarks can be established as following:

1. Large eddy simulation (LES) has been proved to be an appropriate technique for the numerical simulation of both non-reacting and reacting flows. For non-reacting flows, LES can be used to simulate high-Reynolds-number flows or flows with complicated geometries. In combustion-involved flows, LES has been found to predict the dynamic behaviours of fires and plumes effectively by the interaction of combustion and turbulence. The LES simulation results have been

compared with those from traditional CFD simulations and the advantages have been well addressed. The systematic improvement in LES by capturing the instantaneous movement has been well illustrated by the simulations in Chapters 3, 4 and 5. Accelerated by the rapid development of modern computers, LES is believed to dominate the numerical simulation of various types of flows.

2. LES of pool fires have been practised by some researchers in the last decade. Although pioneered experimentally by Weckman [76,98], Cetegen [74,78,103,107] and Venkatesh [109], the detailed numerical analysis of the dynamic behaviour of pool fires is still rare. By using time-averaging and turbulence models, traditional CFD models have successfully captured the mean characters of various kinds of high-Reynolds flows. However, the involvement of empirical models has limited the wider use of a certain CFD model. The time-averaging process could also kill the instantaneous fluctuations, which are very important to the analysis of the dynamic behaviours of pool fires (such as pulsation and air entrainment). When combining with chemical reactions, the turbulence contains even wider a range of scales of movement. As the physical scale of combustion is generally much smaller than that of turbulence, the traditional CFD is systematically unable to catch the tiny scale movement of chemical reaction, which makes it inappropriate for the simulation of pool fires. The current research has made an encouraging attempt to dig into the internal dynamics of such reacting flows by applying LES. Under the help of powerful computers, the smallest single cell with a dimension of 2mm is directly solvable. The combustion is represented by the assembly of thin flames (flamelets) and is well interacted with the turbulence.

3. The impact of grid resolution on the accuracy of prediction has to be addressed. The filtering process employed in LES determines both the calculation efficiency and the accuracy. Coarse resolution or the irregular shape of computational cells could depress the vortices and lead to unreliable predictions. On the other hand, too fine a mesh could make the calculation expensive, unstable, or even infeasible. The compromise of efficiency and effectiveness has become a critical issue in large eddy simulations. The actually employed grid resolution is determined by the requirements of each individual case and the available computer resources. Apart from that, a successful SGS model should also be grid-independent. There is a certain level of grid resolution for each individual case. Grid resolutions coarser than that level could lead to inaccurate or even faulty predictions. On the other hand, the accuracy of simulation results does not increase as much as the computational expense does when the grid resolutions are reaching much finer than the level. The determination of that level depends on the physical description of each individual case, the purpose of the research and the computer capability. In previous chapters, a series of sensitivity study has been carried out and the above conclusion has been strongly supported. Under the current computer capability (2GB RAM and 80GB HDD), up to 2 million cells could be employed in a large eddy simulation on a pool fire, subject to the data collection. From the work in previous chapters, a mesh with less than 1 million cells was considered coarse and may lead to an inaccurate simulation.

4. Boundary conditions are essentially important when defining a fire scenario. Due to the complexity of the interaction between combustion and turbulence, it would be wise to start the fire simulation with cases that have fairly simple and well-

defined boundary conditions to ensure that main interests of the flow field inside the fire are covered. Under this consideration, pool fires in open air and turbulence diffusion flames such as bluff body flames are chosen for the simulation application. For pool fires in open air, all the five other boundaries (apart from the ground) in a Cartesian co-ordinates are set open. The computational domain is set large enough, subject to the computer capability, to ensure that the flow field is not affected by the undefined external forces. The flow parameters at the computational boundaries should remain stable and undisturbed during the simulation. For a bluff body flame, the layer of co-air should be thick enough and the air velocity at the boundary is expected to be uniform for the purpose of isolation. In the data analysis in Chapters 3, 4 and 5, the boundary conditions are seen to be kept well.

5. Dynamic approach of SGS turbulence modelling has been proved to be a successful outbreak in terms of improving the simulation accuracy of high-Reynolds number flows. Although the double filtering process increases the computational expense and could possibly lead to the instability of calculation or some unrealistic results, the dynamic determination of model coefficient solves the systematic shortcoming of EVM and highlights the future of SGS modelling.

   The dynamic approach has been applied to the SGS turbulence modelling for the simulation of bluff body flames (see Chapter 5). Comparing to those from Smagorinsky modelling, the simulation results from the dynamic approach are encouraging. The better determination on the model coefficient results in the improvement of prediction accuracy.

6. Description of combustion is one of the critical issues in fire simulations. As stated before, the description of fire in the current research has experienced a progress from the "thermal particles" to "mixture fraction". Well acknowledged by the fire simulation society, the conserved scalar mixture fraction is good at representing the chemical procedures. Although the very details of the chemical reaction are still not clear at the current stage, the chemical process is believed to be controlled by the mixing of fuel and oxidant. Particular to pool fires (and other fire scenarios set in the open environment), a proper description of air entrained into the system and mixed with the fuel is of determining importance to an appropriated simulation (see Chapter 3). Although in Chapter 4 it was found that the flow field of small pool fires is more or less axially symmetric, the non-symmetry of flow field for medium/large pool fires (as revealed in Chapter 3) has shown that the arbitrary prescription of boundary conditions risks in misleading the simulation results. Although the application of the mixture fraction is fulfilled by some assumptions/simplifications (i.e. stoichiometric combustion only), the simulation results are promising (see Chapters 3, 4 and 5).

7. Interaction between SGS turbulence modelling and SGS combustion modelling generates a major part of difficulties existed in the large eddy simulation of fire scenarios. The heat released by chemical reaction affects the distribution of temperature, velocity and other quantities thereafter. The undated distribution of flow variables will also mutually affect the chemical process. The different temporal and spatial scales of turbulence and combustion and the limitation of resolvable scales in numerical calculation make the direction calculation of the

interaction numerically difficult. In the modified laminar flamelet model, the calculation of turbulence is by some means separated from that of combustion. In the LES calculation, main flow variables including the mixture fraction are calculated according to the governing equations. While in the LFM calculation, a look-up table is constructed linking the species concentration to the mixture fraction. Once the mixture fraction is determined temporally and spatially from the LES calculation, the corresponding species concentration of reactants/products can be located in the look-up table. The thermodynamic pressure is used to link the enthalpy/temperature to the mixture fraction/species concentration. Thereafter flow variables including temperature and density are updated by the species concentration for the next iteration in the LES calculation.

8. Originally the look-up table constructed in the LFM calculation is three dimensional with ξ, ξ_v and χ as independent inputs. During the numerical coding and testing, it has been found that comparing to the mixture fraction ξ, ξ_v and χ have less magnitude of importance in locating the corresponding species concentration. Furthermore, calculating ξ_v and χ from their governing equations could cause the whole calculation unstable or generate some unreasonable results. In the simulations carried out in this research, both ξ_v and χ were obtained from the modelling by the mixture fraction. The simulation results have proved that those modelling approaches are reasonable for the fire simulations.

9. In Chapter 4 it has been demonstrated that LES could be successfully applied to the prediction of the dynamic behaviours of small size pool fires. Similar numerical analysis on small pool fires had seldom been done due to the strict

requirement on the mesh resolution. Although the FDS code was originally designed for the simulation of large size fires, it has managed to capture the instantaneous movement of small pool fires with some necessary modifications. During the current research, LES has visualised some unique characters of small pool fires (flame anchoring, double flames and axial symmetry), which cannot be done with traditional CFD techniques. The mesh dimension inside the fire could be refined to less than 2mm, which is comparable to the experimental measurements.

10. The numerical coding and programming is the practical technique to put the SGS modelling into the practice of real simulation. As mentioned above, the difficulties in the grid resolution and computer capacity bring the potential risk of instability into the real calculation. As stated in Chapter 1, the increase of the ratio between the largest calculable scale to the smallest one could increase the computational expense dramatically. Hence a good program should be able to cope with a wide range of computational scales at a reasonable efficiency. Another parameter that could slow down the calculation is the number of requested solutions. In FDS codes, as many as 5 variables can be recorded instantaneously. Other variables (up to 12) can be recorded for the averaged values at the time of stopping the program. However, full recording of those 17 variables requires much more computer cache, which could result in a longer calculation for the same case.

The CPU time step is decided and automatically adjusted by the grid resolution and the local velocities (CFL criteria). When the CPU time step becomes very

small (under the magnitude of 10^{-3} order), the simulation program turns vulnerable. Experience from the previous simulations (Chapters 3,4,5) shows that the refinement of grid resolution is constrained by the CPU time step. Too fine a grid mesh could reduce the CPU time step, which increases the calculation burden and risks an unstable simulation.

Although the dynamic approach has successfully reduced the dependence on the empirical constants for SGS turbulence modelling, the SGS combustion modelling is still restricted by the numerical method. The mixture fraction, its variance and the scalar dissipation rate are supposed to be independent inputs to the look-up table. All of those three parameters are expected to run for a full range expected by the physical phenomena before completing the look-up table. Due to some numerical limitations (see Chapter 2), however, some of the values are unreasonable for the numerical calculation.

6.2 Recommendations

6.2.1 Optimisation and Extension Use of the Dynamic Approach

Although in Chapter 5 the dynamic approach of SGS turbulence modelling has managed to demonstrate its advantage in capturing the dynamic behaviours of the reacting flow, the increase of the computational expense could limit its application to flows with higher Reynolds number flows. There could be a broad room for the numerical optimisation of the dynamic approach for certain flows (axially symmetrical, pipe flows and periodic flows, etc.) to make the calculations more efficient. Similar consideration could be applied to the extension use of the dynamic approach to the complex geometry flows. Also, the pioneer work of

applying the dynamic approach to the SGS combustion modelling should be evaluated by the computational expense and stability. The current difficulty for the dynamical approach of SGS combustion modelling is the lack of resolved quantities of chemical reaction.

6.2.2 Extension of FDS codes

The FDS codes produced by NIST aim at simulating large size fire scenarios. The governing equations in FDS have been simplified accordingly, which could possibly make the simulation accuracy drop when dealing with small fires. In the future work, the FDS codes should be enriched with new characters to cope with small fires. There have been many improvements done in FDS codes such as the involvement of mixture fraction, radiation transport equations (RTE) and the multi-block grid resolution. The further enrichment would consist of the appropriate filtering process, the inclusion of SGS contribution, the cylindrical co-ordinate and the solution to complicated boundary conditions.

6.2.3 Improvement on SGS Combustion Modelling

The interaction between the combustion and turbulence has become a critical issue in fire modelling. Although the separation of SGS combustion modelling from the SGS turbulence modelling made considerable contribution to the simplification of calculation, more work needs to be done to analyse the details of above interaction. Currently many of the SGS combustion models take the similar formulation as that of eddy viscosity turbulence models. This formulation is programming friendly and could also be further improved by the application of dynamic approach. However, the foundation of that similarity is always being

challenged. Other forms of SGS combustion modelling should also be evaluated and the independence from the SGS turbulence modelling could possibly lead to the breakthrough of SGS combustion modelling.

References,

1. Moin, P., *Progress in Large Eddy Simulation of Turbulent Flows*, Internal Report, American Institute of Aeronautics and Astronautics, U.S.A., 1997.
2. McGrattan, K. B., Baum, H.R., Rehm, R.G., Hamins, A.,Forney, G.P., Floyd, J.E. and Hostikka, S., *Fire Dynamics Simulator (Version 2) – Technical Reference Guide*, NIST report number: NISTIR 6783, January 2001.
3. Quintiere, J., A prospective on compartment fire growth, *Combustion Science and Technology*, **39**:11-54 (1984).
4. Forney, G.P. and Moss, W.F., Analysing and exploiting numerical characteristics of zone fire models, *Fire Science and Technology*, **14**:49-60 (1994).
5. Launder, B.E. and Spalding, D.B., *Mathematical Models of Turbulence*, Academic Press, London (1972).
6. Patankar, S.V., *Numerical heat Transfer and Fluid Flow*, Hemisphere Publishing, New York (1980).
7. Liu, F. and Wen, J.X., The effect of turbulence modelling on the CFD simulation of buoyant diffusion flames, *The Fire Safety Journal*, **38**(2): 125-151 (2002).
8. Boussinesq, J., Theorie de l'dcoulement tourbillant, *Mem. Pre. Par. Div. Sav*, **23** (1877).

9. Launder,B.E. and Spalding, D.B., *Mathematical Models of Turbulence*, Academic Press (1972).

10. Wilcox,D.C., Reassessment of the scale-determining equations for advanced turbulence models, *AIAA J.*, **26:**1299-1310 (1988).

11. Speziale, C.G.,Abid, R. and Anderson, E.C., Critical evaluation of two-equation models for near-wall turbulence, *AIAA J.*, **30:**324-325 (1992).

12. Annarumma, M.O., Most, J.M. and Joulain, P., On the numerical modeling of buoyancy-dominated turbulent vertical diffusion flames, *Combustion and Flame*, **85**:413-415 (1991).

13. Woodburn, P., *PhD Thesis*, University of Cambridge, (1995).

14. Liu, F. and Wen, J.X., Development and validation of an advanced turbulence model for buoyancy driven flows in enclosures, *Int. J. of Heat and Mass Transfer*, **42**: 3967-3981 (1999).

15. Liu, F. and Wen, J.X., CFD Simulation of Buoyant Fire Plumes with a Buoyancy Modified Turbulence Model, *Interflam 99*, pp. 963-977, July 1999.

16. Bardina, J., Ferziger, J.H. and Reynolds, W.C., Improved subgrid scale models for large eddy simulation, *AIAA Paper* **80**-1357(1980).

17. Deardorff, J.W., A numerical study of pseudo three-dimensional parallel-plate convection, *Journal of Fluid Mechanics*, **22**:419-435 (1965).

18. E. C. Itsweire, J. R. Koseff, D. A. Briggs and J. H. Ferziger, Turbulent in stratified shear flows: Implications for interpreting shear-induced mixing in the ocean, *J. Phys. Oceanogr.* **28**:1508 (1993).

19. Rogallo, R.S. and Moin, P., *Ann.Rev.Fluid. Mech.*, Numerical simulation of turbulent flows, **16**, 99 (1984).

20. Reynolds, W.C., The potential and limitations of direct and large eddy simulation, In Whither turbulence at the crossroads, *Lecture Notes in Physics* (Ed. J.L.Lumley), **357**:313-343 (1989).

21. Schumann, U., Subgrid length-scales for large-eddy simulation of stratified turbulence, *Theoret. Comput. Fluid Dyn.*, **2**:279-290 (1991).

22. Ferziger, J.H., Higher level simulations of turbulent flow in computational methods for turbulent, transonic and viscous flows, *J.-A. Essers*, Ed., Hemisphere,1983.

23. Ferziger, J.H., Large Eddy Simulation, *Simulation and Modelling of Turbulent Flows*, Eds. M.Y.Hussaini and T.Gatski, Cambridge University Press,1996

24. Breuer, M. and Rodi, W., Notes on numerical Fluid Mechanics, Vieweg Verlag, Braunschweig, **52**:258-274 (1996b).

25. Shi, X.G., Turbulence, Tian Jin University Press, Tian Jin, China, 1994.

26. Smagorinsky, J., General circulation experiments with the primitive equations, Part I. The basic experiment, *Monthly Weather Review*, **91**:99-152 (1963).

27. Vreman B., Geurts B. and Kuerten H., Large eddy simulation of turbulent mixing layer, *J.Fluid Mech.*, **339**:357-390 (1997).

28. Miyauchi, T., Tanahashi, M. and Kakuwa, T., Evaluation of Energy Transfer between Grid Scale and Subgrid Scale by Use of Direct Numerical Simulation Data Base, *JSME International Journal*, Series B, **41**(3):343-350 (1997).

29. Morinishi, Y. and Kobayashi, T., *Proceedings of the fourth European Turbulence Conference*, 1992, pp. 279-286

30. Kang, Y., Wen, J.X., Lo, S.H., McGrattan, K.B. and Baum, H.R., Numerical Investigation of the Turbulence Structure of a Medium-Scale Methanol Pool Fire,

3rd International Seminar of Combustion and Explosion Hazard, Lake District, England, April 2000.

31. Clark, R.A., Ferziger, J.H. and Reynolds, W.C., Evaluation of subgrid-scale models using an accurately simulated turbulent flow, *J.Fluid Mech.*, **91**:1-16 (1979).

32. Liu, S., Meneveau, C. and Katz, J., On the properties of similarity subgrid-scale closure models as deduced from measurements in a turbulent jet, *J. Fluid Mech.*, **275**:83-119 (1994).

33. Deardorff, J.W., A numerical study of three-dimensional turbulent channel flow at large Reynolds numbers, *J. Fluid Mech.*, **41**: 453-480 (1970).

34. Deardorff, J.W., On the magnitude of the subgrid scale eddy coefficient, *J. Comput. Phys.*, **7**:120-133 (1971).

35. Bilger, R.W., In Topics in Applied Physics, *Springer-Veriag, Berlin*, **44** (1980)

36. Vreman, B., Geurts, B. and Kuerten, H., *Journal of Engineering mathematics*, 1995, vol. 29, pp. 299-327

37. Germano, M., Piomelli, U, Mion, P. and Cabot, W.H., A dynamic subgrid-scale eddy viscosity model, *Phys. Fluids* A **3**(7):1760-1765 (1991).

38. Sinai, Y.L., Exploratory CFD modelling of pool fire instabilities without cross-wind, *Fire Safety Journal*, **35:**51-61 (2000).

39. Branley, N. and Jones, W.P., An efficient method for large eddy simulation of turbulent, *Proceedings of the 11th Symposium on Turbulent Shear Flows*, **21**:1-6 (1997).

40. Colucci, P.J., Jaberi, F.A., Givi, P. and Pope, S.B., Filtered density function for large eddy simulation of turbulent reacting flows, *Phys. Fluids* **10**:499-515 (1998).

41. Fureby, C., Lundgren, E. and Moller, S.I., Detailed simulations of pulsating combustion, *Proceedings of the 25th Symposium (International) on Combustion*, Combustion Institute, Pittsburgh, PA , pp. 1257-1264 (1994).

42. Givi, P., Model-free simulation of turbulent reacting flows, Prog. *Energy Combust. Sci.* **15**:1-107 (1989).

43. Kerstein, *A.R.*, A linear-eddy model of turbulent scalar transport and mixing, *Combust. Sci. and Tech.*, **60**:391-421 (1988).

44. Cook, A.W. and Riley, J.J., A subgrid model for equilibrium chemistry in turbulent flows, *Physics Fluids,* **6**(8):2868-2870 (1994).

45. Veynante, D and Poinsot, T., Reynolds Averaged and Large Eddy Simulation Modelling for Turbulent Combustion, *Turbulence and Combustion,* Lecture 5, pp. 105-141.

46. McMurtry, P.A., Menon, S. and Kerstein, A.R., A linear eddy subgrid model for turbulent reacting flows: application to hydrogen-air combustion, *Twenty-fourth symposium (International) on combustion*, pp.271-278. (1992).

47. Kerstein, A.R., Linear-eddy modelling of turbulent transport. 6. Microstructure of diffusive scalar mixing fields, *J.Fluid Mech.* **231**:361-394 (1991).

48. Lilly, D.K., A proposed modification of the Germano subgrid-scale closure method, *Phys. Fluids* A **4**(3):633-635 (1992).

49. Gao F., O'Brien E.E., A large eddy simulation scheme for turbulent reacting flows, *Phys. Fluids* **5**(6):1282-1284 (1993).

50. Cook, A.W., Riley, J.J. and Kosaly, G., A laminar flamelet approach to subgrid-scale chemistry in turbulent flows, *Combustion and Flame*, **109**:332-341 (1997).

51. Cook, A.W. and Riley, J.J., Subgrid-scale modeling for turbulent reacting flows, *Combustion and Flame*, **112**:593-606 (1998).

52. Huggett, C., Estimation of the rate of heat release by means of oxygen consumption measurements, *Fire and Materials*, **4**:61-65 (1980).

53. Rehm, R.G. and Baum, H.R., The equations of motion for thermally driven buoyant flows, *Journal of Research of the NBS*, **83**:297-308, 1978.

54. Frankel, S.H., Adumitroaie, V., Madnia, C.K., and Givi, P., Enginering Applications of Large Eddy Simulations, *Fluids Engineering Division, ASME*, **162**:81-101 (1993).

55. Lentini, D., *Comb. Sci. Tech.*, 1994, vol.100, pp. 95-122

56. Pope, S.B., The statistical theory of turbulent flames, *Phil. Trans. R. Soc. London*, **291**:529-568 (1979).

57. Peters, N., Laminar diffusion flamelet models in non-premixed turbulent combustion, *Prog. Energy Comb. Sci.* **10**:319-339 (1984).

58. Schmidt, H., and Schumann, U., Coherent structure of the convective boundary layer derived from large-eddy simulations, *J. Fluid Mech.* **200**:511-562 (1989).

59. Girimaji, S.S., and Zhou, Y., Analysis and modeling of subgrid scalar mixing using numerical data, *Phys. Fluids A* **8**:1224-1236 (1996).

60. Germano, M., Piomelli, U., Moin, P. and Cabot, WH, A dynamic subgrid eddy viscosity model, *CTR Manuscript* 116, Stanford University, (1990).

61. Piomelli, U., High Reynolds number calculation using the dynamic subgrid-scale stress model, *Phys. Fluids*, A **5:**1484-1490 (1993).

62. Cabot, W., Large eddy simulations of time-dependent and buoyancy-driven channel flows, *CTR Annual Research Briefs*, pp.45 (1992).

63. Sullivan, P. and Moeng, C.H., *Proceedings of the 10th Symposium on Turbulence and Diffusion*, Portland, Oregon, pp. 82 (1992)

64. Canuto, V.M., Dubovikov, M.S. and Dienstfrey, A., A dynamic model for turbulenc IV. Buoyancy-driven flows, *Phys. Fluids* **9** (7):2118-2131 (1997).

65. Zang, Y., Street, R.L. and Koseff, J.R., A dynamic mixed subgrid-scale model and its application to recirculating flows, *Phys. Fluids*, A **5**:3186-3196 (1993).

66. Bohnert, M. and Ferziger, J.H., The dynamic subgrid scale model in large-eddy simulation of the stratified Ekman layer, *Proceedings of the 2nd International Symposium on Engineering Turbulence Modelling and Measurements*, Florence, Italy, (1993).

67. Moin, P., Squires, K., Cabot, W. and Lee, S., A dynamic subgrid-scale model for compressible turbulence and scalar transport, *Phys. Fluids* A **3**(11):2746-2757 (1991).

68. Wong, V.C. and Lilly, D.K., A comparison of two dynamic subgrid closure methods for turbulent thermal convection, *Phys. Fluids* **6** (2):1017-1023 (1994).

69. Cook, A.W. and Riley, J.J., Direct numerical simulation of a turbulent reactive plume on a parallel computer, *J. Comput. Phys.*, **129:**263-283 (1996).

70. Pitsch, H., *Centre for Turbulence Research Annual Research Briefs*, (2000) pp.149-158.

71. Speziale, C.G., Younis, B.A., Rubinstein, R. and Zhou, Y., On consistency conditions for rotating turbulent flows, *Phys. Fluids* **10**:2108-2110 (1998).

72. Steiner, H. and Bushe, W.K., Centre for Turbulence Research Annual Research Briefs, (1998) pp. 23-34.

73. De Bruyn Kops, S.M., Riley, J.J., Kosaly, G., and Cook, A.W., Investigation of modeling for non-premixed turbulent combustion, *Flow, Turbulence and Combustion*, **60**:105-122 (1998).

74. Cetegen BM, Ahmed TA, Experiments on the periodic instability of buoyant plumes and pool fires, *Combustion and Flame* 93:157-184 (1993).

75. Hamins A, Yang JC and Kashiwagi T, An Experimental Investigation of the Pulsation Frequency of Flames, *Proceedings of the 24th International Symposium on Combustion*, Combustion Institute, pp. 1695-1702 (1992).

76. Weckman and Sobiesiak A, The oscillatory behaviour of medium scale pool fires, *Proceedings of the 22nd International Symposium on Combustion*, Combustion Institute, pp.1299-1310 (1988).

77. Malalasekera WMG, Versteeg HK and Gilchrist K, A review of research and experimental study on the pulsation of buoyant diffusion flames and pool fires, *Fire and Materials* **20**:261-271 (1996).

78. Cetegen BM, Behaviour of naturally unstable and periodically forced axisymmetric buoyant plumes of helium and helium—air mixtures, *Phys. Fluids* **9** (12):3842-3852 (1997).

79. Gebhart B, Instability, transition and turbulence in buoyancy-induced flows, *Ann. Rev. Fluid Mech.* **5**:213-246 (1973).

80. Mandin O and Most JM, *Proceedings of the 6th International Symposium on Fire Safety Science*, pp. 1138-1148 (1999).

81. Pagni PJ, Buoyancy effects on smoldering combustion, *App. Mech. Rev.* **43**:153-170 (1990).

82. Joulain P, The behaviour of pool fires: state of art and new insights, *Proceedings of the 27th International Symposium on Combustion*, Combustion Institute, pp.2691-2706 (1998).

83. Delichatsios MA, Gravitational fluctuations in pool fires and pool buoyant flows, *Combust. Sci. and Tech.* **112**:355-359 (1996).

84. Buckmaster J and Peters N, The infinite candle and its stability --- a paradigm for flickering diffusion flames, *Proceedings of the 21st International Symposium on Combustion*, Combustion Institute, pp.1829-1836 (1988).

85. Davis RW, Moore EF, Roquemore WM, Chen LD, Preliminary results of a numerical-experimental study of the dynamical structure of a buoyant jet diffusion flame, *Combustion and Flame*, **83** (3-4):263-270 (1991).

86. Blunsdon CA, Beeri Z, Malalasekera WMG, and Dent JC, Fire, Combustion and Hazardous Waste Processing, ASME (HTD-Vol. **296**) (1994).

87. Ghoniem AF, Lakkis I and Steriou M, Numerical simulation of the dynamics of large fire plumes and the phenomenon of puffing, *Proceedings of the 26th International Symposium on Combustion*, Combustion Institute, pp. 1531-1539 (1996).

88. Mell WE, Mcgrattan KB and Baum HR, Numerical simulation of combustion in fire plumes, *Proc. Combst. Institute*, **26**:1523-1530 (1996).

89. Jiang X and Luo KH, Combustion induced buoyancy effects of an axisymmetric reactive plume, *Proceedings of the 28th International Symposium on Combustion*, Combustion Institute, pp.1989-1996 (2000).

90. Jiang, X. and Luo, K.H., Spatial DNS of flow transition of a rectangular buoyant reacting free-jet, *Journal of Turbulence,* **2**:1-18 (2001)

91. Mell WE, Mcgrattan KB and Baum HR, Johnson SW abd Pitts WM, *Fall 1995 Western States Section meeting/Combustion Institute*, Standford, CA. http://odie.seas.ucla.edu/WSS/papers/f95F221.html

92. DesJardin P.E. and Frankel S.H., Large eddy simulation of a nonpremixed reacting jet: application and assessment of subgrid-scale combustion models, *Phys. Fluids*, **10** (9):2298-2314 (1998).

93. Baum HA, Mcgrattan KB and Rehm RG, Three dimensional simulations of fire plume dynamics, *Proc. 5th Int. Symp. Fire Safety Science*, pp. 511-522 (1997).

94. Baum HR and Mell WE, Radiative transport model for large-eddy fire simulations, *Combust Theory Modelling* **2** (4) 415-422 (1998).

95. Zhou, X, Luo KH and Williams JJR, Vortex dynamics in spatio-temporal development of reacting plumes, *Proceedings of the 28th International Symposium on Combustion*, Combustion Institute, pp.2859-2866 (2000).

96. Deardorff, J.W., A numerical study of three-dimensional turbulent channel flow at large Reynolds numbers, *J. Fluid Mech.* **41**:453-480 (1970).

97. Baum, H.R., McGrattan, K.B. and Rehm, R.G., Large eddy simulation of smoke movement in three dimensions, *Journal of Heat Transfer Society of Japan*, **35**:45-52 (1997).

98. Weckman, E.J. and Strong, A.B., Experimental investigation of the turbulence structure of medium-scale methanol pool fires, *Combustion and Flame*, **105**:245-266 (1996).

99. Kang, M.Y., Wen, J.X., McGrattan, K.B. and Baum, H. R., Use of a laminar flamelet approach in the large eddy simulation of flame structure at the base of a pool fire, *Interflam2001*, pp.743-754 (2001).

100. Delichatsios, M.A., Air entrainment into buoyant jet flames and pool fires, *Combustion and Flame*, **70** (1):33-46 (1987).

101. Delichatsios, M.A. and Orloff, L., Entrainment measurements in turbulent buoyant jet flames and implications for modelling, *Proceedings of the 20th International Symposium on Combustion*, Combustion Institute, pp.367-385 (1984).

102. Beyler, C.L., *Ph.D Thesis, Harvard University*, 1983.

103. Cetegen, B.M., Zukoski, E.E. and Kubota, T., Visible structure of buoyant diffusion flames, *Proceedings of the 20th International Symposium on Combustion*, Combustion Institute, pp.361-366 (1984)

104. Zhou, X.C. and Gore J.P., Air entrainment flow field induced by a pool fire, *Combustion and Flame*, **100**:52-60 (1995).

105. Hertzberg, M., Cashdollar, K., Litton, C. and Burgess, D., The diffusion flame in free convection, *US Bureau of Mines, Report Number RI8263,* 1978.

106. Brotz, W., Schonbucher, A., Barnhardt, V. and Schiess, N., *Ber. Bundesges. Phys. Chem.* 87, **997** (1983)

107. Cetegen, B., Phase-Resolved Velocity Field Measurements in Pulsating Buoyant Plumes of Helium-Air Mixtures, *Annual NIST Fire Research Conference*, Gaithersburg, MD (1994).

108. Bouhafid, A., Vantelon, J.P., Joulain, P. and Fernandez-Pello, A.C., On the flame structure at the base of a pool fire, *Proc. Twenty-Second Symposium (International) on Combustion*, The Combustion Institute, Pittsburgh, pp 1291-1298 (1988).

109. Venkatesh, S., Ito, A. and Saito, K., Flame base structure of small-scale pool fires, *Proc. Twenty-Sixth Symposium (International) on Combustion*, The Combustion Institute, pp.1438-1443 (1996).

110. Rehm, R. G. and Forney, G. P., Note on the pressure equations used in zone fire modelling, *NIST report NISTIR 4906,* NIST, USA (1992).

111. Hu, C. and Fukuchi, N., The characteristics analysis of turbulent heat diffusion in the multi-compartments structure, *The 95th Trans. Of the West-Japan Soc. Of Naval Architects*, **12**:209-217 (2001).

112. McCaffrey, B.J., Momentum implications for buoyant diffusion flames, *Combustion and Flame*, **52**:149-167 (1983).

113. Cox, G. and Chitty, R., A study of the deterministic properties of unbounded fire plumes, *Combustion and Flame*, **39**:191-209 (1980).

114. Takahashi, F. and Schmoll, W.G., *Proc. Twenty-Third Symposium (International) on Combustion*, The Combustion Institute, Pittsburgh, pp.677-683 (1990).

115. Chung, S.H. and Lee, B.J., On the characteristics of laminar lifted flames in a nonpremixed jet, *Combustion and Flame*, **86**:62-72 (1991).

116. Dold, J.W., Flame propagation in a nonuniform mixture: Analysis of a slowly varying Triple Flame, *Combustion and Flame*, **76:**71-88, (1989).

117. Wichman, I.S., On the quenching of a diffusion flame near a cold wall, *Combust. Sci. Technol.*, **64**:295-313 (1989).

118. Wichman, I.S., Basic Features of Triple Flames in Combustion Theory, 8th ISTP (1996).

119. Kang, Y., Wen, J.X.,, Large eddy simulation of a turbulent bluff-body burner flame, submitted to Flow, Turbulence and Combustion, (2003a).

120. Kang, Y., Wen, J.X., Large eddy simulation of the dynamic behaviour and structures of pool fires, submitted to Int. J. of Heat and Mass Transfer, (2003b).

121. Xu, M.H., Yuan, J.W., Han, C.Y. and Zheng, C.G., Investigation of particle dynamics and pulverized coal combustion in a cavity bluff-body burner, *Fuel*, **74**:1913-1917 (1995).

122. Wouters, H.A., Nooren, P.A., Peeters, T.W.J. and Roekaerts, D., Simulation of a bluff-body-stabilized diffusion flame suing second moment closure and Monte-Carlo methods, *Proceedings of the Twenty-Sixth Symposium (International) on Combustion*, pp. 177-185 (1997).

123. Jones, W.P. and Launder, B.E., The prediction of laminarization with a two-equation model of turbulence, *Int. J. Heat. Mass Transfer*, **15**:301-314 (1972).

124. Kim, S.H., Huh, K.Y. and Liu, T., Application of the elliptic conditional moment closure model to a two-dimensional nonpremixed methanol bluff-body flame, Combustion and flame, **120**: 75-90 (2000).

125. Lopes, J., Semiao, V. and Carvalho, M.G., On the effect of the local turbulence scales on the mixing rate of diffusion flames: assessment of two different combustion models, *International Journal of Energy Research*, **26**:893-920 (2002).

126. Martins, L.F. and Ghoniem, A.F., Simulation of the nonreacting flow in a bluff-body burner; Effect of the diameter ratio, *Transactions of the ASME*, **115**:474-484 (1993).

127. Merci, B, Dick, E., Vierendeels, J., Rokaerts, D. and Peeters, T.W.J., Application of a new cubic turbulence model to piloted and bluff-body diffusion flames, *Combustion and Flame*, **126**:1533-1556 (2001).

128. Pitsch, H. and Steiner, H., Large eddy simulation of a turbulent piloted methane/air diffusion flame (Sandia flame D), *Phys. Fluids*, **12**:2541-2554 (2000).

129. Shih, T.H., Zhu, J. and Lumley, J.L., Calculation of wall-bounded complex flows and free shear flows, *Int. J. Num. Methods Fluids*, **23**:1133-1141 (1996).

130. Sharif, M.A.R. and Gu, Z., Turbulent flow simulation behind a v-shaped flame stabilizer using a nonlinear K- ε model and a smoothing algorithm, *Chem. Eng. Comm.*, **189** (4):471-488 (2002).

131. Craft, T.J., Launder, B.E. and Suga, K., Development and application of a cubic eddy-viscosity model of turbulence, *Int. J. Heat Fluid Flow*, **17**:108-115 (1996).

132. Bilger, R.W., Conditional Moment Closure for Turbulent Reacting, *Phys. Fluids A.* **5**:436-444 (1993).

133. Klimenko, A. Y., Multicomponent diffusion of various admixtures in turbulent flow, *Fluid Dynamics*, **25**:327-334 (1990).

134. Masri, A.R., Dibble, R.W. and Barlow, R.S., The structure of turbulent nonpremixed flames revealed by Raman-Rayleigh-Lif measurements, *Prog. Energy Combust. Sci.* **22**:307-362 (1996).

135. Dally, B.B, Masri, A.R., Barlow, R.S., Fiechtner, G.J. and Fletcher, D.F., Measurements of NO in turbulent nonpremixed flames stabilised on a bluff body, *Twenty-Sixth International Symposium on Combustion*, The Combustion Institute, Pittsburgh, pp. 2191-2197 (1996).

136. Dally, B.B, Masri, A.R.and Fletcher, D.F., Modelling of turbulent flames stabilized on a bluff body, *Combustion theory and modelling*, **2**:193-219 (1998).

137. Dally, B.B., Masri, A.R., Barlow, R.S. and Fiechtner, G.J., Instantaneous and mean compositional structure of bluff-body stabilized nonpremixed flames, *Combustion and Flame* **114**:119-148 (1998).

138. Masri, A.R., Dally, B.B., Barlow, R.S. and Carter, C.D., The structure of the recirculation zone of a bluff-body combustor, *Proceedings of the Twenty-Fifth Symposium (International) on Combustion*, pp 1301-1308 (1994).

139. Masri, A.R., Kelman, J.B. and Dally, B.B., The instantaneous spatial structure of the recirculation zone in bluff-body stabilized flames, *Proceedings of the Twenty-seventh Symposium (International) on Comubstion*, pp.1031-1039 (1998).

140. Chen, R.H, Driscoll, J.F., Kelly, J., Namazian, M and Schefer, R.W., A comparison of bluff-body and swirl-stabilized flames, *Combust. Sci. Technol.* **71**:197-217 (1991).

141. Roquemore, W.M., Bradley, R.P., Stutrud, J.S., Reeves, C.M., Obringer, C.A. and Britton, R.L., Utilisation of Laser Diagnostics to Evaluate Combustor Models, *AGARD Propulsion and Energetics Panel*, Cesme, Turkey, (1983).

142. Hossain, M., Jones, J.C. and Malalasekera, W., Modelling of a Bluff-body Nonpremixed Flame Using a Coupled Radiation/Flamelet Combustion Model, *Flow, Turbulence and Combustion*, **67**:217-234 (2001)

143. Cox, G. and Chitty, R., Some Stochastic Properties of Fire Plumes, Fire and Materials, **6**:127-134 (1982)

144. Papailiou, D., Koutmos, P., Mavridis, C. and Bakrozis A, Simulations of local extinction phenomena in bluff-body stabilized diffusion flames with a Lagrangian reactedness model, *Combust. Theory Modelling*, **3**:409-431 (1999)

145. Muradoglu, M., Liu, K and Pope, S.B., PDF modelling of a bluff body stabilized turbulent flame, *Combustion and Flame*, **132** (1-2): 115-137 (2003)

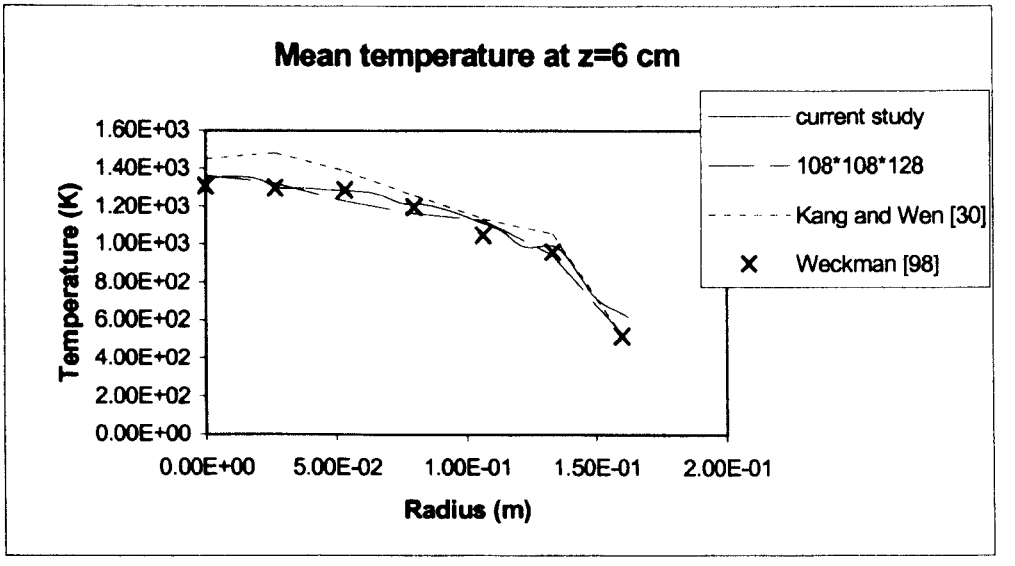
Mean temperature at z=6 cm
Temperature (K)
1.60E+03
1.40E+03
1.20E+03
1.00E+03
8.00E+02
6.00E+02
4.00E+02
2.00E+02
0.00E+00
0.00E+00
5.00E-02
1.00E-01
1.50E-01
2.00E-01
Radius (m)
current study
108*108*128
Kang and Wen [30]
Weckman [98]

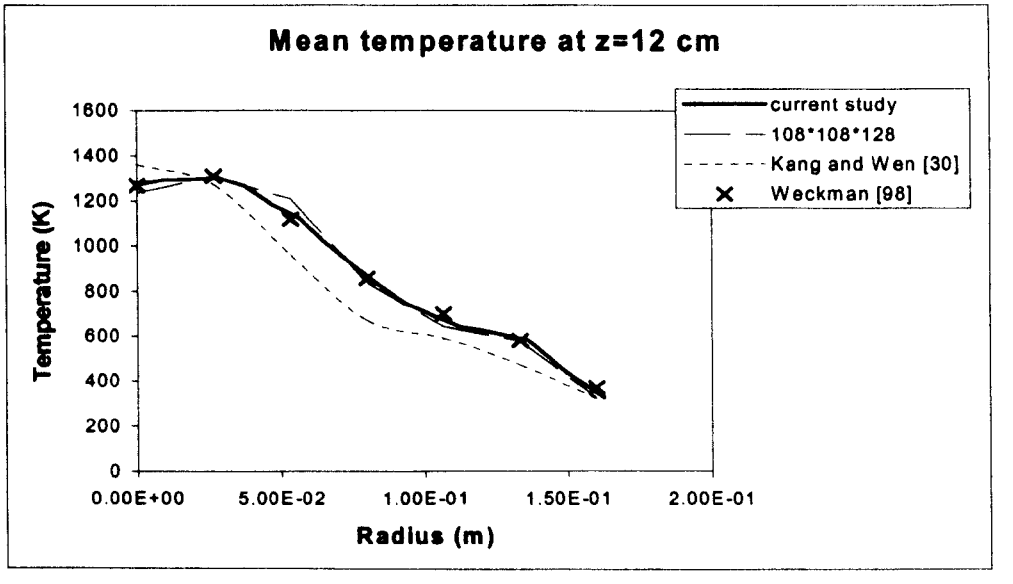
Mean temperature at z=12 cm
Temperature (K)
1600
1400
1200
1000
800
600
400
200
0
0.00E+00
5.00E-02
1.00E-01
1.50E-01
2.00E-01
Radius (m)
current study
108*108*128
Kang and Wen [30]
Weckman [98]

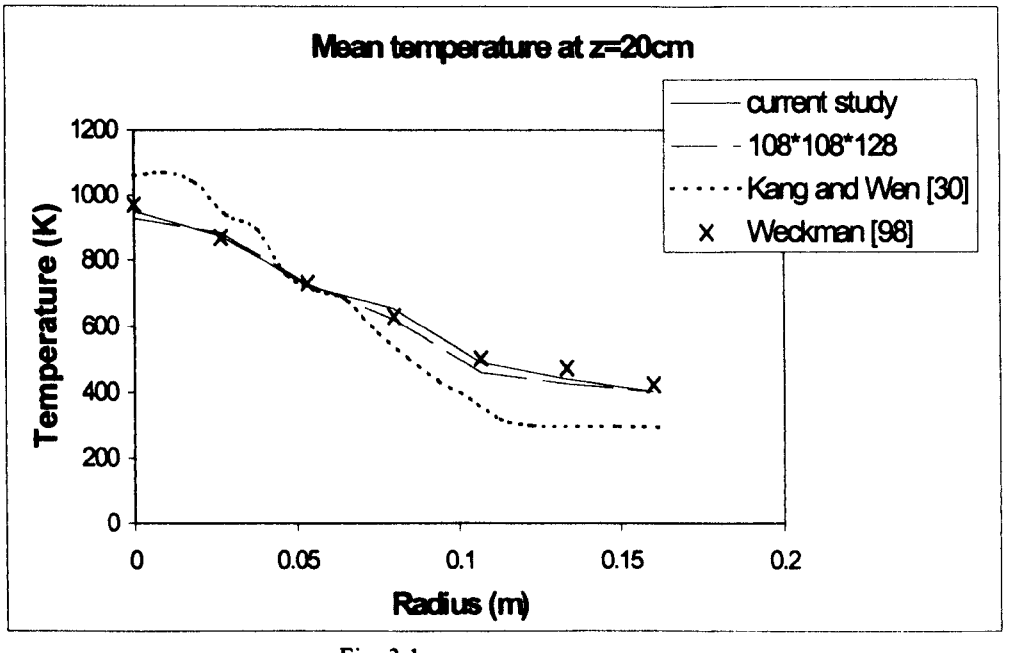
Mean temperature at z=20cm
Temperature (K)
1200
1000
800
600
400
200
0
0
0.05
0.1
0.15
0.2
Radius (m)
current study
108*108*128
Kang and Wen [30]
Weckman [98]

Fig. 3.1

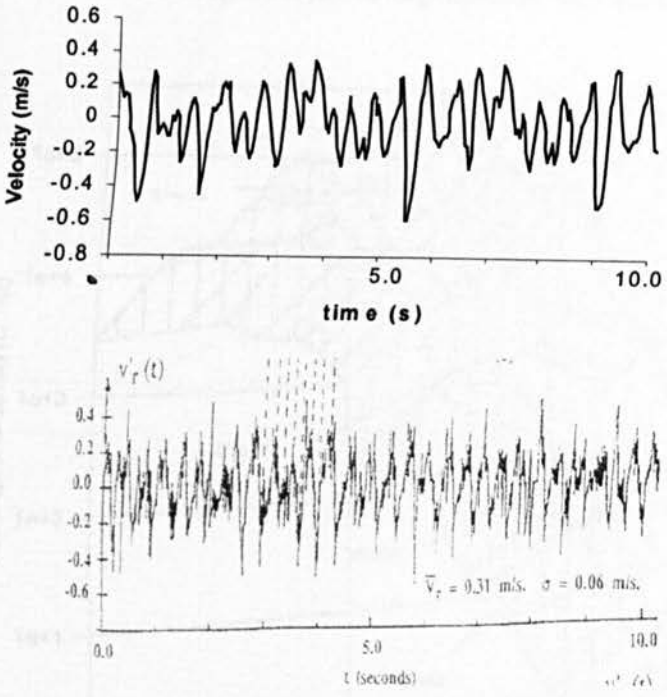

Fig. 3.2a(up: modified laminar flamelet model; below: experimental measurement [74])
p.s.: the starting point of 0 at the time axis represents the 10th second of simulation

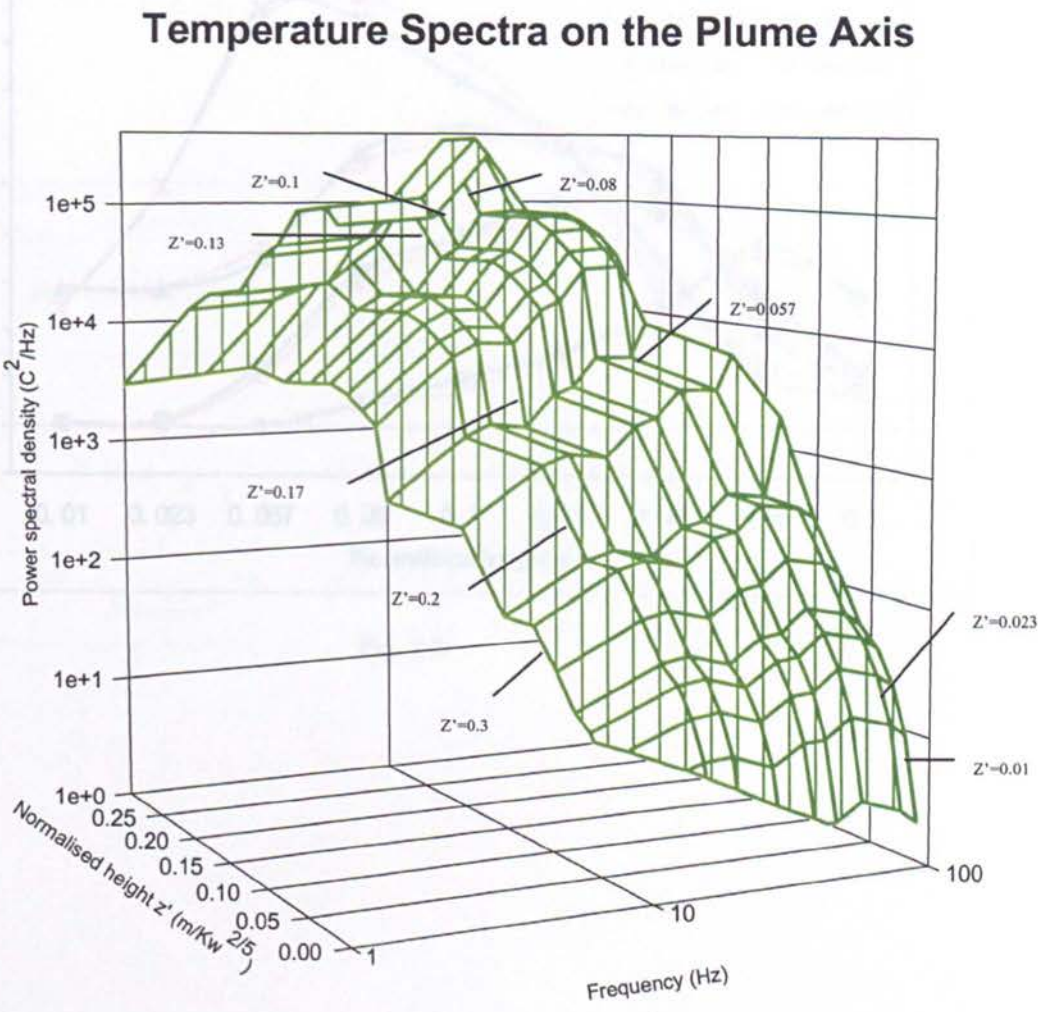
Temperature Spectra on the Plume Axis
Power spectral density (C^2/Hz)
1e+5
1e+4
1e+3
1e+2
1e+1
1e+0
Z'=0.1
Z'=0.08
Z'=0.13
Z'=0.057
Z'=0.17
Z'=0.2
Z'=0.023
Z'=0.3
Z'=0.01
Normalised height z' (m/Kw$^{2/5}$)
0.25
0.20
0.15
0.10
0.05
0.00
1
10
100
Frequency (Hz)

Fig. 3.2b

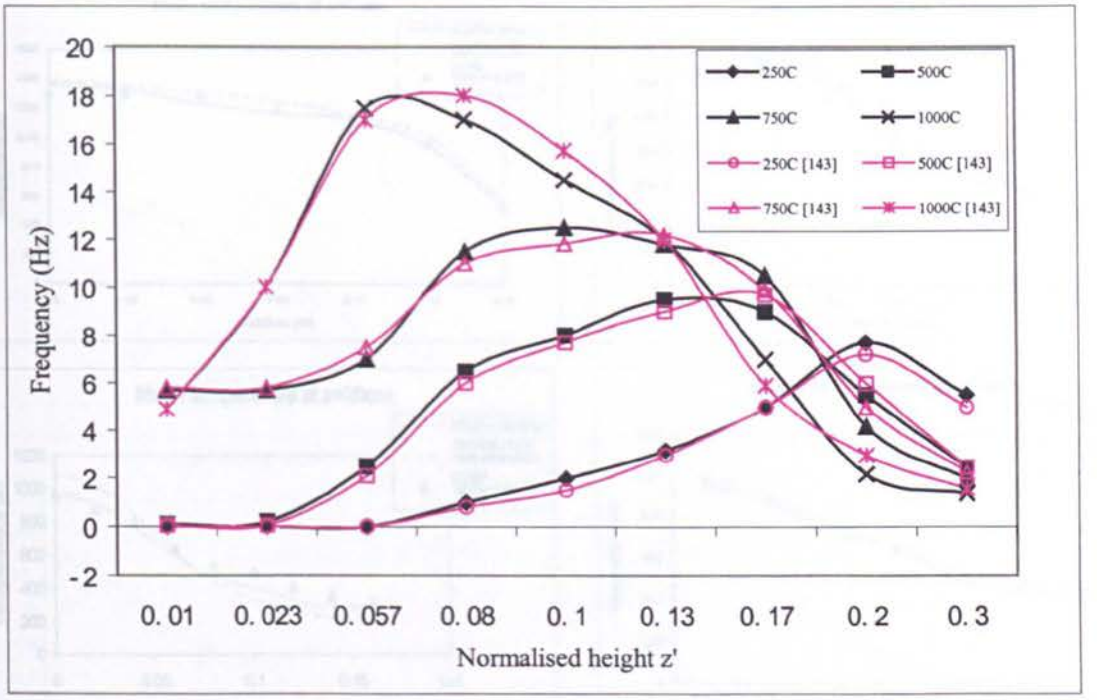
Frequency (Hz)
20
18
16
14
12
10
8
6
4
2
0
-2
0. 01
0. 023
0. 057
0. 08
0. 1
0. 13
0. 17
0. 2
0. 3
Normalised height z'
250C
500C
750C
1000C
250C [143]
500C [143]
750C [143]
1000C [143]

Fig. 3.2c

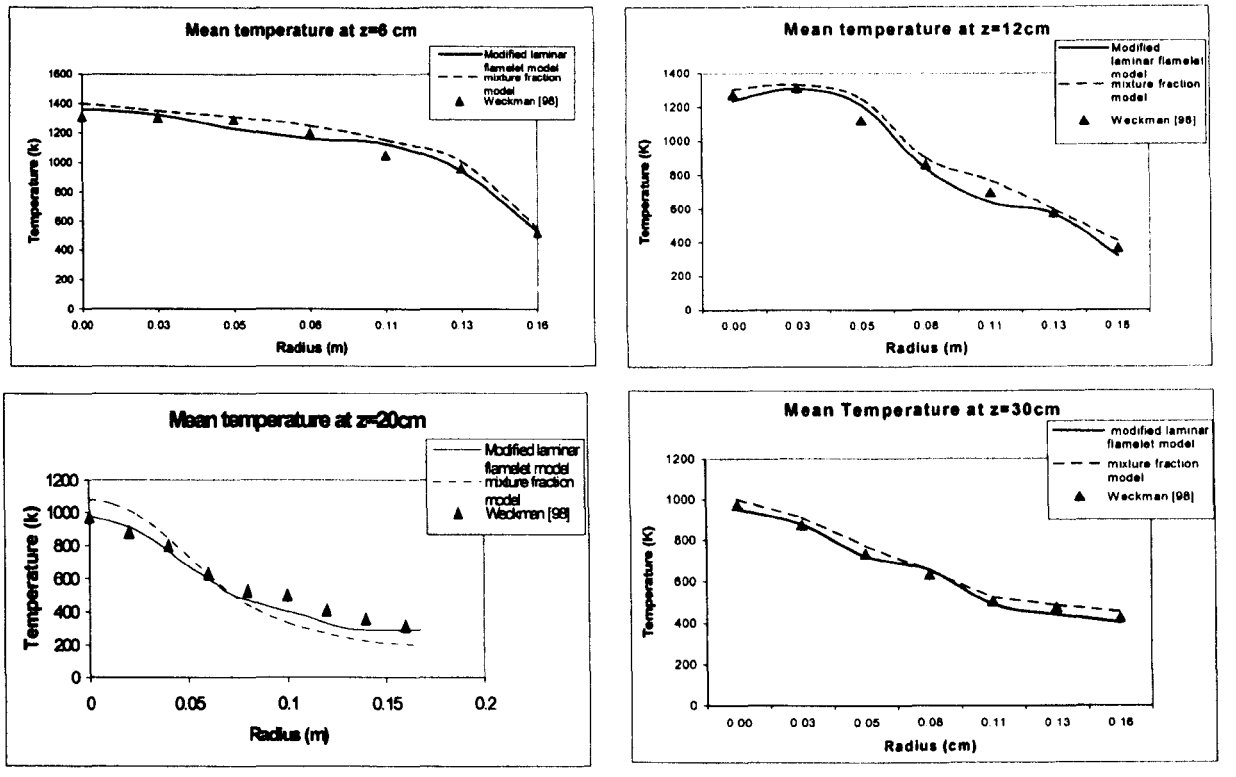
Mean temperature at z=6 cm
Modified laminar flamelet model
mixture fraction model
Weckman [98]
Temperature (k)
Radius (m)
Mean temperature at z=12cm
Modified laminar flamelet model
mixture fraction model
Weckman [98]
Temperature (K)
Radius (m)
Mean temperature at z=20cm
Modified laminar flamelet model
mixture fraction model
Weckman [98]
Temperature (k)
Radius (m)
Mean Temperature at z=30cm
modified laminar flamelet model
mixture fraction model
Weckman [98]
Temperature (K)
Radius (cm)

Fig. 3.3

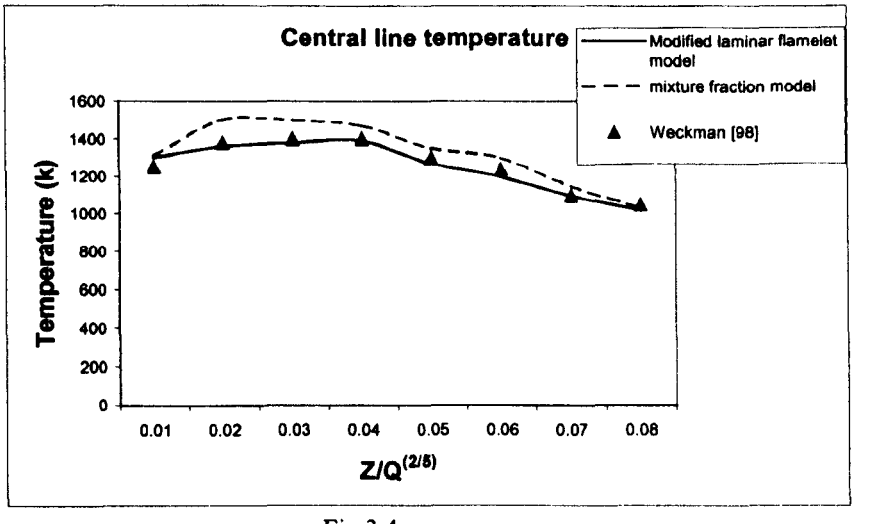
Central line temperature
Modified laminar flamelet model
mixture fraction model
Weckman [98]
Temperature (k)
Z/Q(2/5)

Fig 3.4

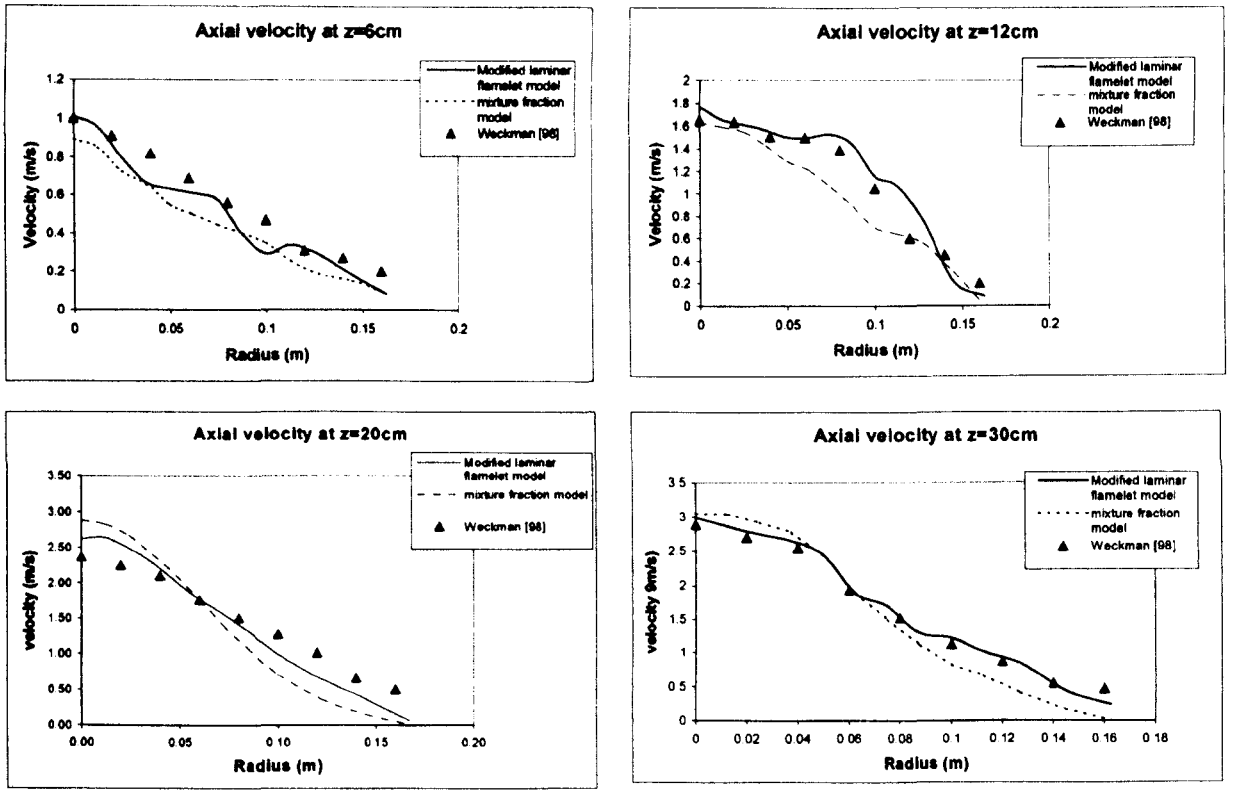
Axial velocity at z=6cm
Modified laminar flamelet model
mixture fraction model
Weckman [98]
Velocity (m/s)
Radius (m)
Axial velocity at z=12cm
Modified laminar flamelet model
mixture fraction model
Weckman [98]
Velocity (m/s)
Radius (m)
Axial velocity at z=20cm
Modified laminar flamelet model
mixture fraction model
Weckman [98]
velocity (m/s)
Radius (m)
Axial velocity at z=30cm
Modified laminar flamelet model
mixture fraction model
Weckman [98]
velocity (m/s)
Radius (m)

Fig. 3.5

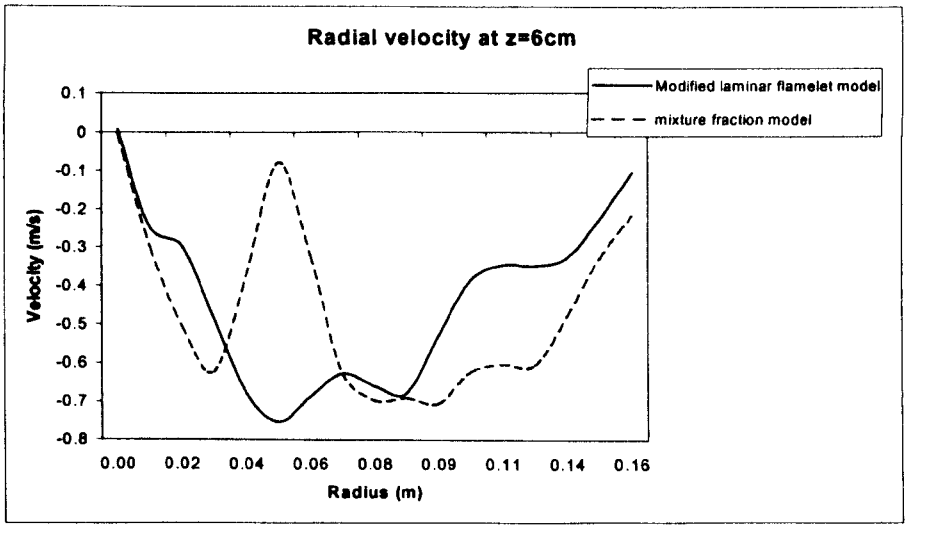
Radial velocity at z=6cm
Modified laminar flamelet model
mixture fraction model
Velocity (m/s)
0.1
0
-0.1
-0.2
-0.3
-0.4
-0.5
-0.6
-0.7
-0.8
0.00 0.02 0.04 0.06 0.08 0.09 0.11 0.14 0.16
Radius (m)

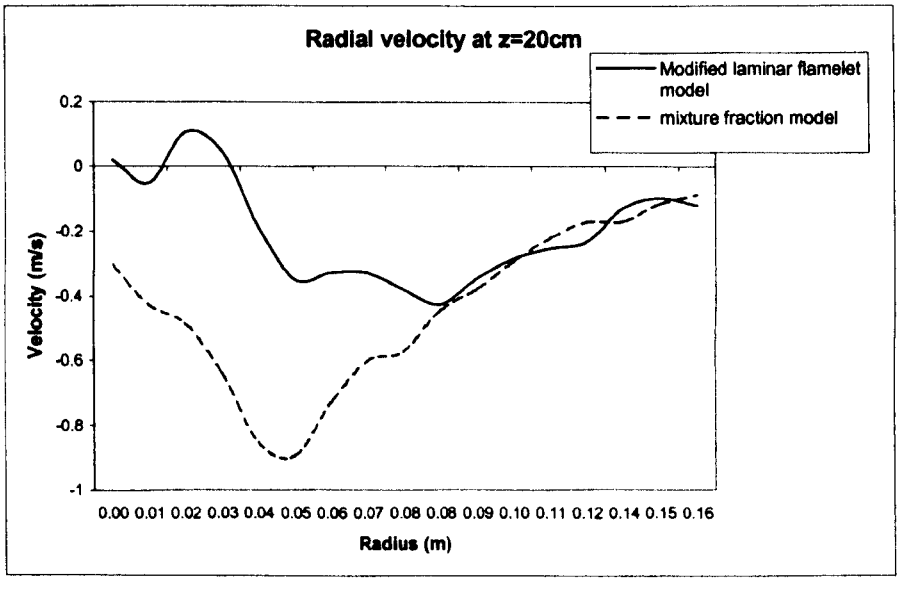
Radial velocity at z=20cm
Modified laminar flamelet model
mixture fraction model
Velocity (m/s)
0.2
0
-0.2
-0.4
-0.6
-0.8
-1
0.00 0.01 0.02 0.03 0.04 0.05 0.06 0.07 0.08 0.08 0.09 0.10 0.11 0.12 0.14 0.15 0.16
Radius (m)

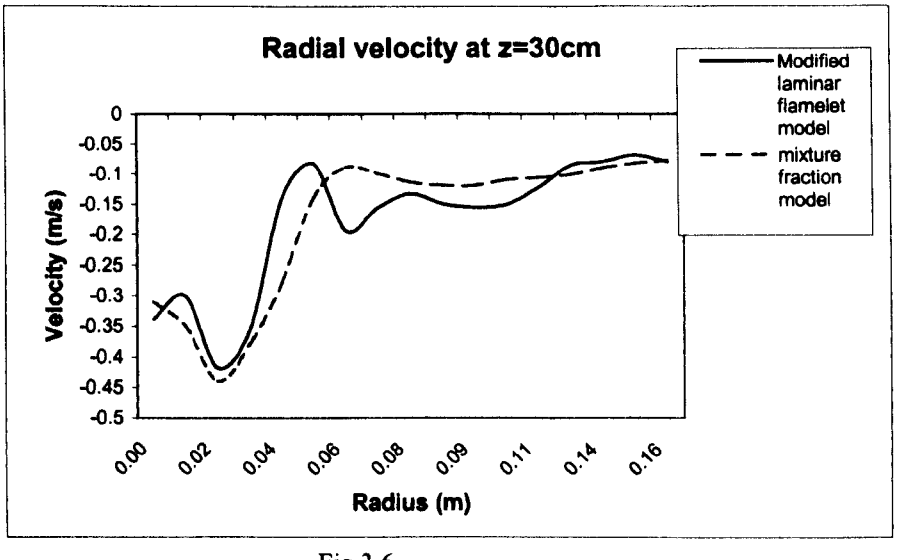
Radial velocity at z=30cm
Modified laminar flamelet model
mixture fraction model
Velocity (m/s)
0
-0.05
-0.1
-0.15
-0.2
-0.25
-0.3
-0.35
-0.4
-0.45
-0.5
0.00 0.02 0.04 0.06 0.08 0.09 0.11 0.14 0.16
Radius (m)

Fig 3.6

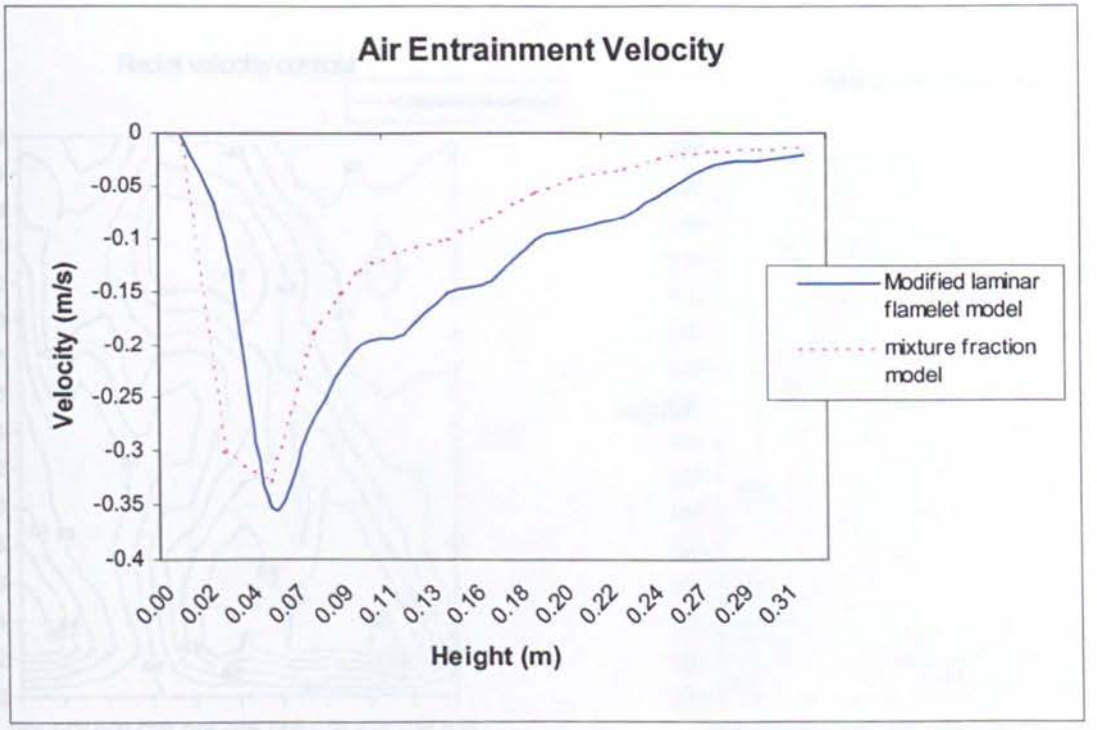
Air Entrainment Velocity
Velocity (m/s)
0
-0.05
-0.1
-0.15
-0.2
-0.25
-0.3
-0.35
-0.4
0.00
0.02
0.04
0.07
0.09
0.11
0.13
0.16
0.18
0.20
0.22
0.24
0.27
0.29
0.31
Height (m)
Modified laminar flamelet model
mixture fraction model

Fig 3.7

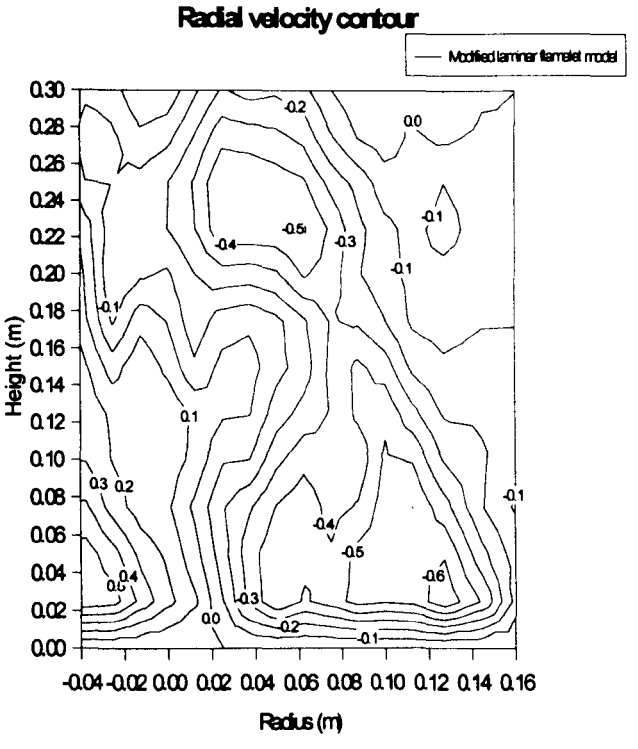

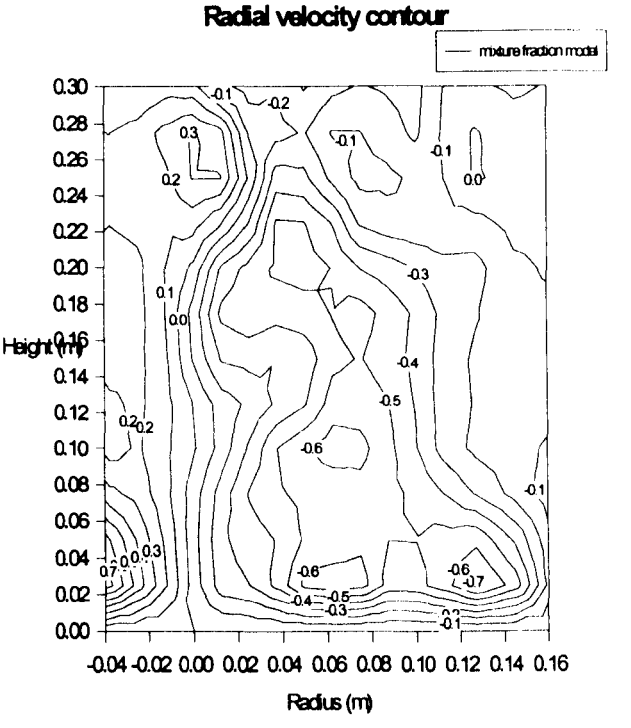

Radial velocity Contour

Experimental measurement (Weckman [98])

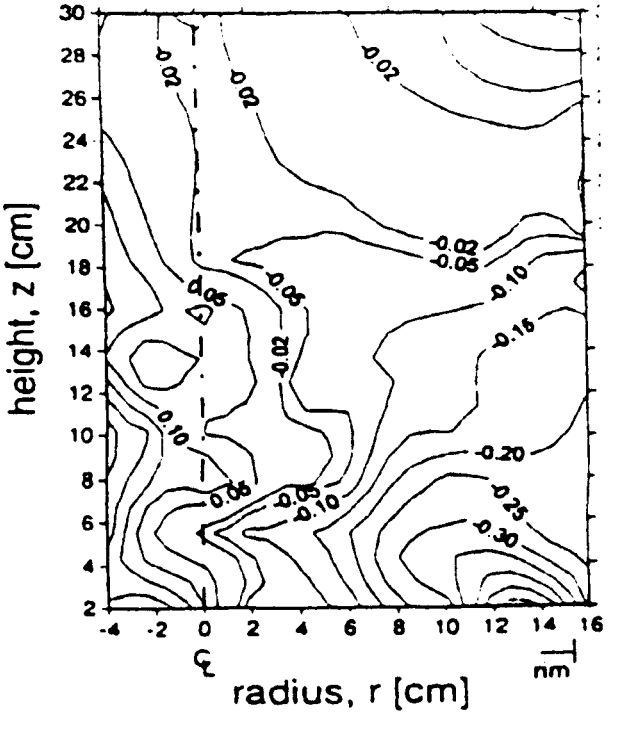

Fig. 3.8

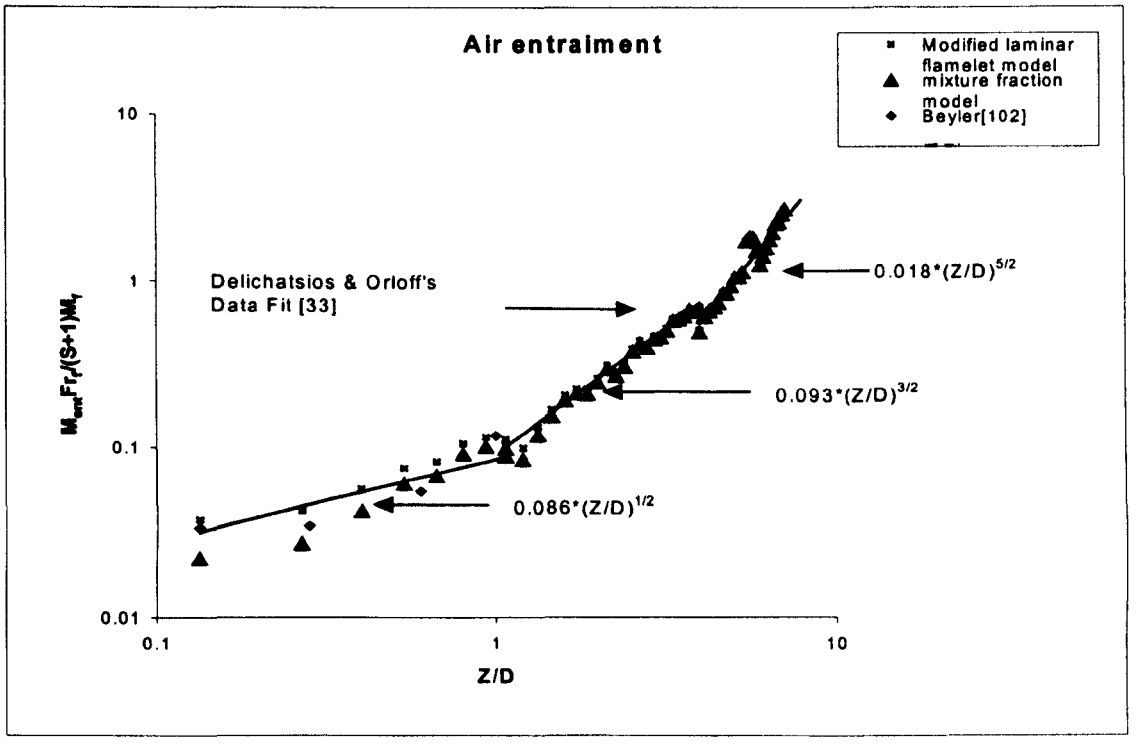

Fig. 3.9

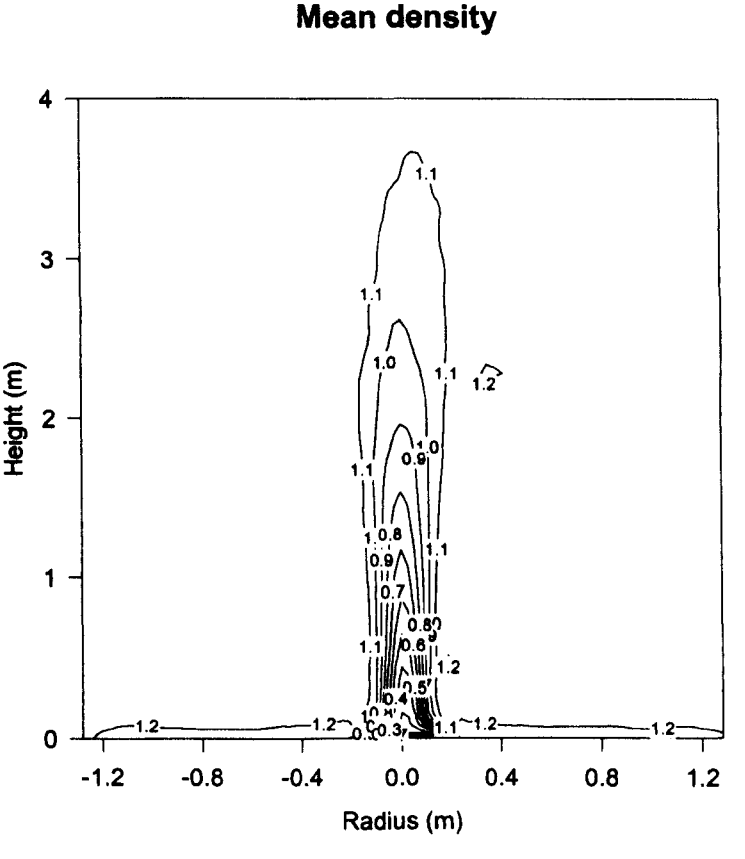

Fig. 3.10

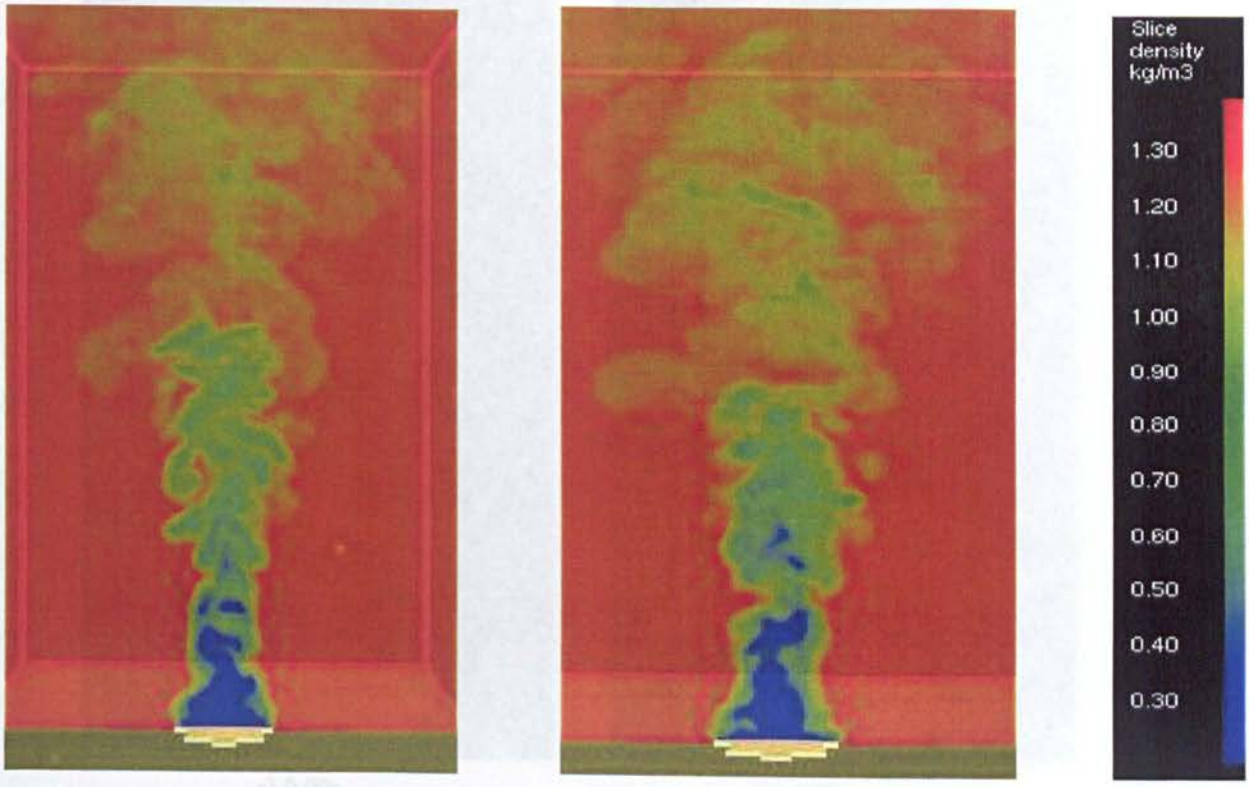

(a) Modified laminar flamelet model

(b) Mixture fraction model

Fig. 3.11

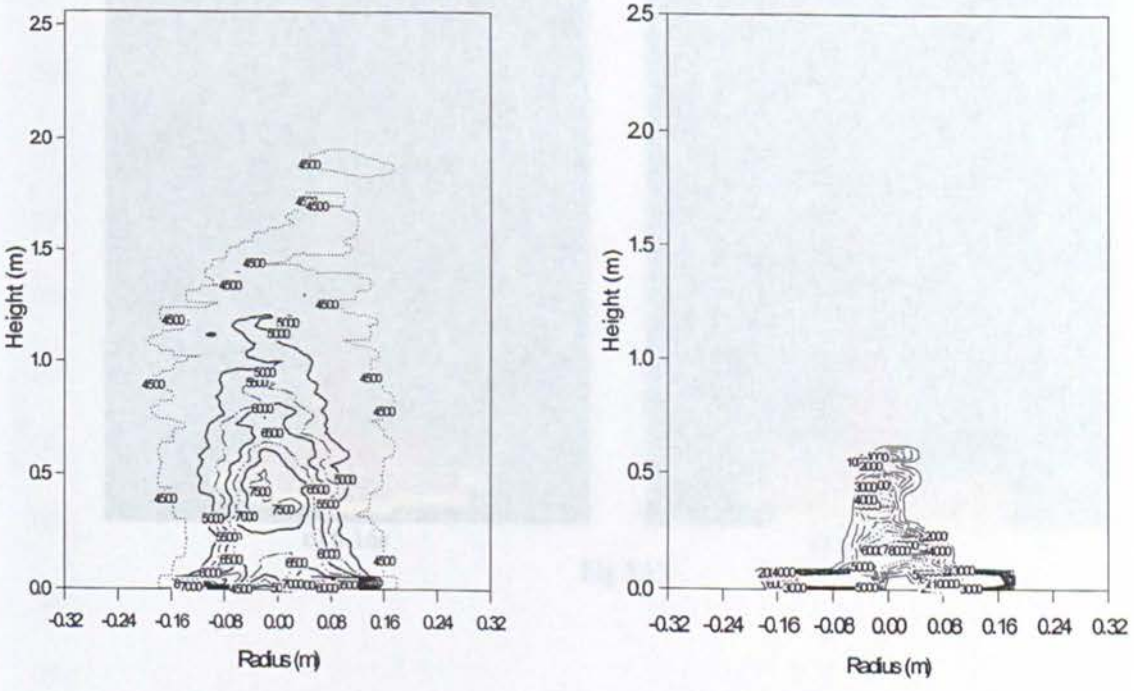

(a) Modified laminar flamelet model

(b) Mixture fraction model

Fig 3.12 (KW/m^3)

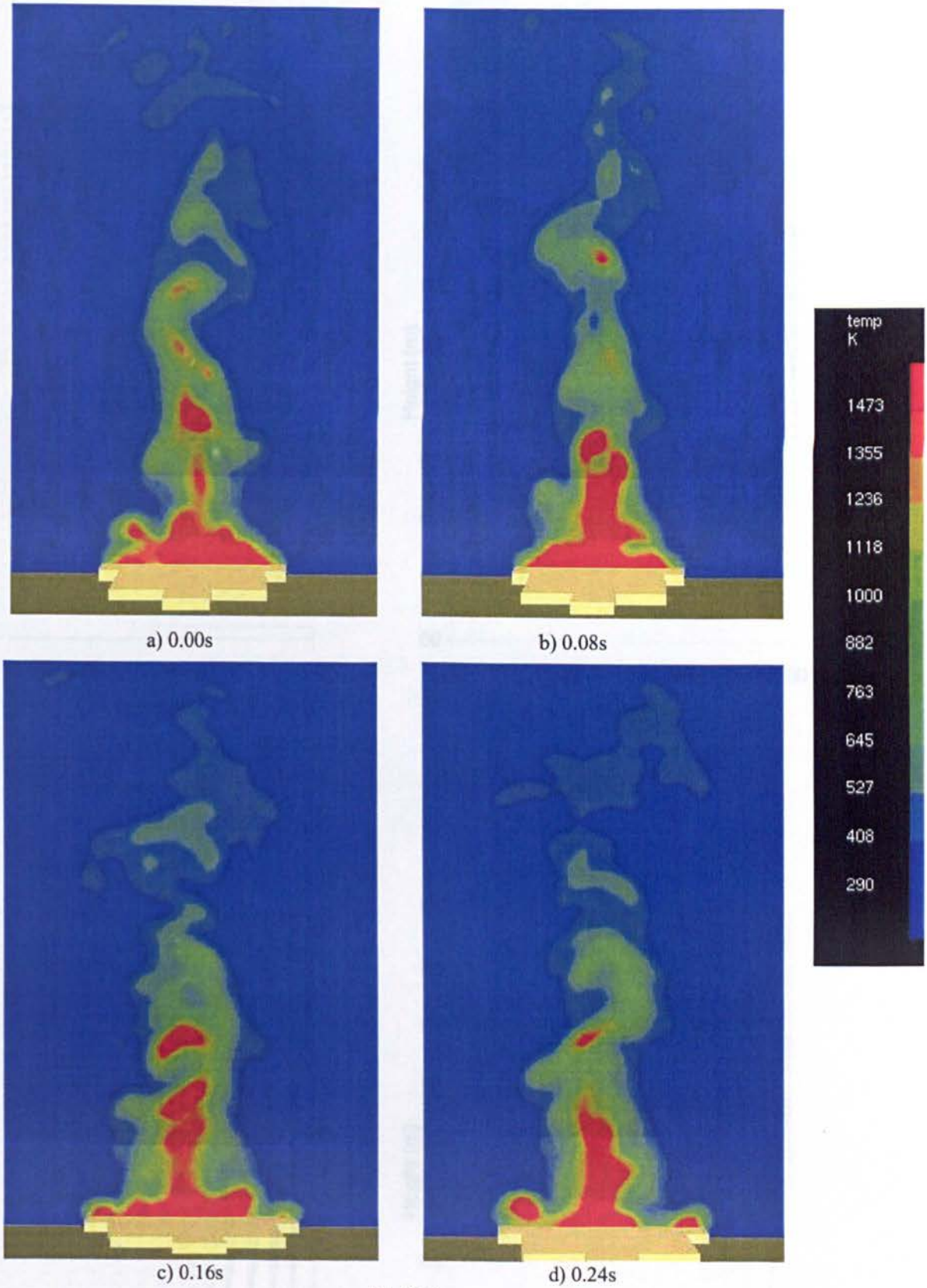

a) 0.00s

b) 0.08s

c) 0.16s

d) 0.24s

Fig 3.13

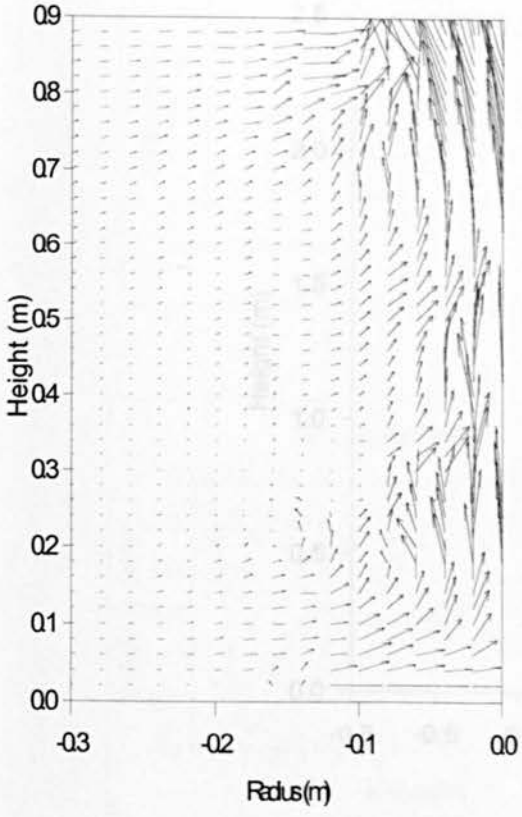

a) 0.00s

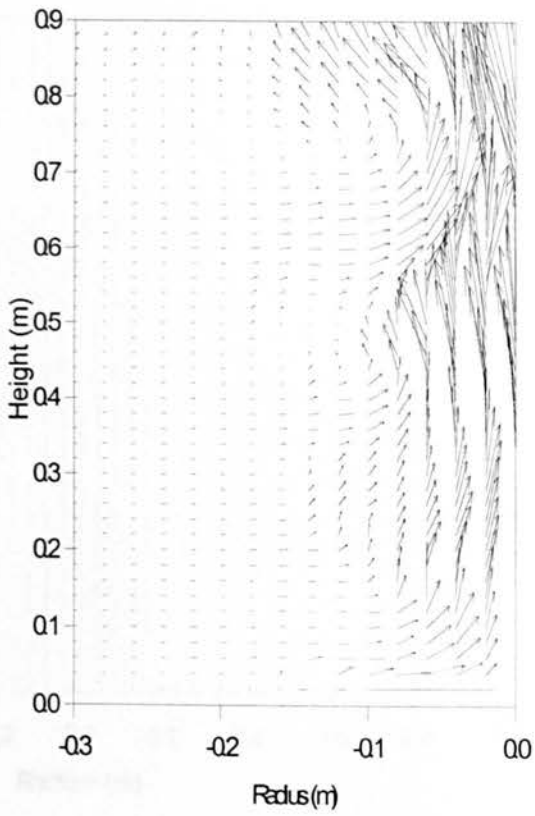

b) 0.08s

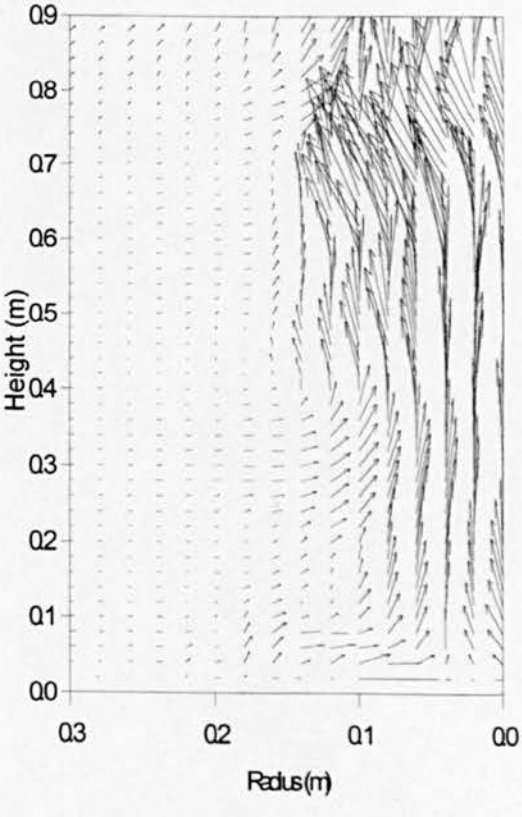

c) 0.16s

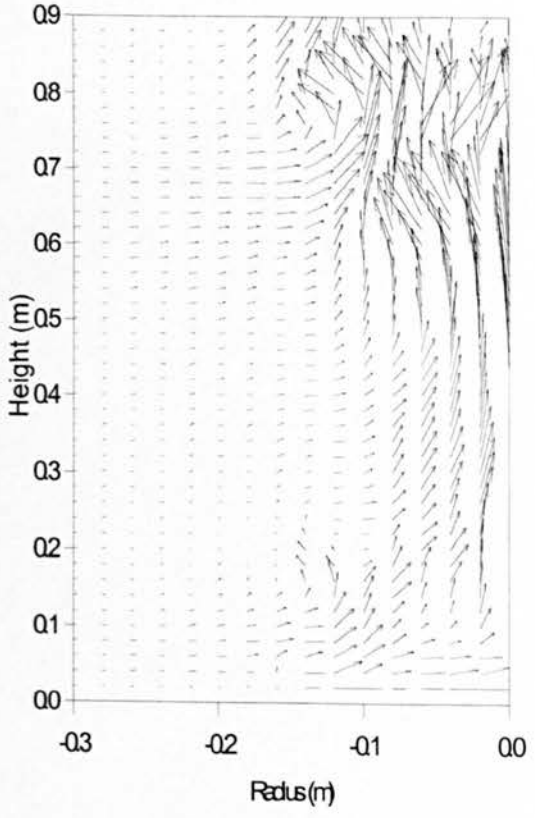

d) 0.24s

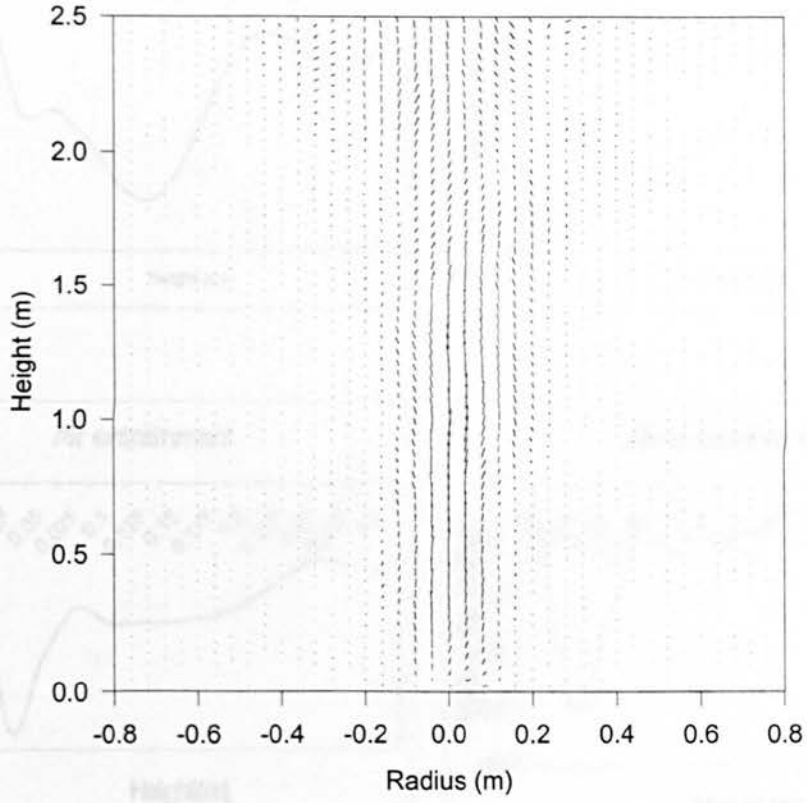

(e) average profile

Fig 3.14

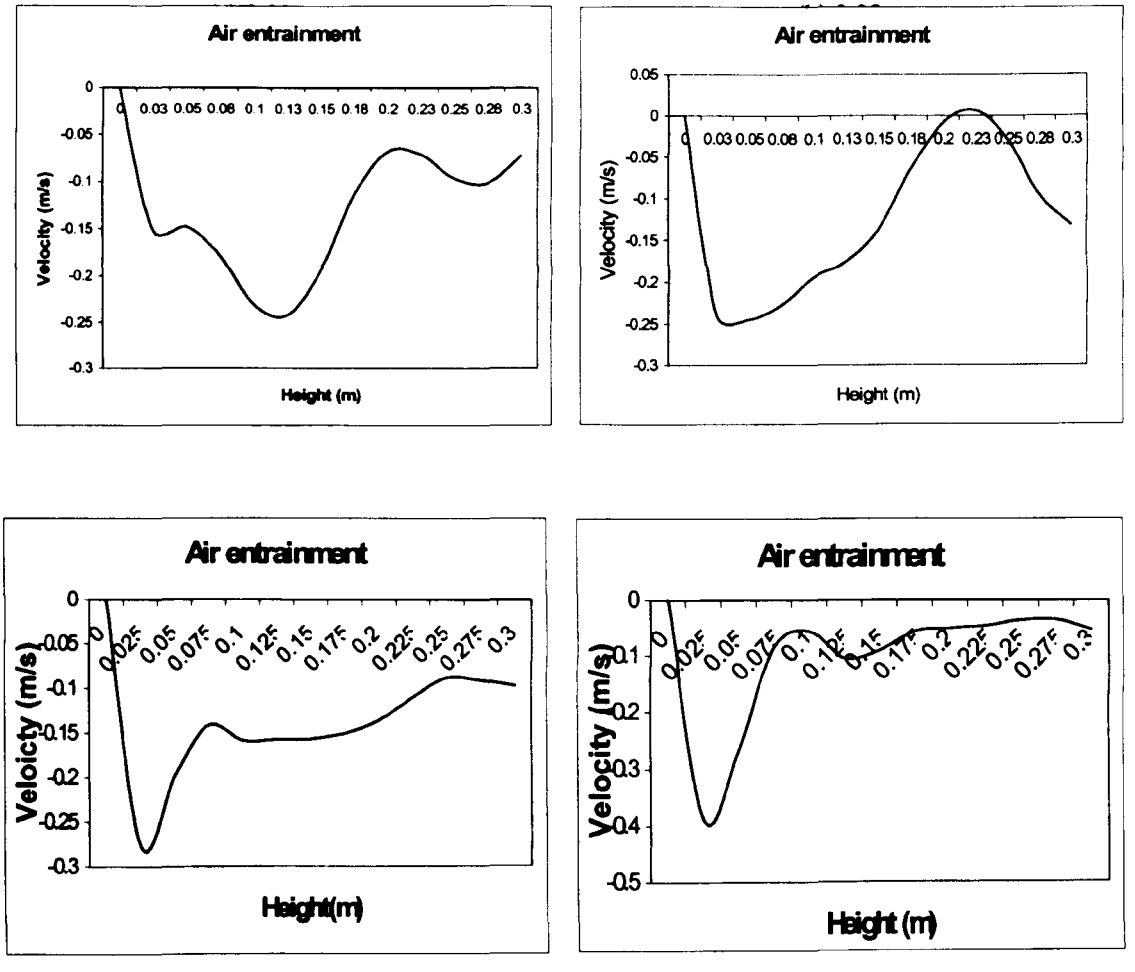
Air entrainment
Velocity (m/s)
Height (m)
0 0.03 0.05 0.08 0.1 0.13 0.15 0.18 0.2 0.23 0.25 0.28 0.3
Air entrainment
Velocity (m/s)
Height (m)
0 0.03 0.05 0.08 0.1 0.13 0.15 0.18 0.2 0.23 0.25 0.28 0.3
Air entrainment
Velocity (m/s)
Height(m)
0 0.02F 0.05 0.07F 0.1 0.12F 0.15 0.17F 0.2 0.22F 0.25 0.27F 0.3
Air entrainment
Velocity (m/s)
Height (m)
0 0.02F 0.05 0.07F 0.1 0.12F 0.15 0.17F 0.2 0.22F 0.25 0.27F

Fig 3.15

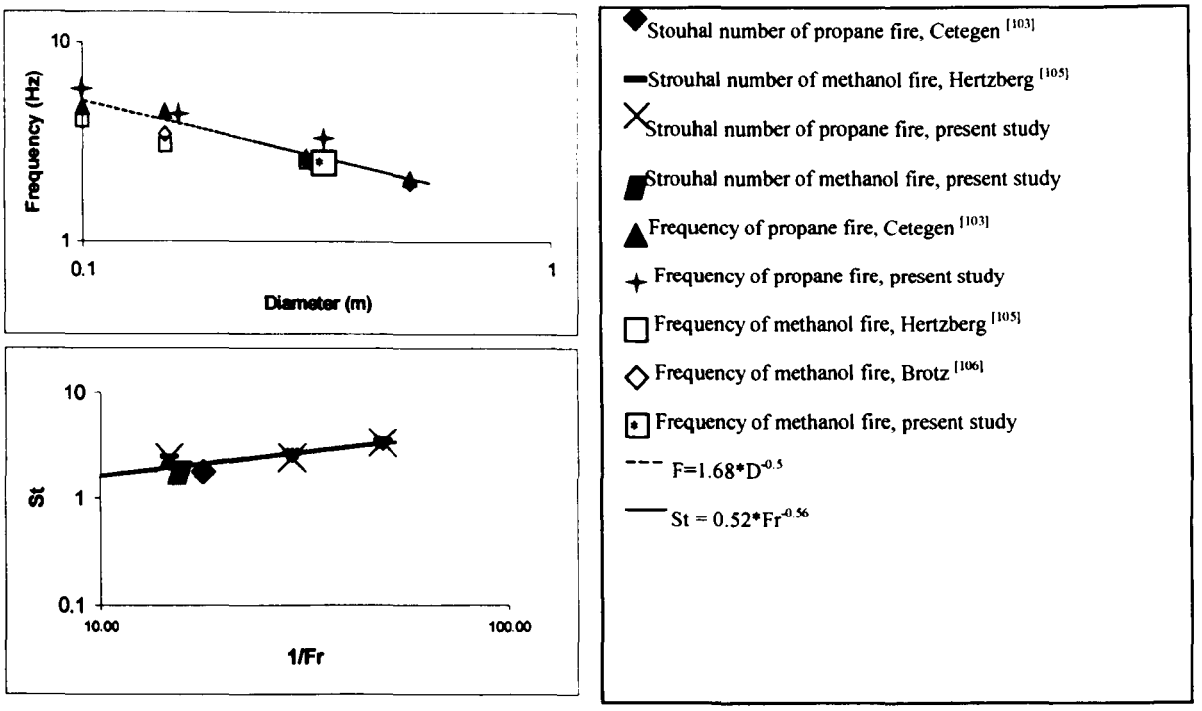

Fig. 3.16

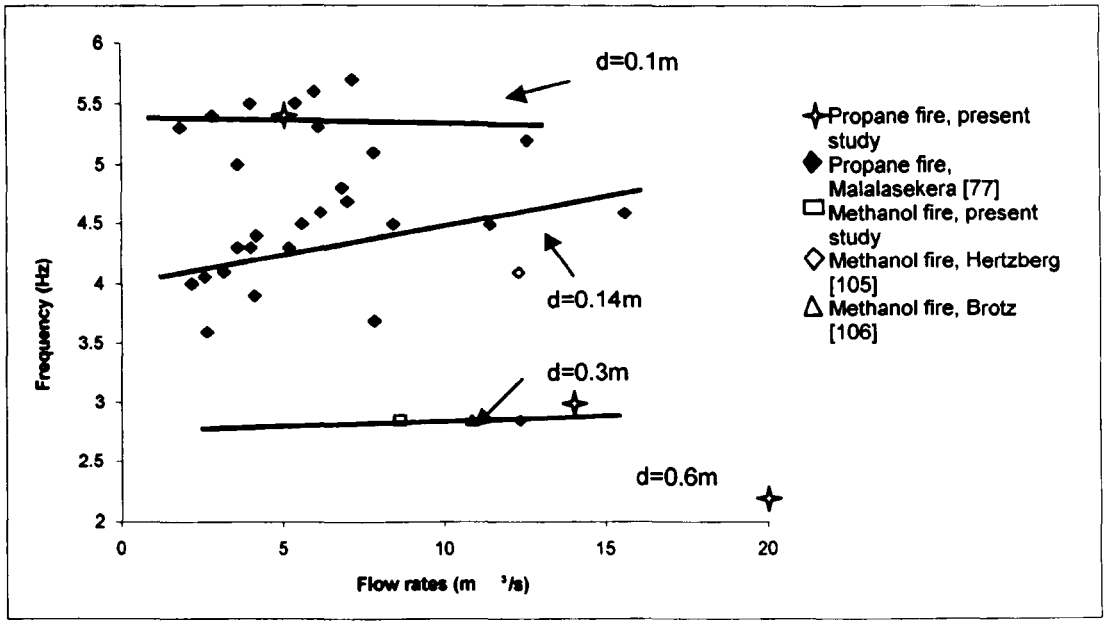

Fig. 3.17

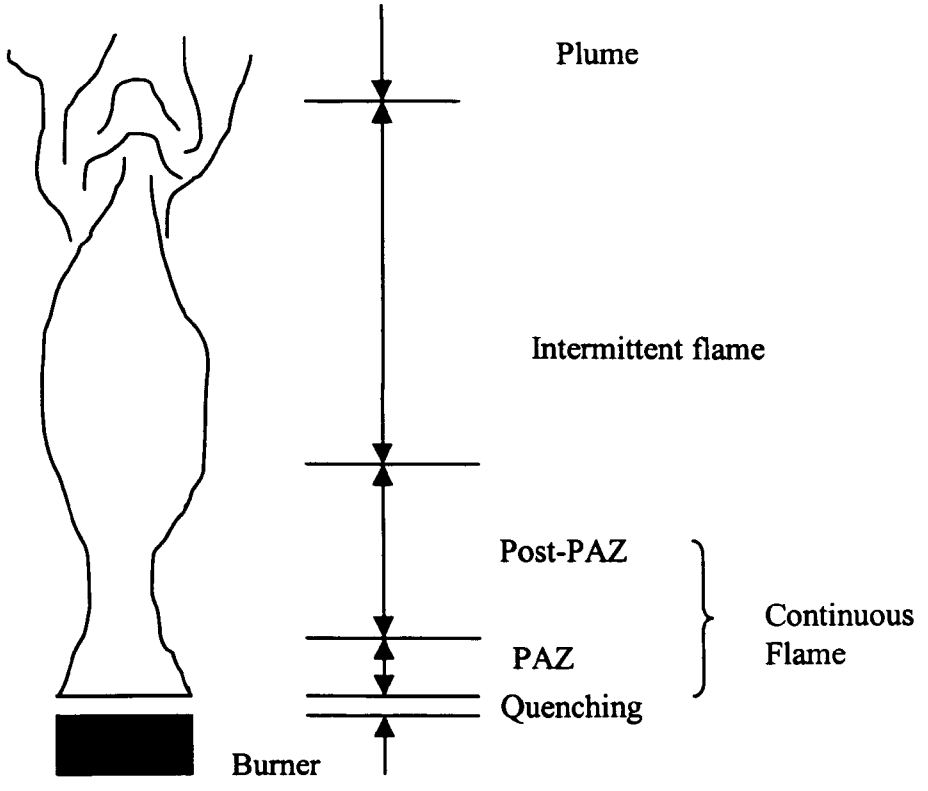
Plume
Intermittent flame
Post-PAZ
PAZ
Quenching
Continuous
Flame
Burner

Fig 4.1

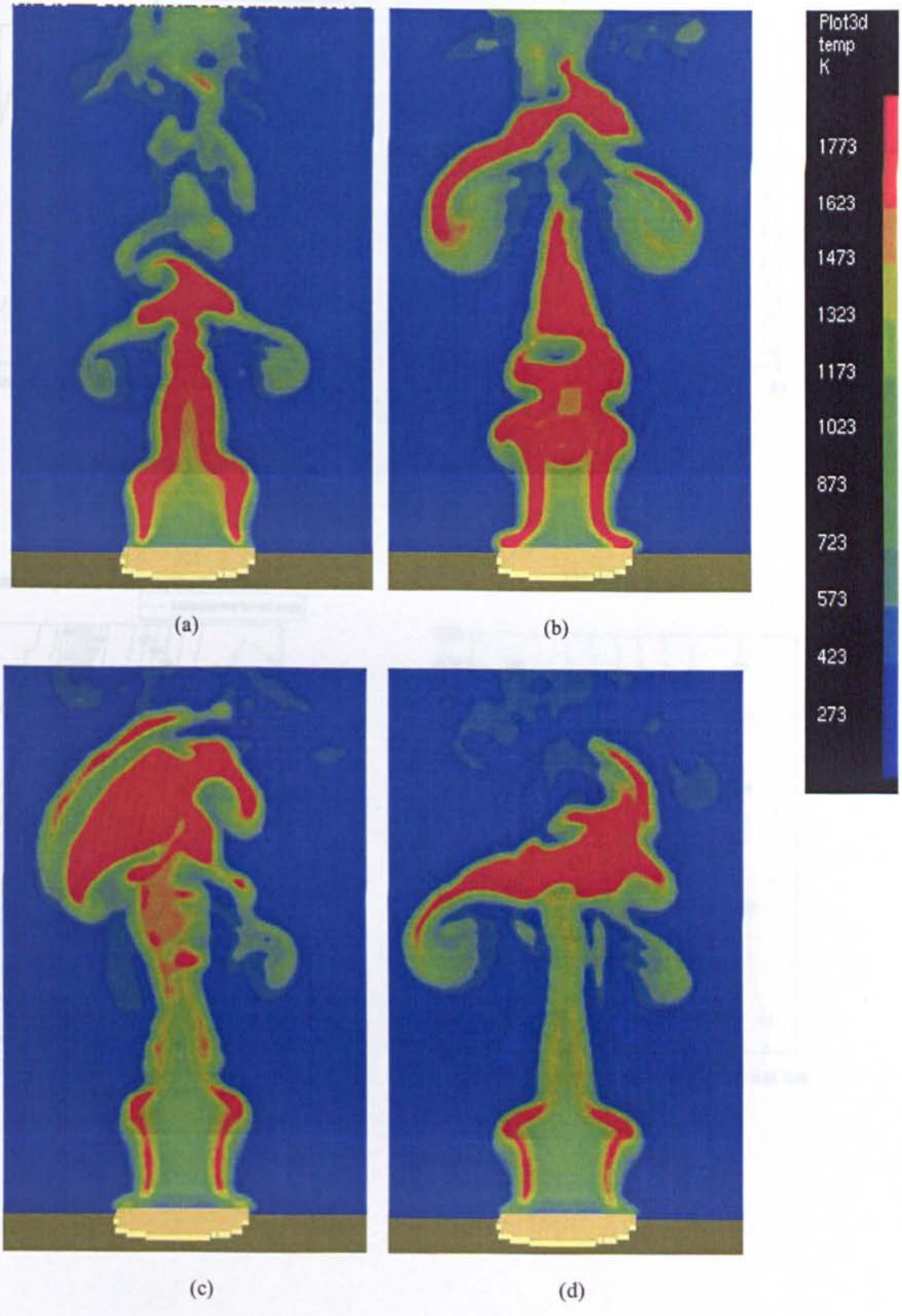
Plot3d
temp
K
1773
1623
1473
1323
1173
1023
873
723
573
423
273
(a)
(b)
(c)
(d)

Fig 4.2

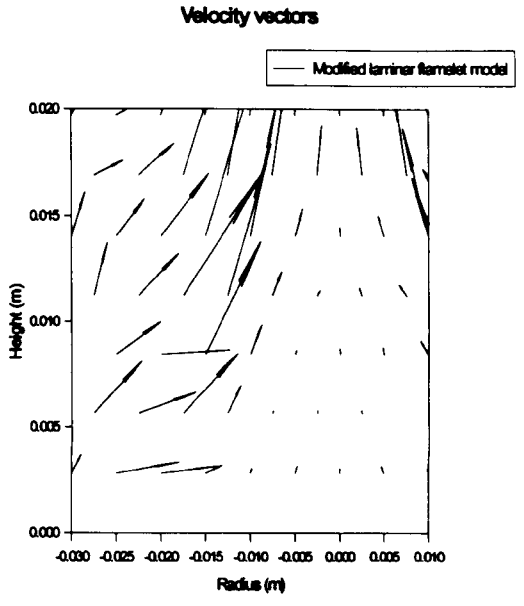

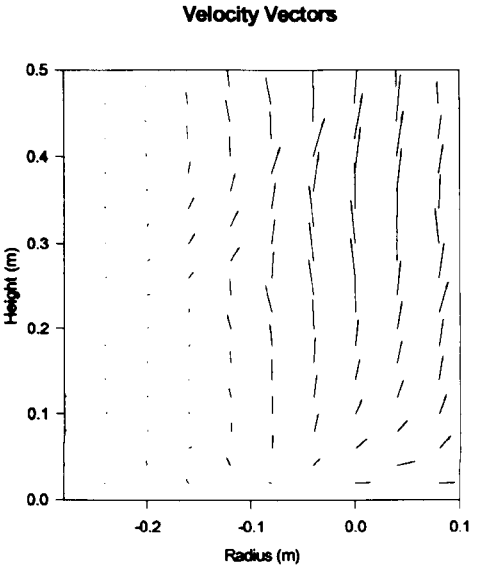

a) b)

Fig 4.3

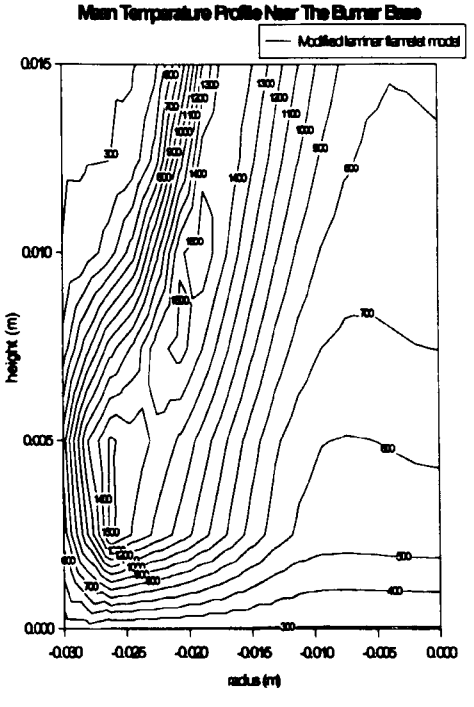

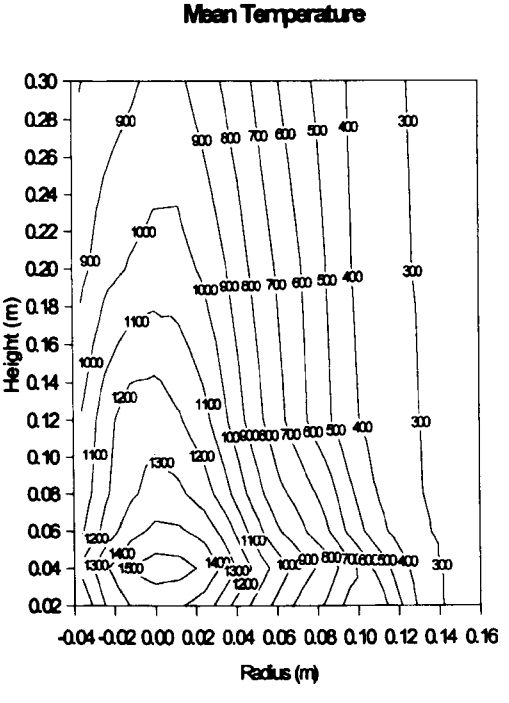

a) b)

Fig 4.4

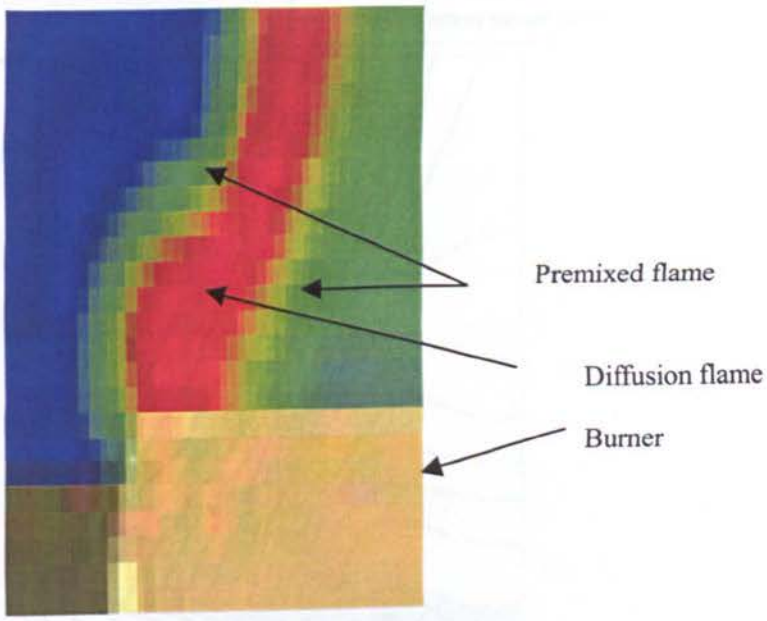

Fig. 4.5

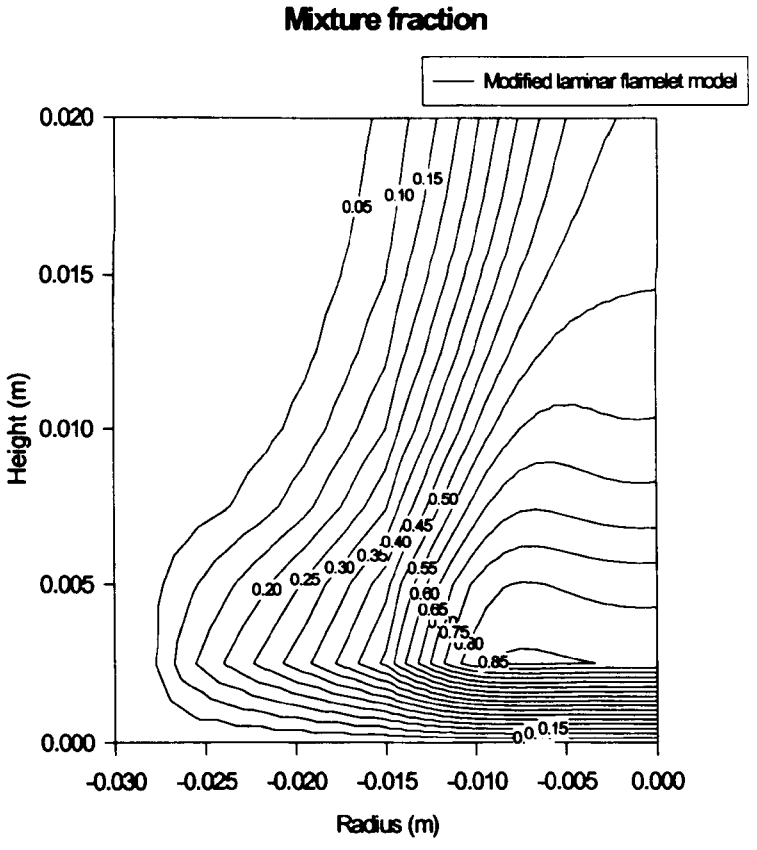
Mixture fraction
Modified laminar flamelet model
0.020
0.015
0.010
0.005
0.000
Height (m)
0.05
0.10
0.15
0.20
0.25
0.30
0.35
0.40
0.45
0.50
0.55
0.60
0.65
0.75
0.80
0.85
0.0.15
-0.030
-0.025
-0.020
-0.015
-0.010
-0.005
0.000
Radius (m)

Fig 4.6

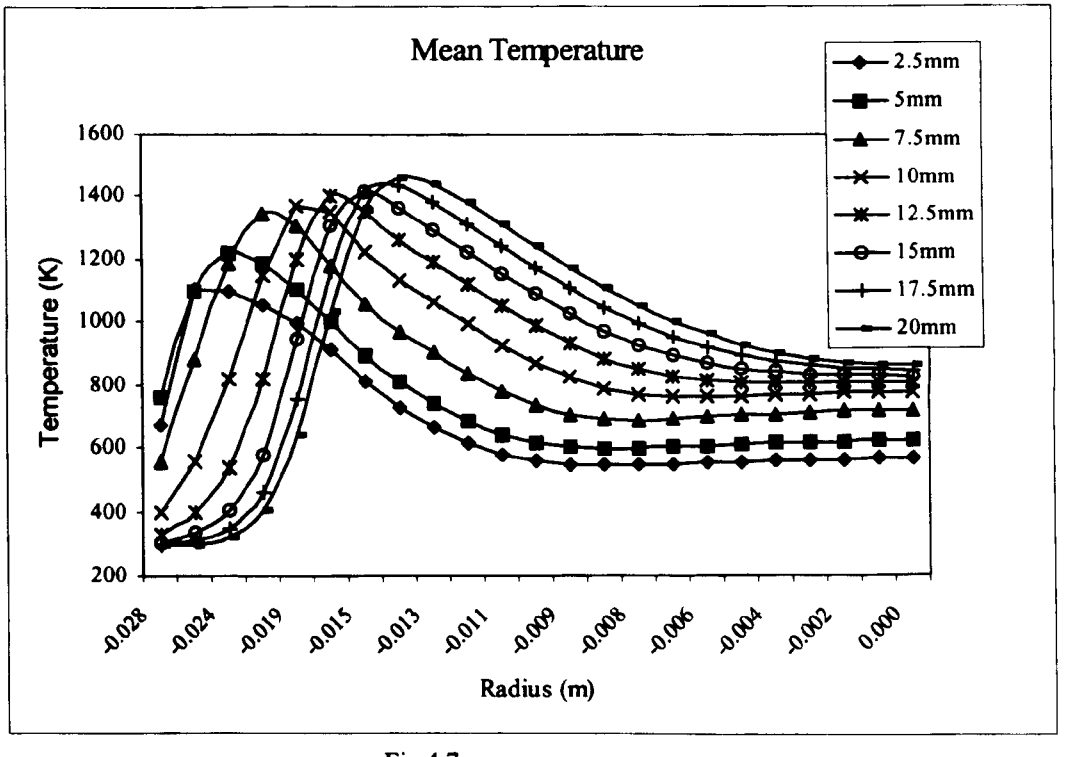
Mean Temperature
2.5mm
5mm
7.5mm
10mm
12.5mm
15mm
17.5mm
20mm
1600
1400
1200
1000
800
600
400
200
Temperature (K)
-0.028
-0.024
-0.019
-0.015
-0.013
-0.011
-0.009
-0.008
-0.006
-0.004
-0.002
0.000
Radius (m)

Fig 4.7

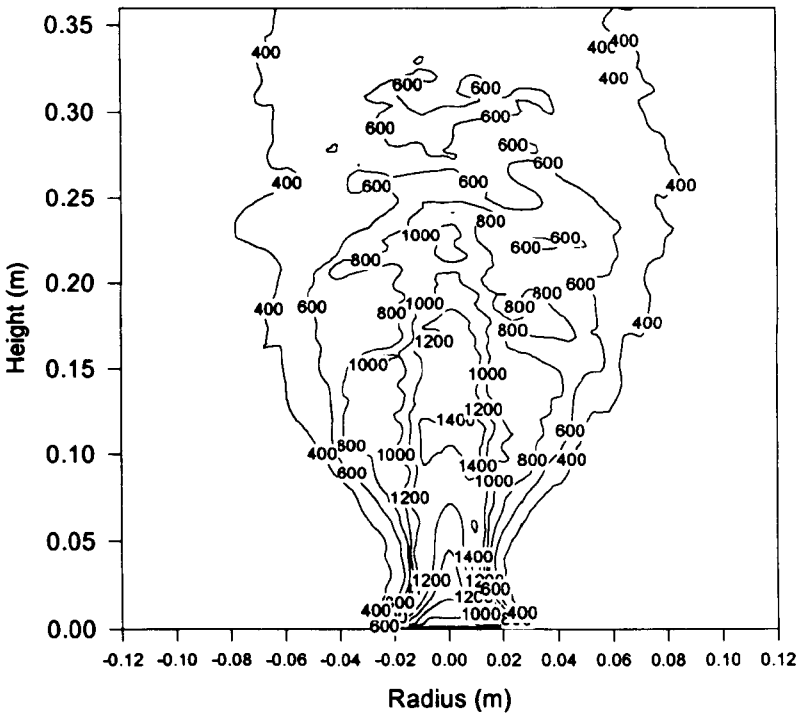

Fig 4.8

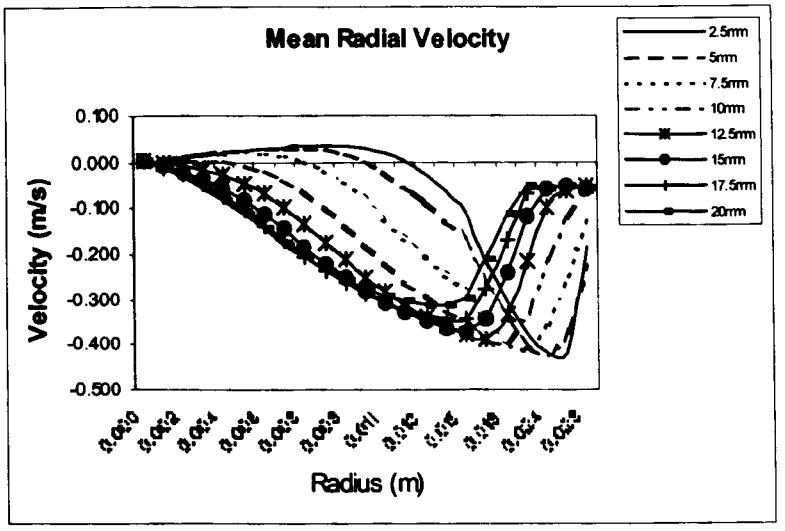

Fig 4.9

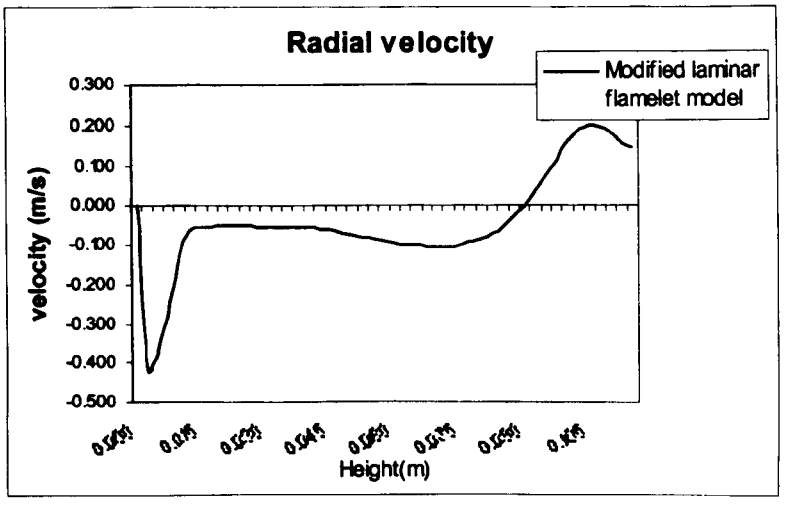

Fig 4.10

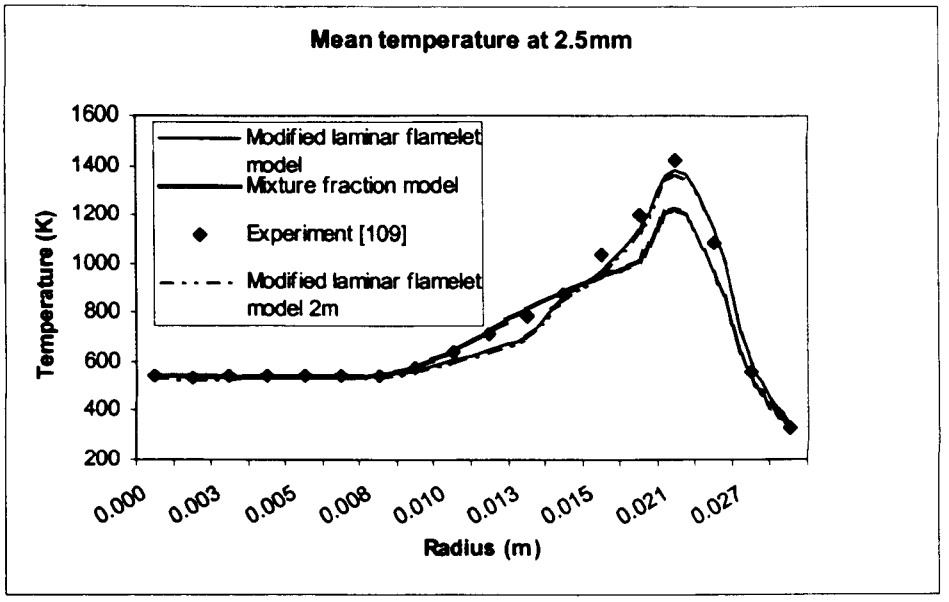
Mean temperature at 2.5mm
Modified laminar flamelet model
Mixture fraction model
Experiment [109]
Modified laminar flamelet model 2m
Temperature (K)
1600
1400
1200
1000
800
600
400
200
0.000
0.003
0.005
0.008
0.010
0.013
0.015
0.021
0.027
Radius (m)

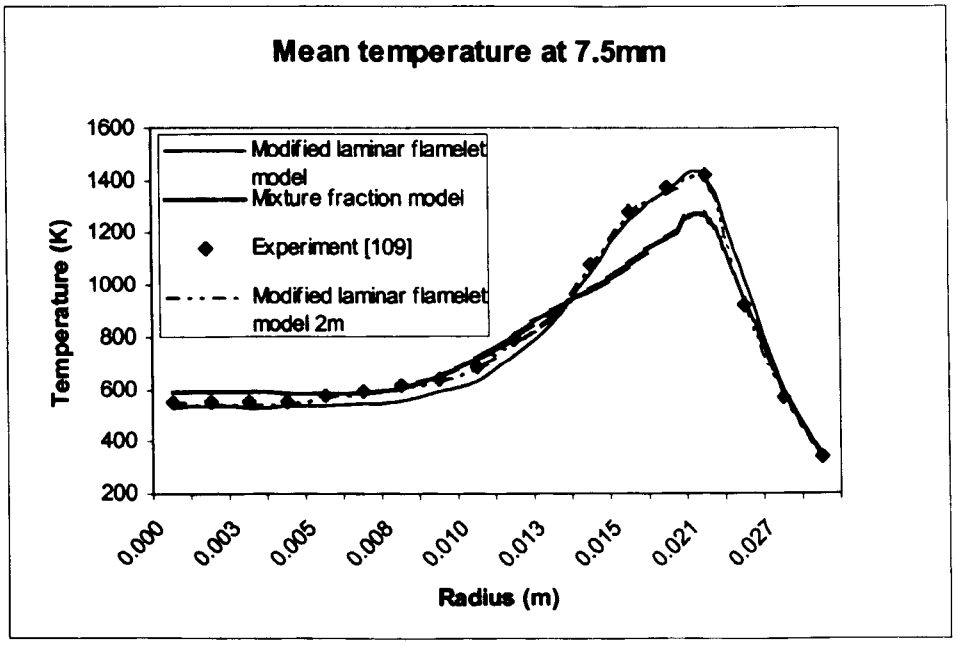
Mean temperature at 7.5mm
Modified laminar flamelet model
Mixture fraction model
Experiment [109]
Modified laminar flamelet model 2m
Temperature (K)
1600
1400
1200
1000
800
600
400
200
0.000
0.003
0.005
0.008
0.010
0.013
0.015
0.021
0.027
Radius (m)

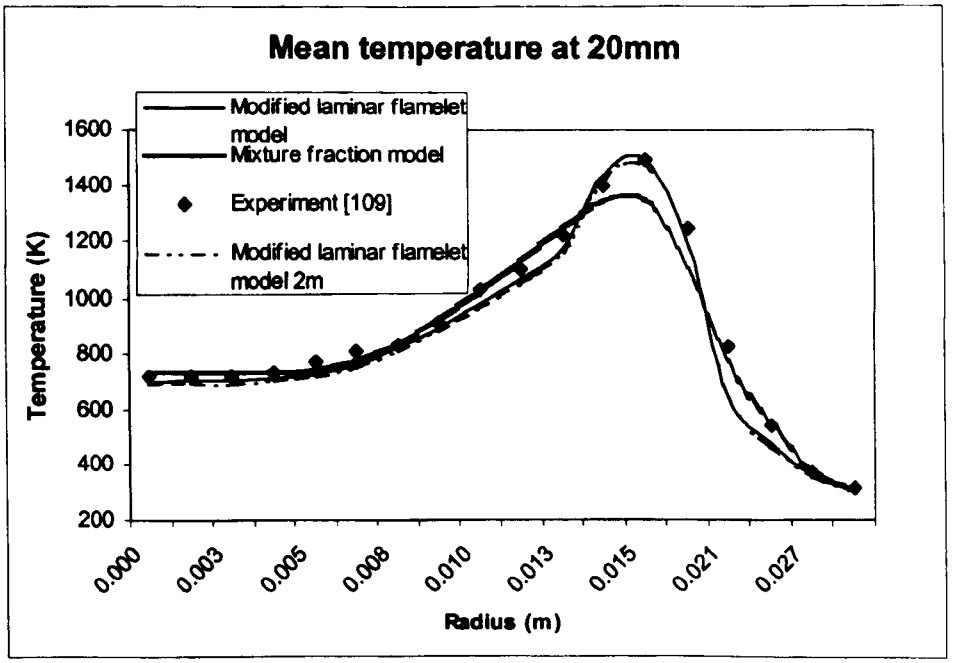
Mean temperature at 20mm
Modified laminar flamelet model
Mixture fraction model
Experiment [109]
Modified laminar flamelet model 2m
Temperature (K)
1600
1400
1200
1000
800
600
400
200
0.000
0.003
0.005
0.008
0.010
0.013
0.015
0.021
0.027
Radius (m)

Fig 4.11

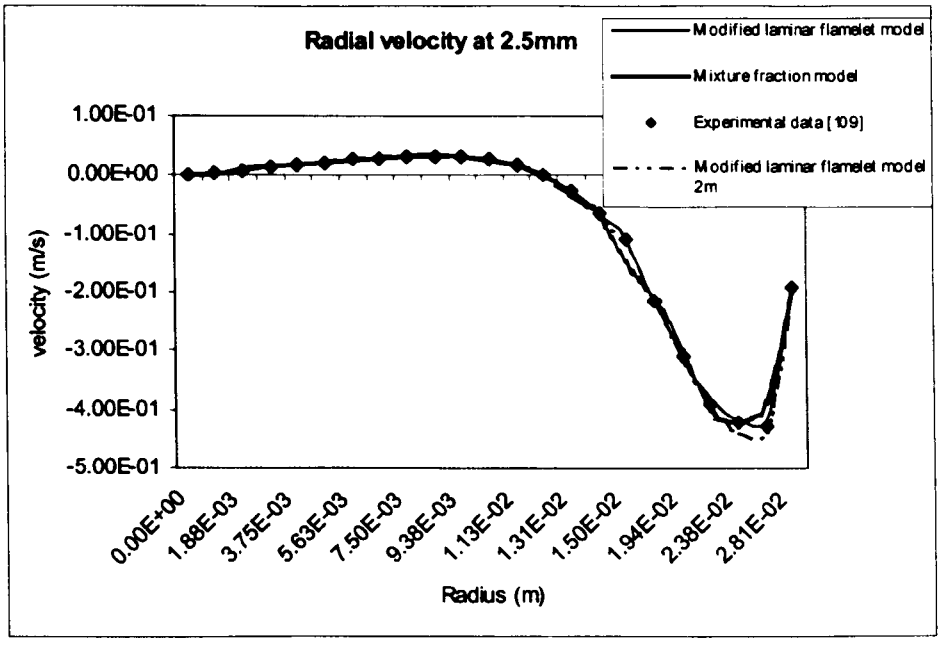
Radial velocity at 2.5mm
Modified laminar flamelet model
Mixture fraction model
Experimental data [109]
Modified laminar flamelet model 2m
1.00E-01
0.00E+00
-1.00E-01
-2.00E-01
-3.00E-01
-4.00E-01
-5.00E-01
velocity (m/s)
0.00E+00
1.88E-03
3.75E-03
5.63E-03
7.50E-03
9.38E-03
1.13E-02
1.31E-02
1.50E-02
1.94E-02
2.38E-02
2.81E-02
Radius (m)

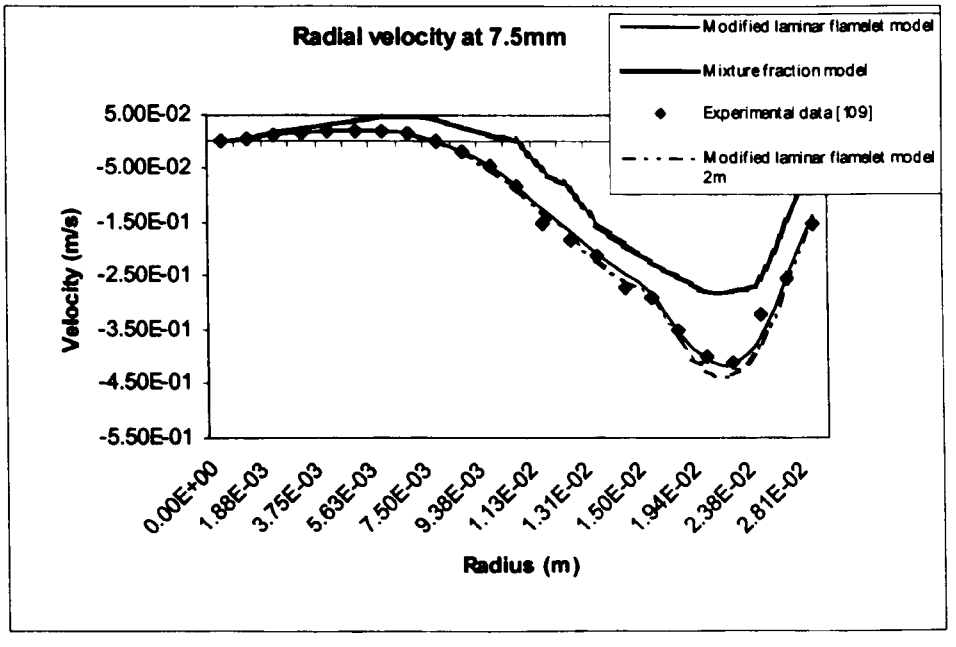
Radial velocity at 7.5mm
Modified laminar flamelet model
Mixture fraction model
Experimental data [109]
Modified laminar flamelet model 2m
5.00E-02
-5.00E-02
-1.50E-01
-2.50E-01
-3.50E-01
-4.50E-01
-5.50E-01
Velocity (m/s)
0.00E+00
1.88E-03
3.75E-03
5.63E-03
7.50E-03
9.38E-03
1.13E-02
1.31E-02
1.50E-02
1.94E-02
2.38E-02
2.81E-02
Radius (m)

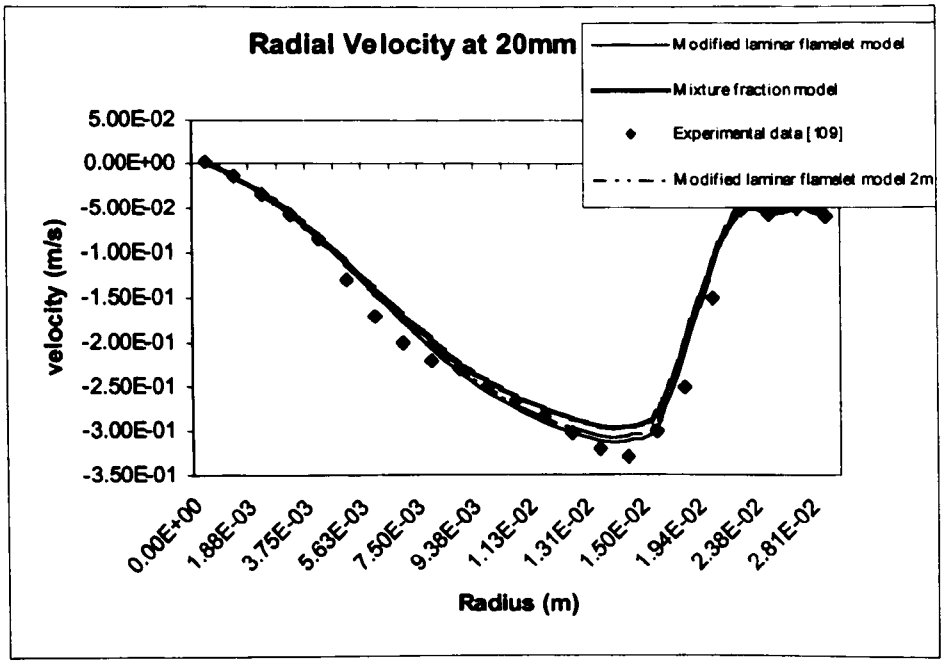
Radial Velocity at 20mm
Modified laminar flamelet model
Mixture fraction model
Experimental data [109]
Modified laminar flamelet model 2m
5.00E-02
0.00E+00
-5.00E-02
-1.00E-01
-1.50E-01
-2.00E-01
-2.50E-01
-3.00E-01
-3.50E-01
velocity (m/s)
0.00E+00
1.88E-03
3.75E-03
5.63E-03
7.50E-03
9.38E-03
1.13E-02
1.31E-02
1.50E-02
1.94E-02
2.38E-02
2.81E-02
Radius (m)

Fig 4.12

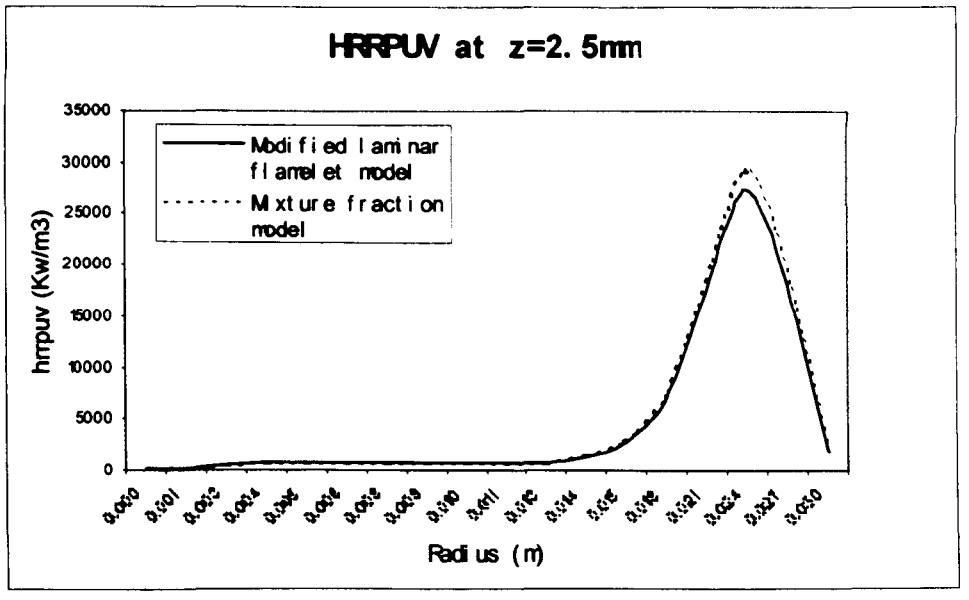
HRRPUV at z=2. 5mm
Modified laminar flamelet model
Mixture fraction model
hrrpuv (Kw/m3)
Radius (m)

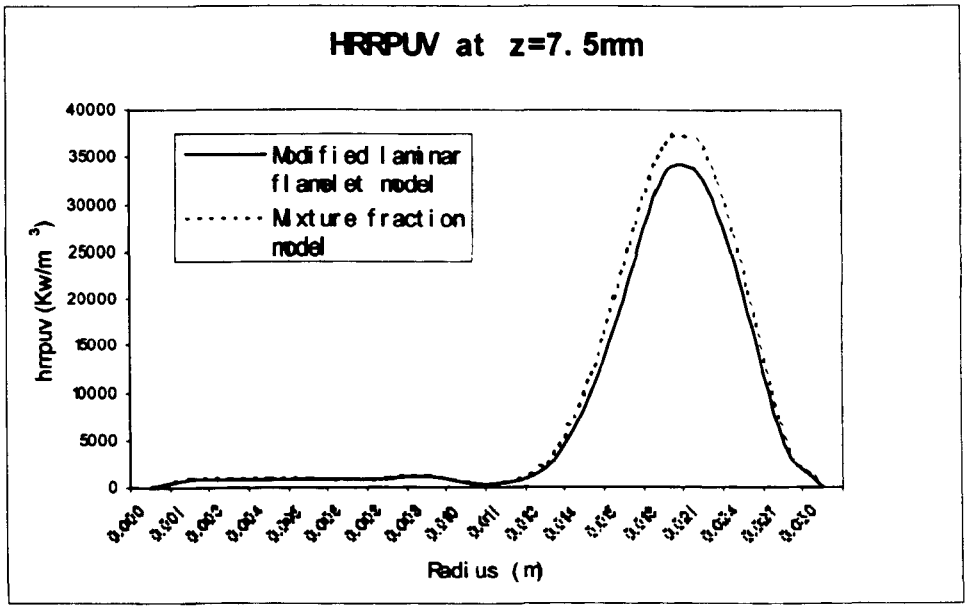
HRRPUV at z=7. 5mm
Modified laminar flamelet model
Mixture fraction model
hrrpuv (Kw/m 3)
Radius (m)

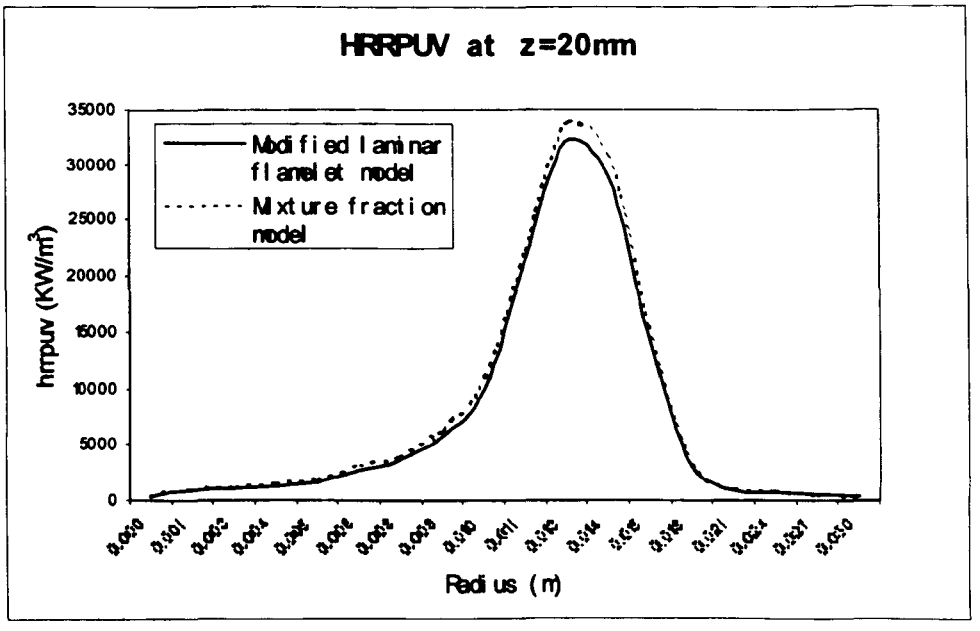
HRRPUV at z=20mm
Modified laminar flamelet model
Mixture fraction model
hrrpuv (KW/m3)
Radius (m)

Fig 4.13

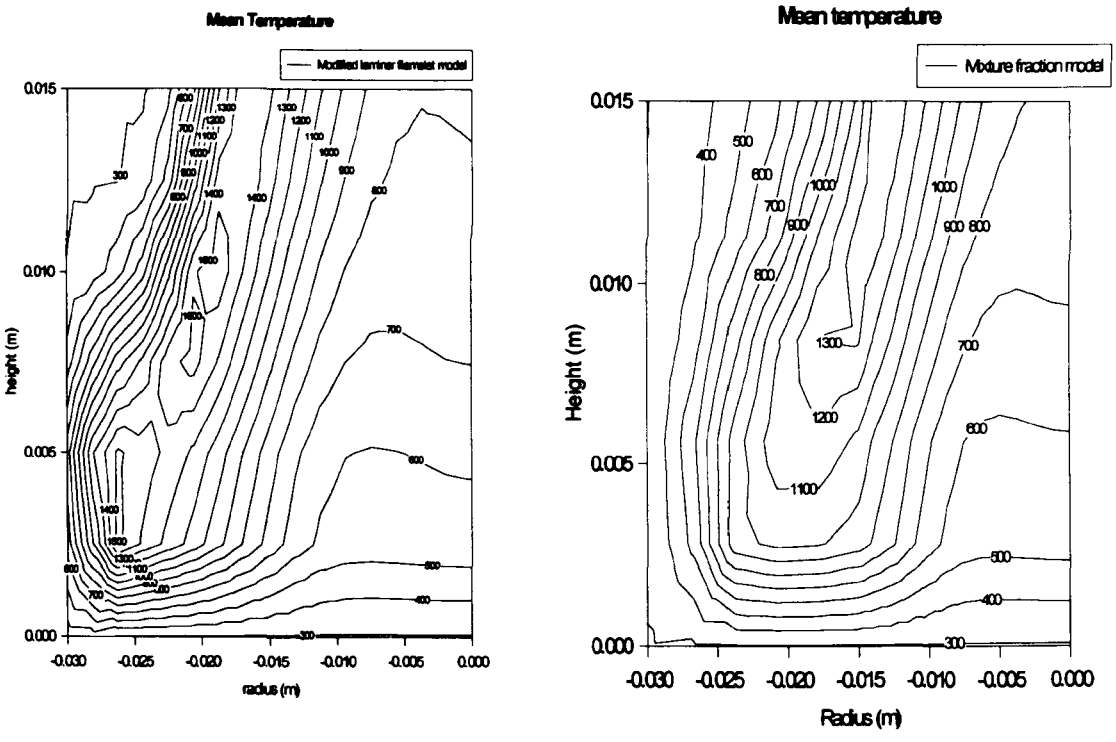

Fig 4.14

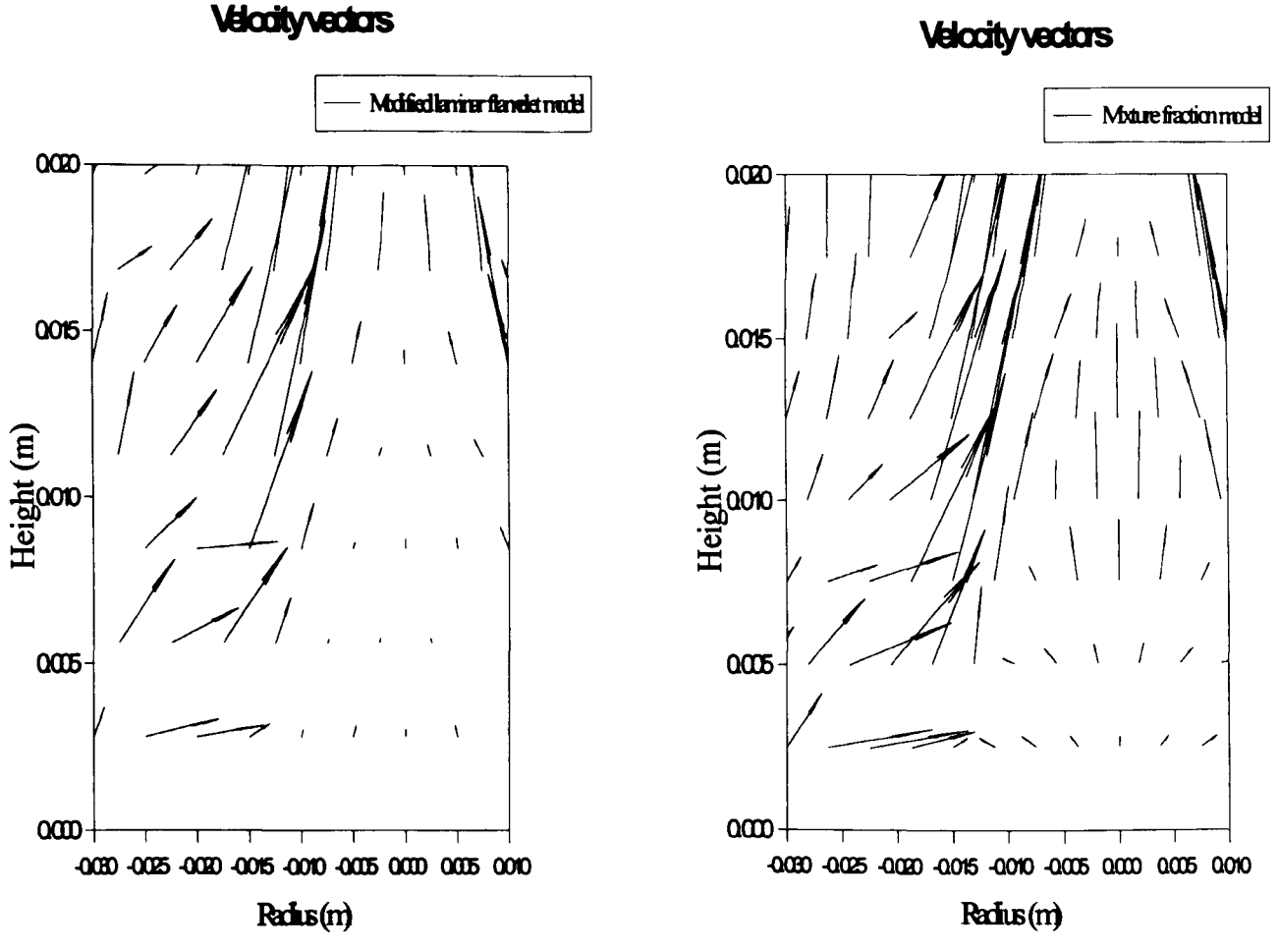

Fig. 4.15

First order of thermodynamic pressure

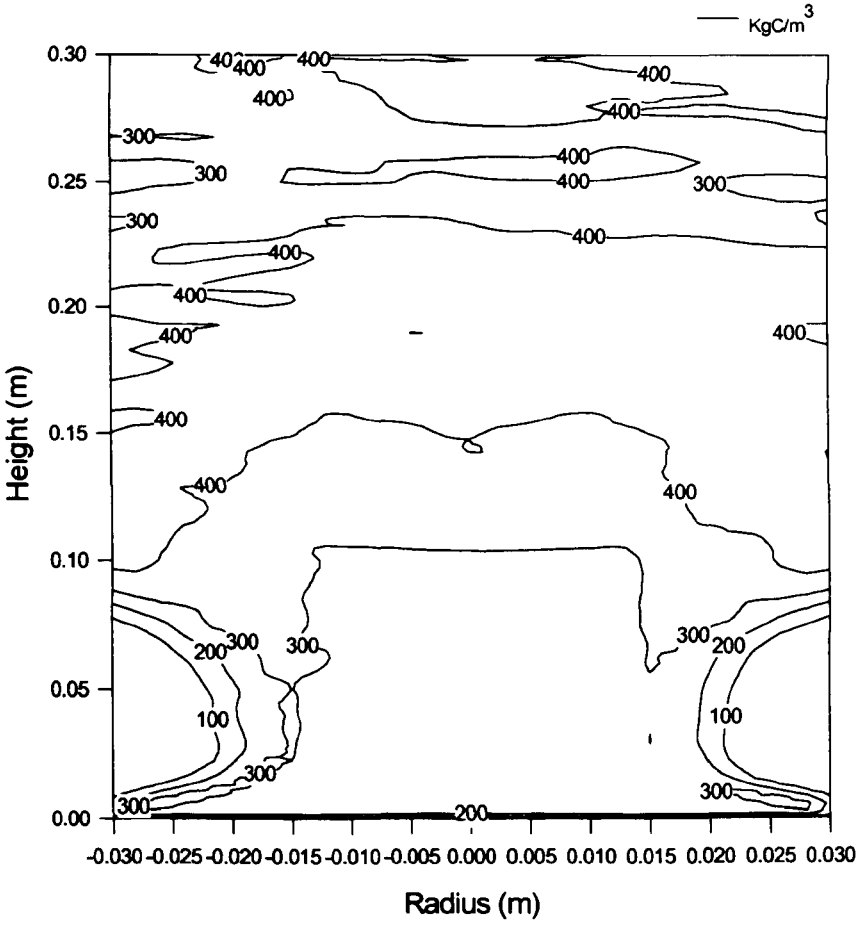

Fig 4.16

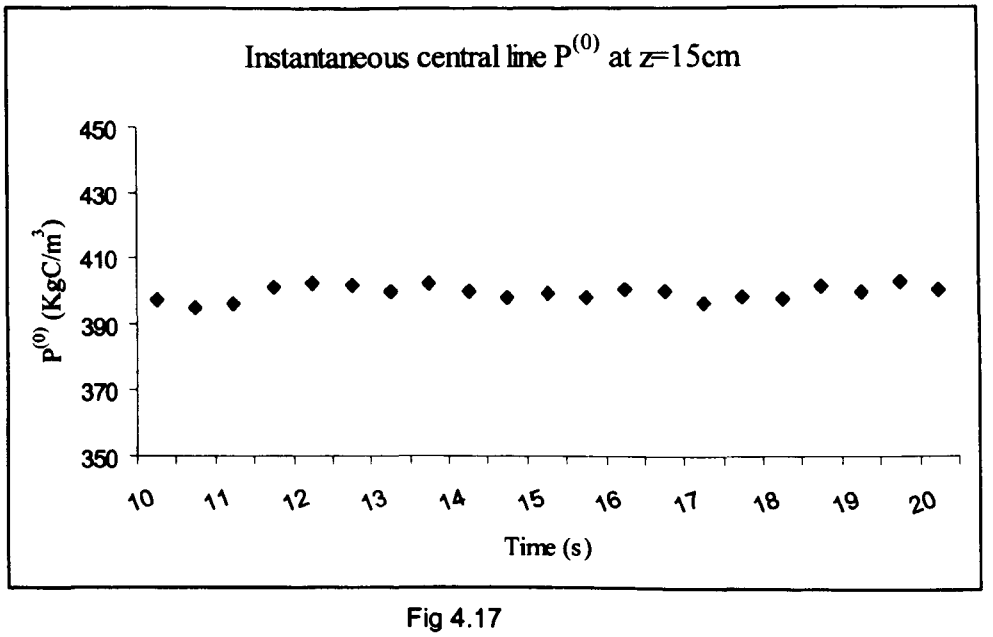

Fig 4.17

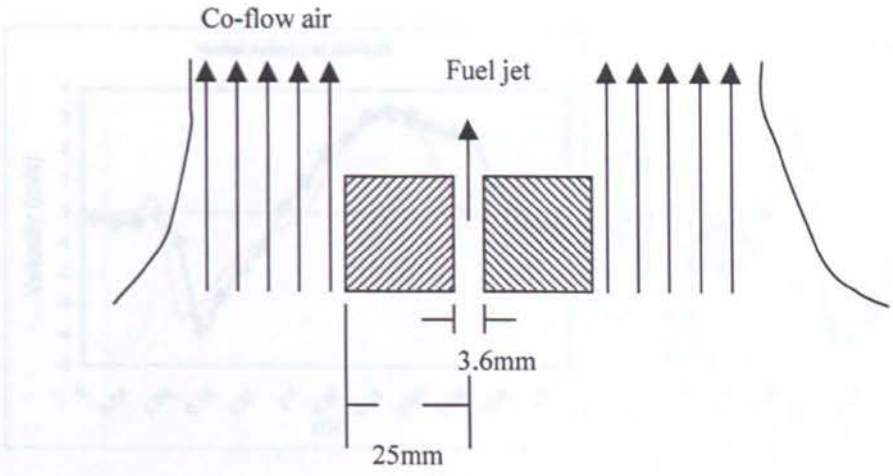
Co-flow air
Fuel jet
3.6mm
25mm

Fig. 5.1

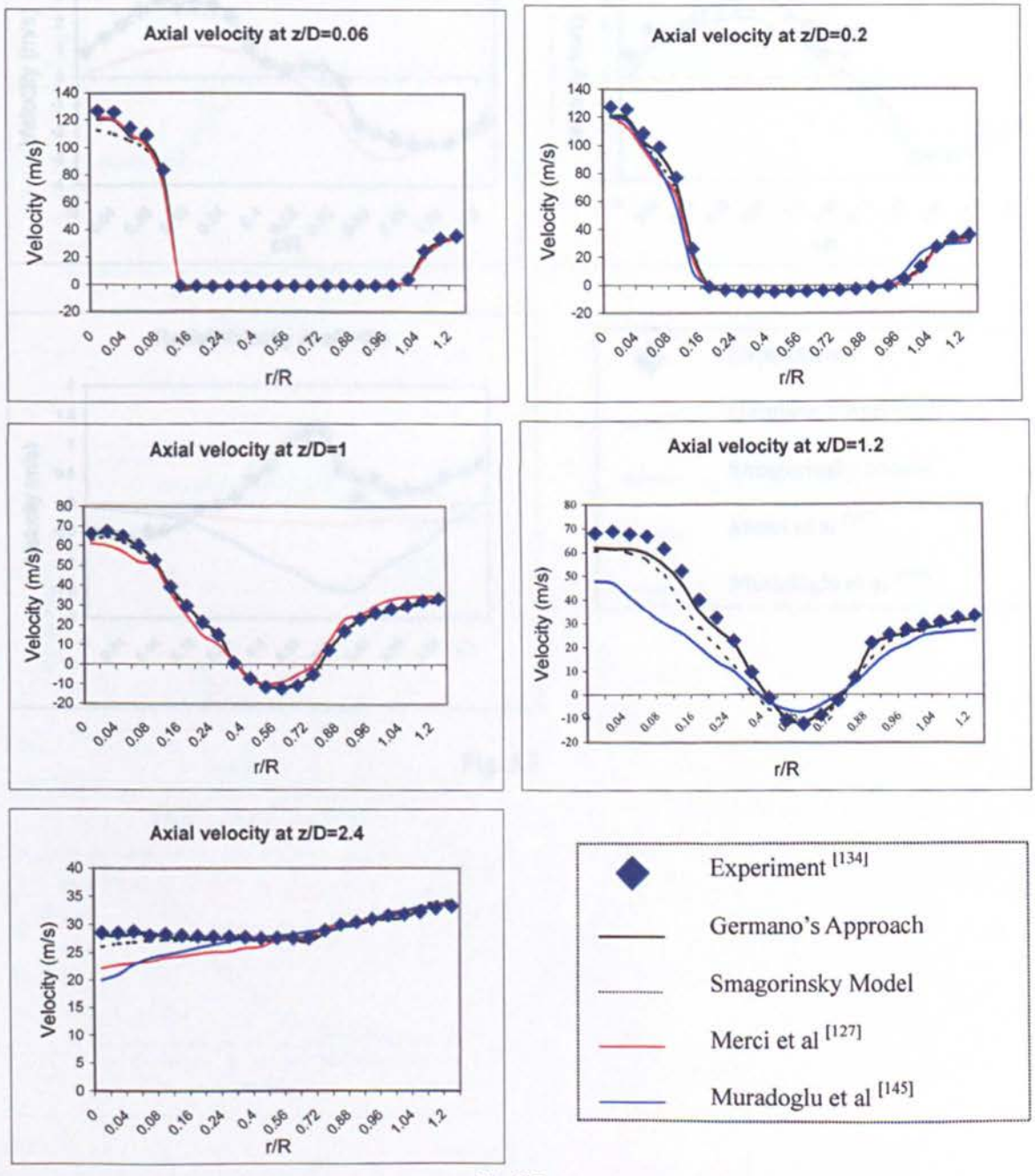
Axial velocity at z/D=0.06
Axial velocity at z/D=0.2
Axial velocity at z/D=1
Axial velocity at x/D=1.2
Axial velocity at z/D=2.4
Velocity (m/s)
r/R
Experiment [134]
Germano's Approach
Smagorinsky Model
Merci et al [127]
Muradoglu et al [145]

Fig.5.2

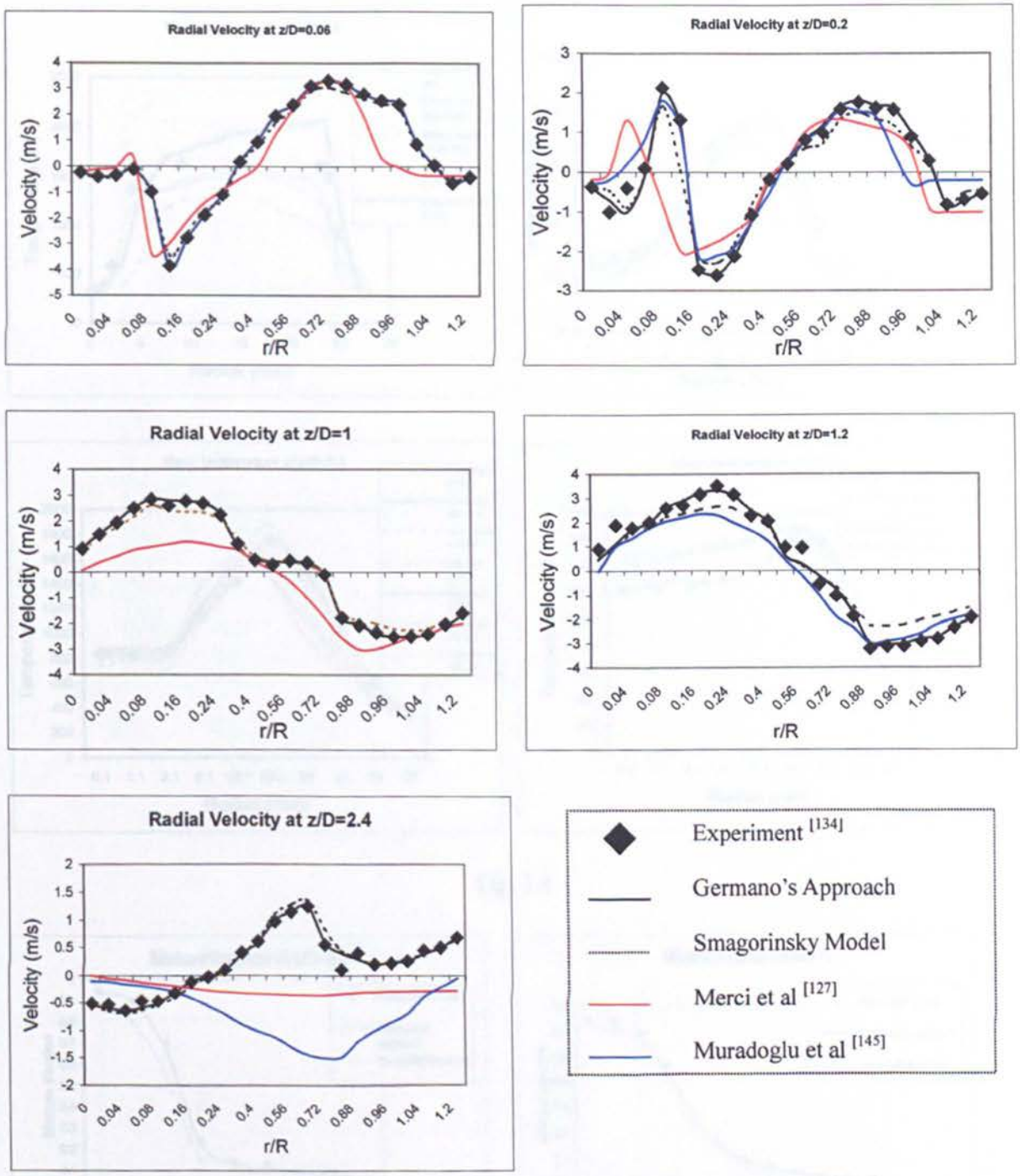
Radial Velocity at z/D=0.06
Radial Velocity at z/D=0.2
Radial Velocity at z/D=1
Radial Velocity at z/D=1.2
Radial Velocity at z/D=2.4
Velocity (m/s)
r/R
0
0.04
0.08
0.16
0.24
0.4
0.56
0.72
0.88
0.96
1.04
1.2
Experiment [134]
Germano's Approach
Smagorinsky Model
Merci et al [127]
Muradoglu et al [145]

Fig. 5.3

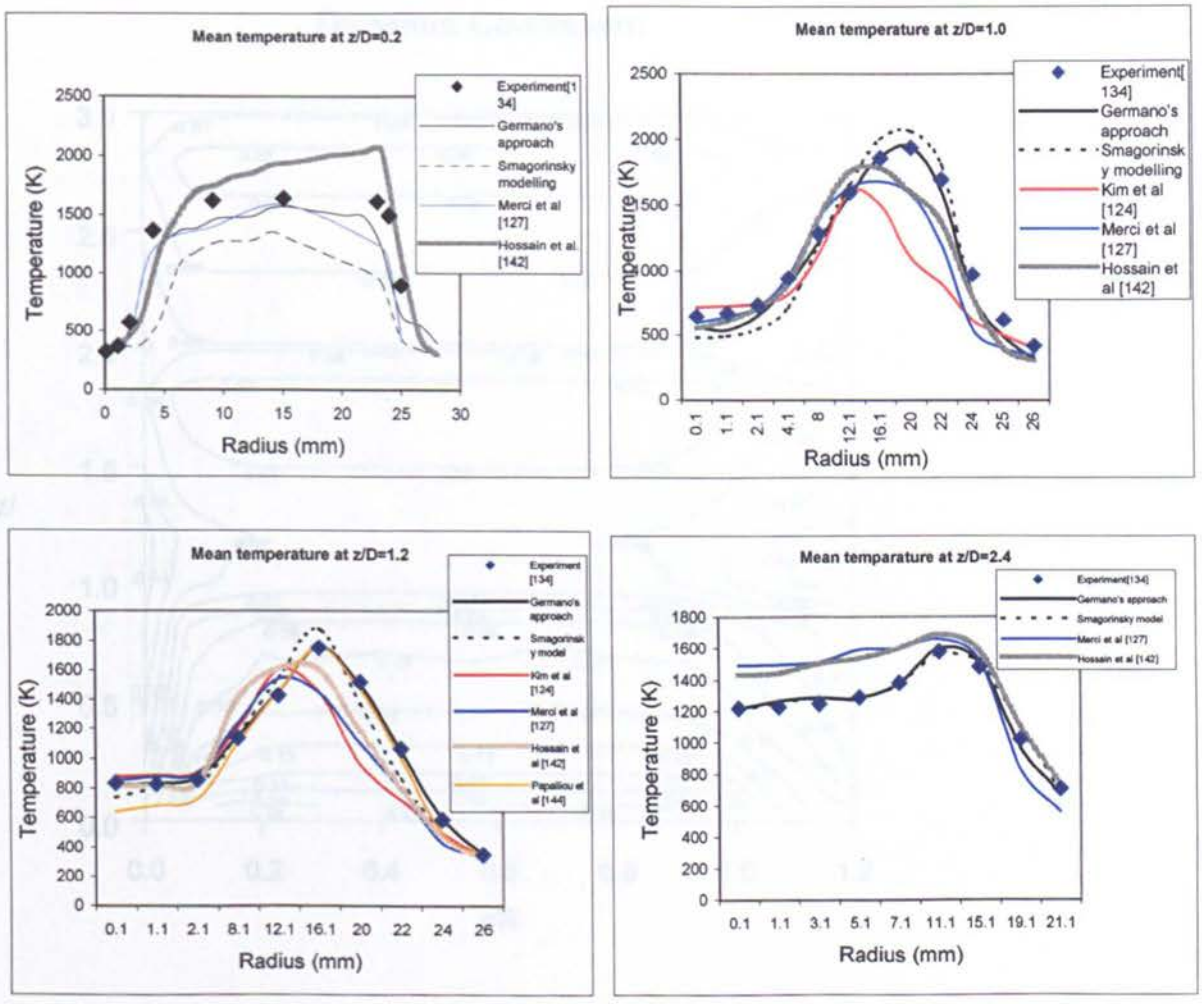
Mean temperature at z/D=0.2
Temperature (K)
Radius (mm)
Experiment[134]
Germano's approach
Smagorinsky modelling
Merci et al [127]
Hossain et al. [142]
Mean temperature at z/D=1.0
Temperature (K)
Radius (mm)
Experiment[134]
Germano's approach
Smagorinsky modelling
Kim et al [124]
Merci et al [127]
Hossain et al [142]
Mean temperature at z/D=1.2
Temperature (K)
Radius (mm)
Experiment [134]
Germano's approach
Smagorinsky model
Kim et al [124]
Merci et al [127]
Hossain et al [142]
Papalliou et al [144]
Mean temparature at z/D=2.4
Temperature (K)
Radius (mm)
Experiment[134]
Germano's approach
Smagorinsky model
Merci et al [127]
Hossain et al [142]

Fig. 5.4

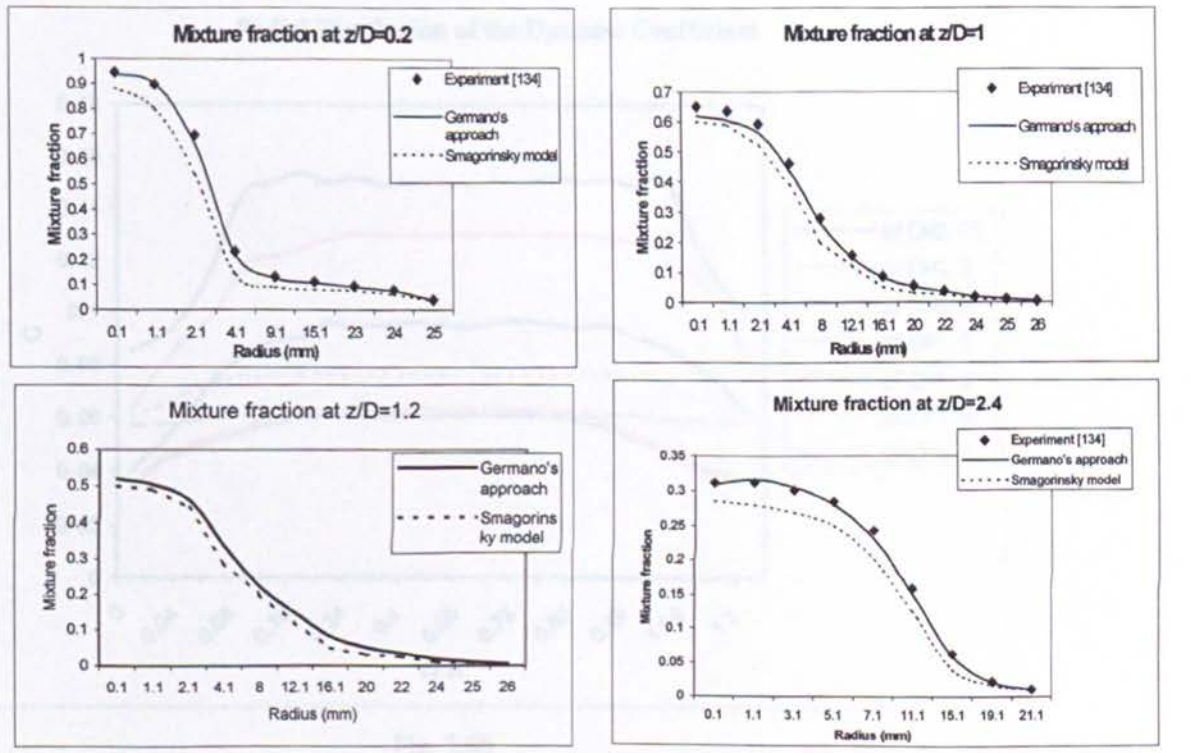
Mixture fraction at z/D=0.2
Mixture fraction
Radius (mm)
Experiment [134]
Germano's approach
Smagorinsky model
Mixture fraction at z/D=1
Mixture fraction
Radius (mm)
Experiment [134]
Germano's approach
Smagorinsky model
Mixture fraction at z/D=1.2
Mixture fraction
Radius (mm)
Germano's approach
Smagorinsky model
Mixture fraction at z/D=2.4
Mixture fraction
Radius (mm)
Experiment [134]
Germano's approach
Smagorinsky model

Fig. 5.5

Dynamic Coefficient

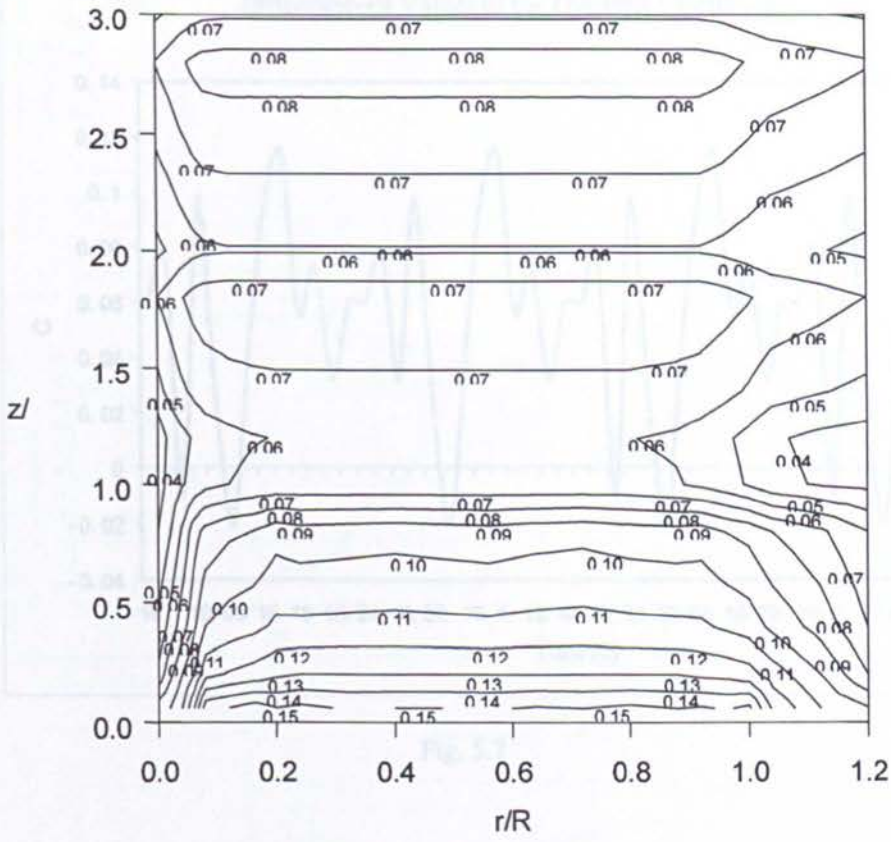

Fig. 5.6a

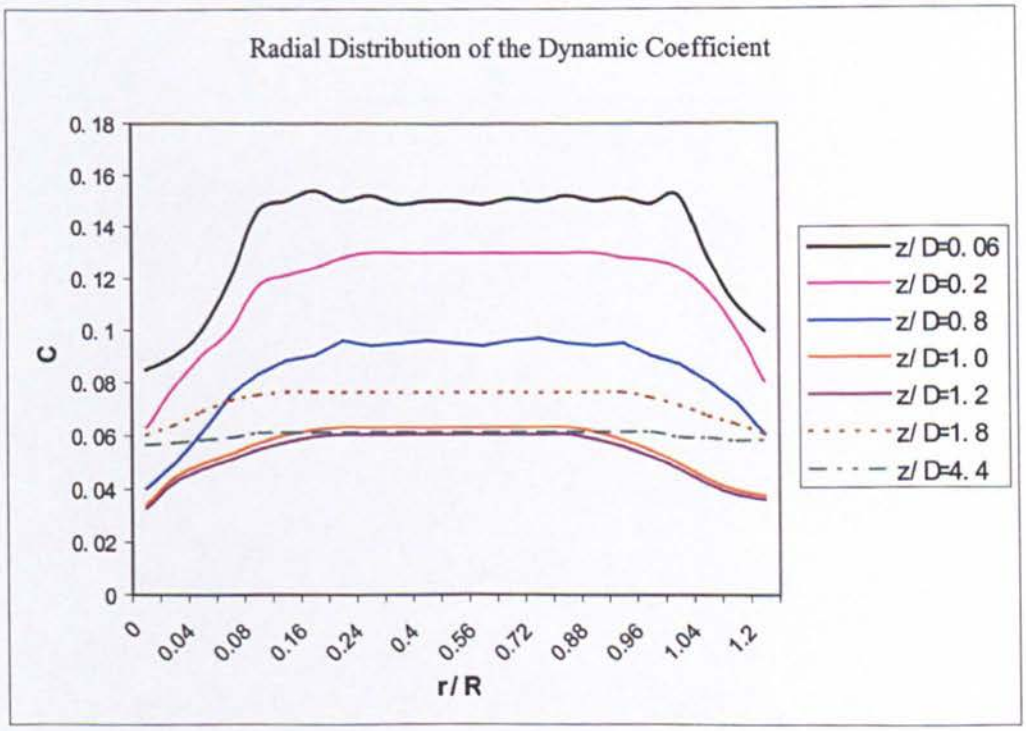

Fig. 5.6b

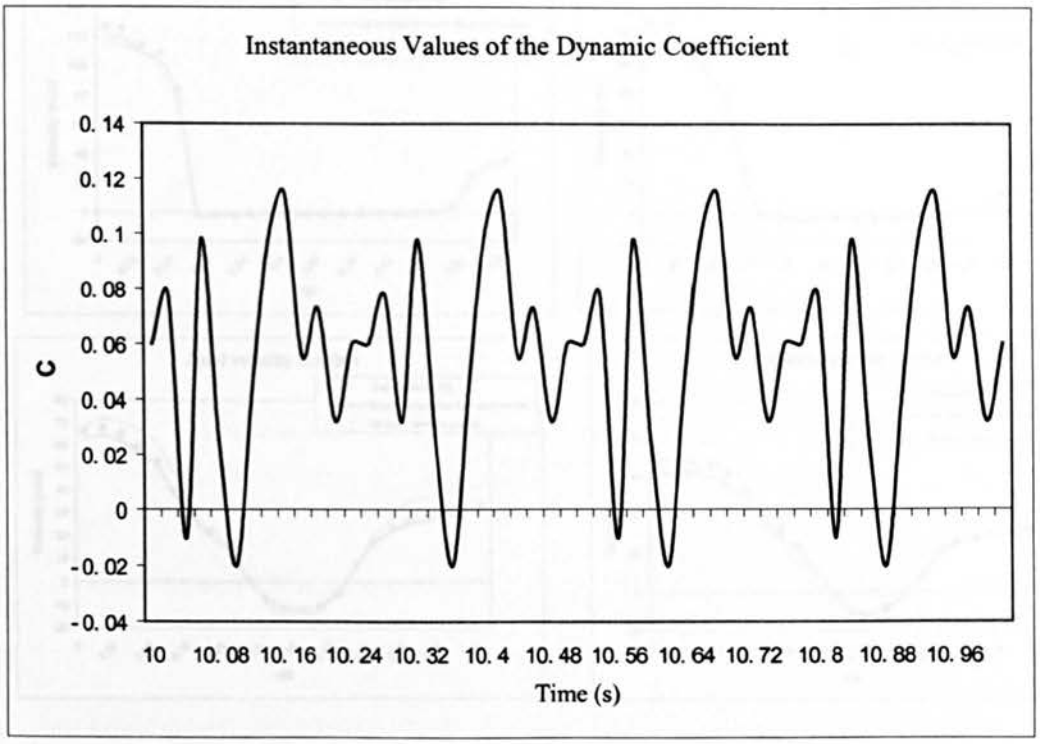
Instantaneous Values of the Dynamic Coefficient
0. 14
0. 12
0. 1
0. 08
0. 06
0. 04
0. 02
0
- 0. 02
- 0. 04
C
10
10. 08
10. 16
10. 24
10. 32
10. 4
10. 48
10. 56
10. 64
10. 72
10. 8
10. 88
10. 96
Time (s)

Fig. 5.7

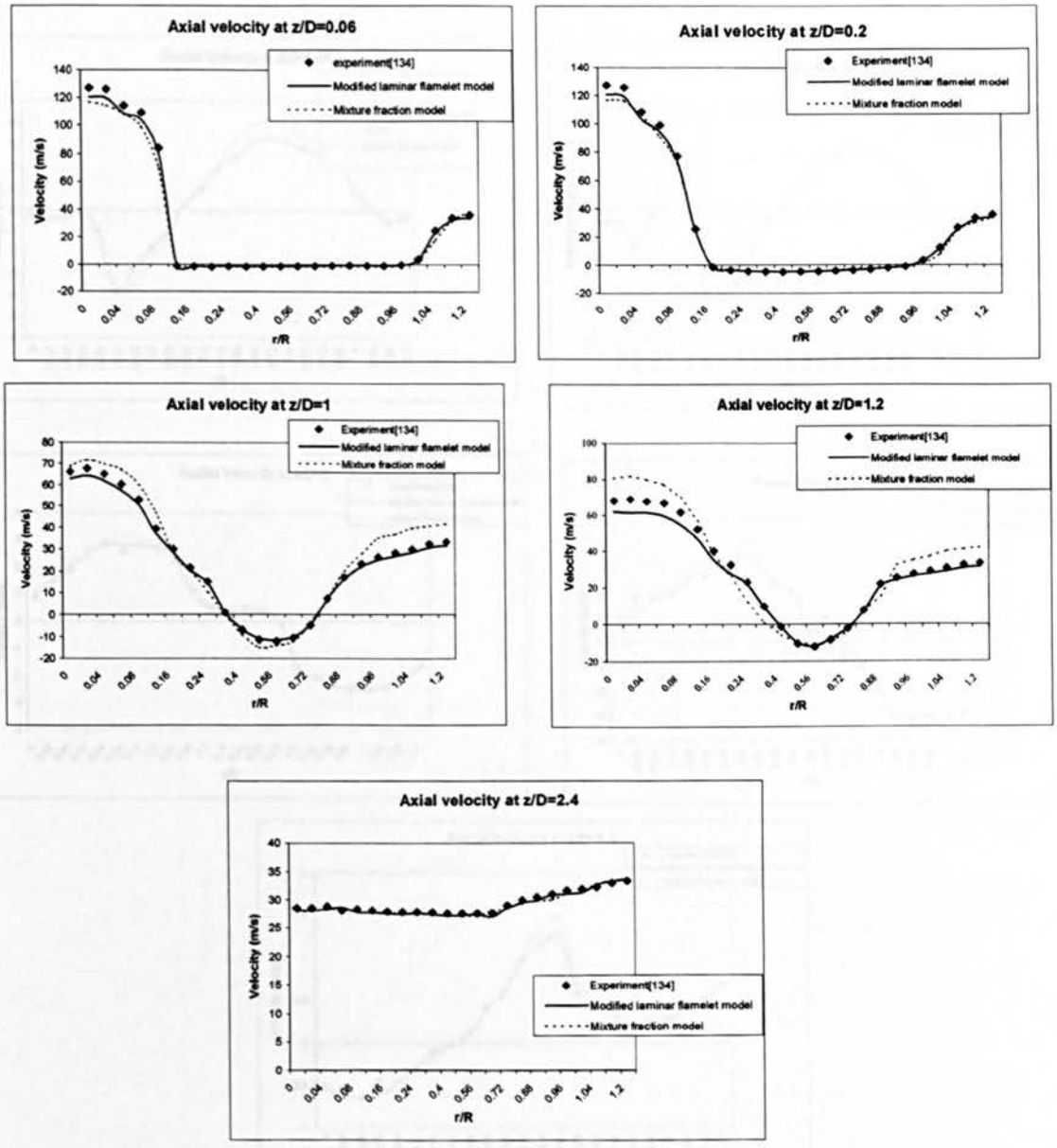
Axial velocity at z/D=0.06
experiment[134]
Modified laminar flamelet model
Mixture fraction model
Velocity (m/s)
r/R
Axial velocity at z/D=0.2
Experiment[134]
Modified laminar flamelet model
Mixture fraction model
Velocity (m/s)
r/R
Axial velocity at z/D=1
Experiment[134]
Modified laminar flamelet model
Mixture fraction model
Velocity (m/s)
r/R
Axial velocity at z/D=1.2
Experiment[134]
Modified laminar flamelet model
Mixture fraction model
Velocity (m/s)
r/R
Axial velocity at z/D=2.4
Experiment[134]
Modified laminar flamelet model
Mixture fraction model
Velocity (m/s)
r/R

Fig. 5.8

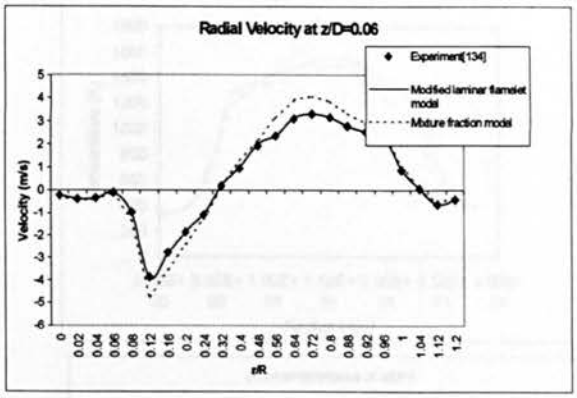
Radial Velocity at z/D=0.06
Experiment[134]
Modified laminar flamelet model
Mixture fraction model
Velocity (m/s)
r/R

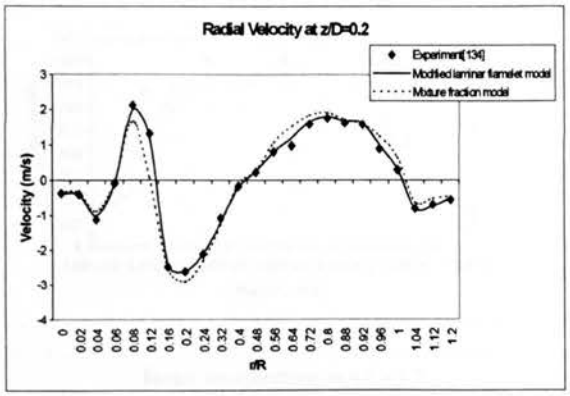
Radial Velocity at z/D=0.2
Experiment[134]
Modified laminar flamelet model
Mixture fraction model
Velocity (m/s)
r/R

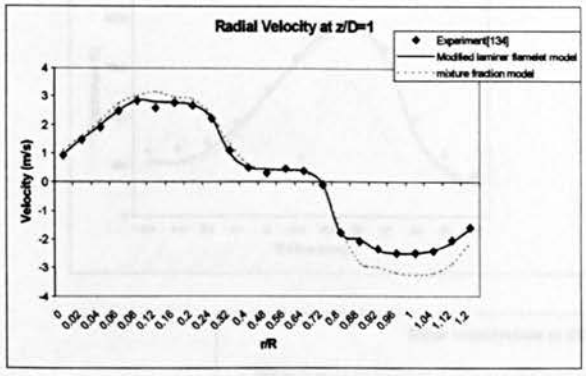
Radial Velocity at z/D=1
Experiment[134]
Modified laminar flamelet model
mixture fraction model
Velocity (m/s)
r/R

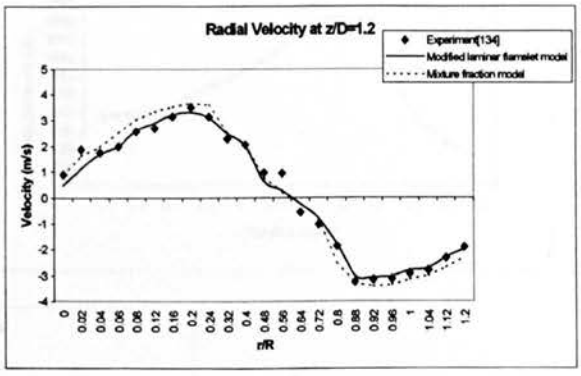
Radial Velocity at z/D=1.2
Experiment[134]
Modified laminar flamelet model
Mixture fraction model
Velocity (m/s)
r/R

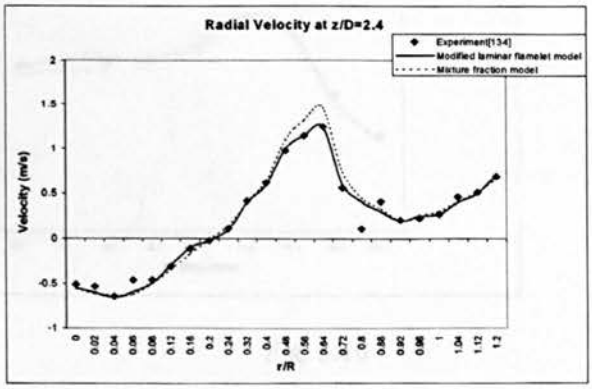
Radial Velocity at z/D=2.4
Experiment[134]
Modified laminar flamelet model
Mixture fraction model
Velocity (m/s)
r/R

Fig. 5.9

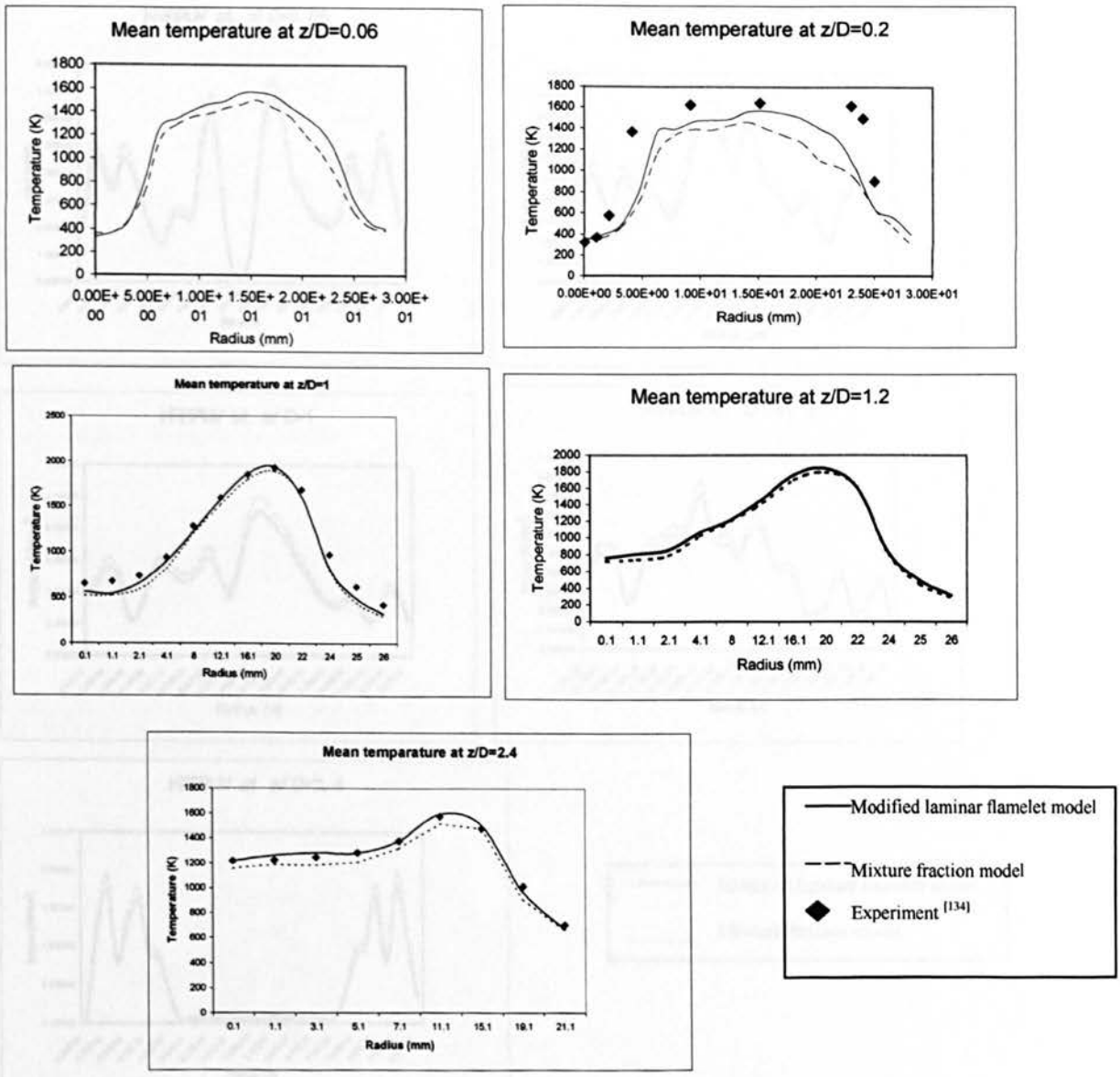
Mean temperature at z/D=0.06
Temperature (K)
Radius (mm)
Mean temperature at z/D=0.2
Temperature (K)
Radius (mm)
Mean temperature at z/D=1
Temperature (K)
Radius (mm)
Mean temperature at z/D=1.2
Temperature (K)
Radius (mm)
Mean temparature at z/D=2.4
Temperature (K)
Radius (mm)
Modified laminar flamelet model
Mixture fraction model
Experiment [134]

Fig. 5.10

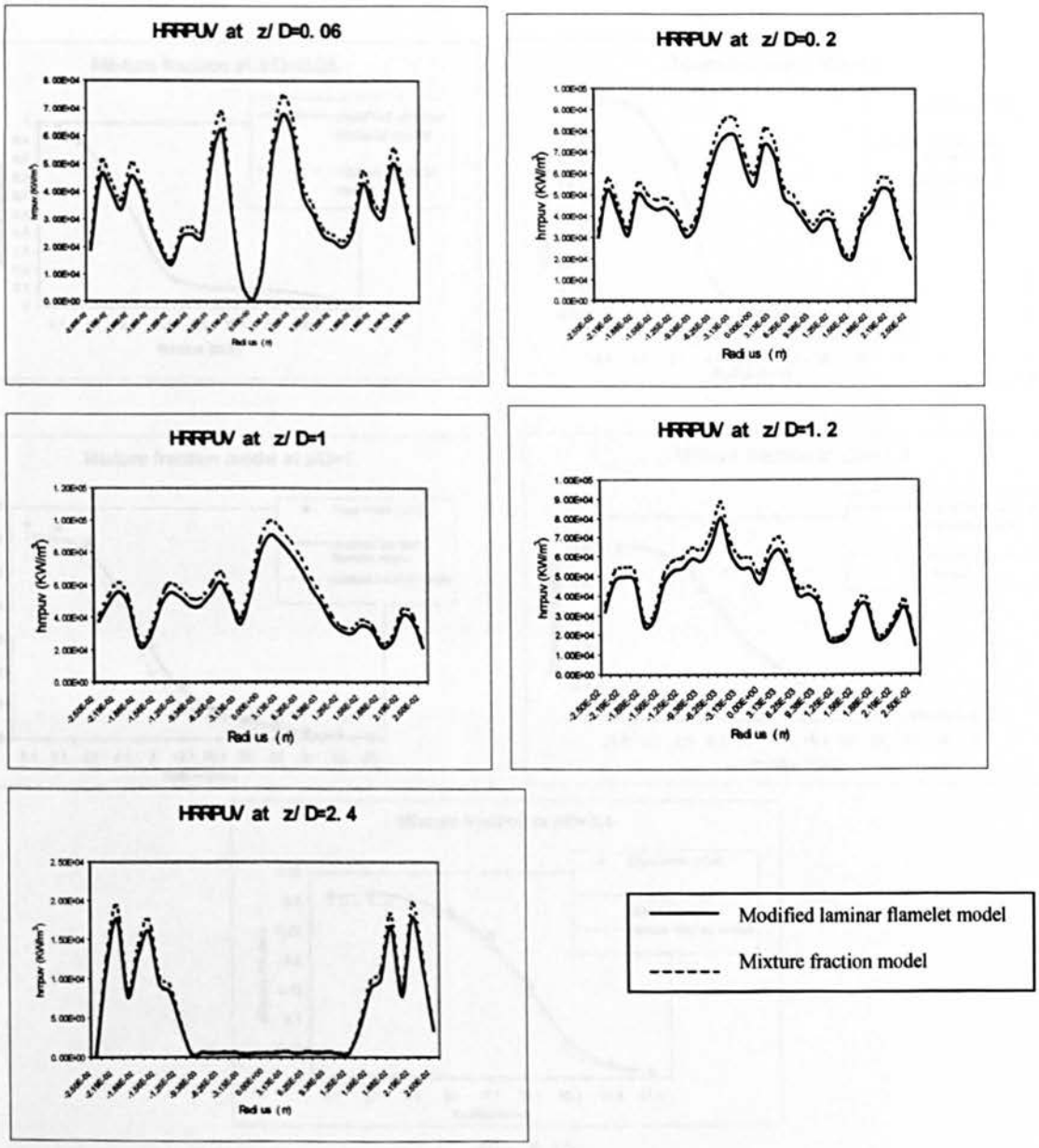
HRRPUV at z/ D=0. 06
HRRPUV at z/ D=0. 2
HRRPUV at z/ D=1
HRRPUV at z/ D=1. 2
HRRPUV at z/ D=2. 4
hrrpuv (KW/m³)
Radius (m)
Modified laminar flamelet model
Mixture fraction model

Fig. 5.11

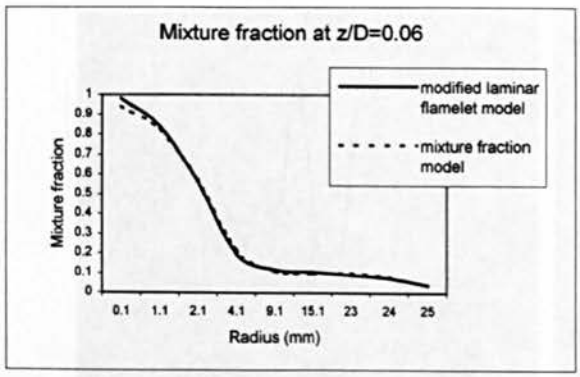
Mixture fraction at z/D=0.06
modified laminar flamelet model
mixture fraction model
Mixture fraction
Radius (mm)

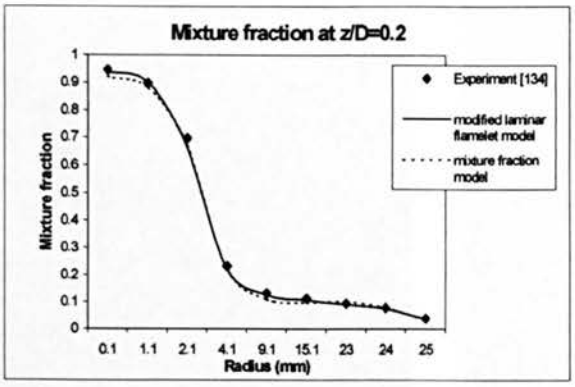
Mixture fraction at z/D=0.2
Experiment [134]
modified laminar flamelet model
mixture fraction model
Mixture fraction
Radius (mm)

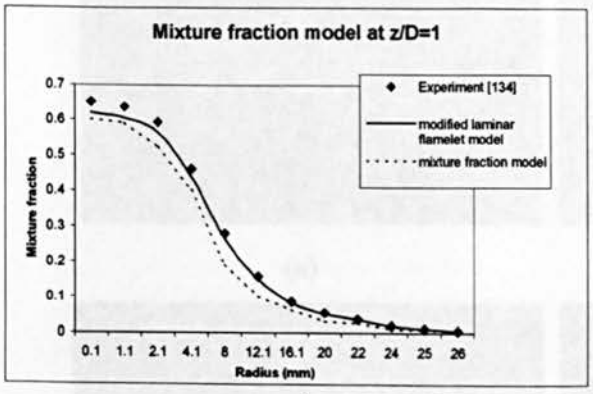
Mixture fraction model at z/D=1
Experiment [134]
modified laminar flamelet model
mixture fraction model
Mixture fraction
Radius (mm)

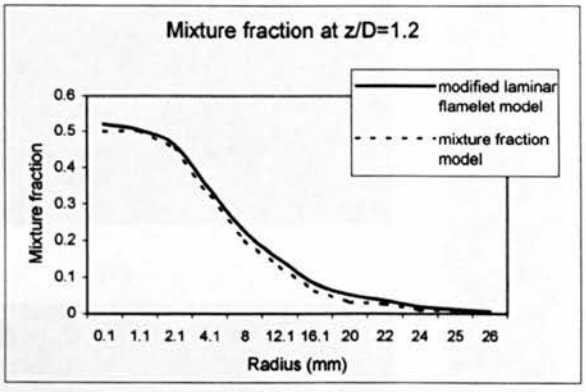
Mixture fraction at z/D=1.2
modified laminar flamelet model
mixture fraction model
Mixture fraction
Radius (mm)

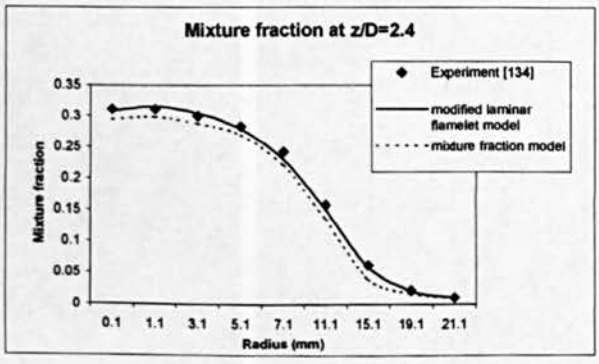
Mixture fraction at z/D=2.4
Experiment [134]
modified laminar flamelet model
mixture fraction model
Mixture fraction
Radius (mm)

Fig. 5.12

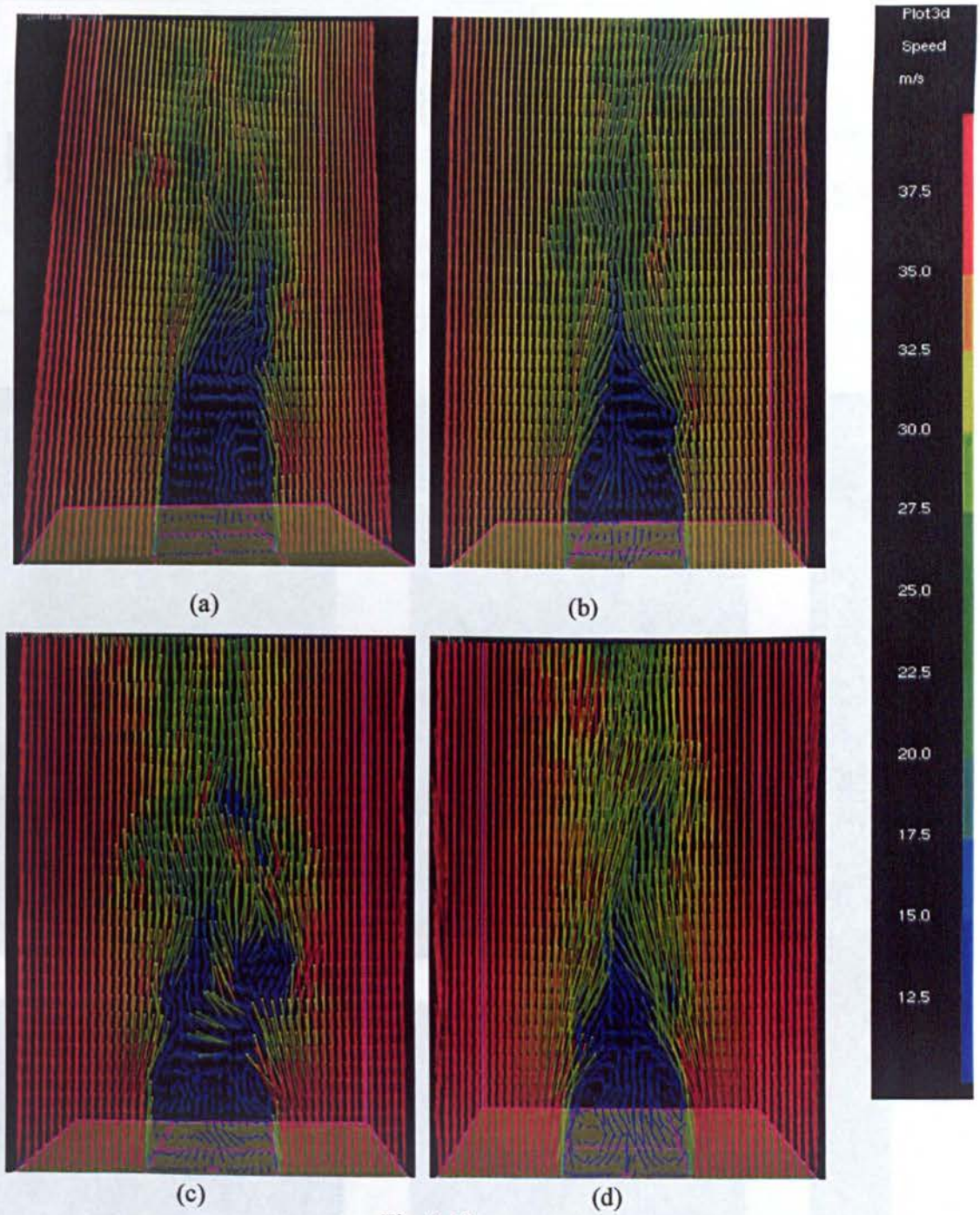

(a) (b)

(c) (d)

Fig. 5.13

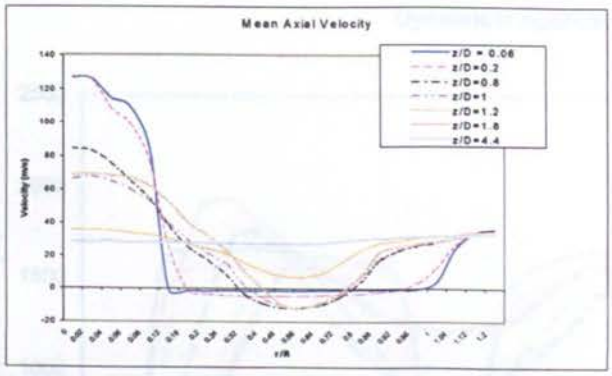

Fig.5.14

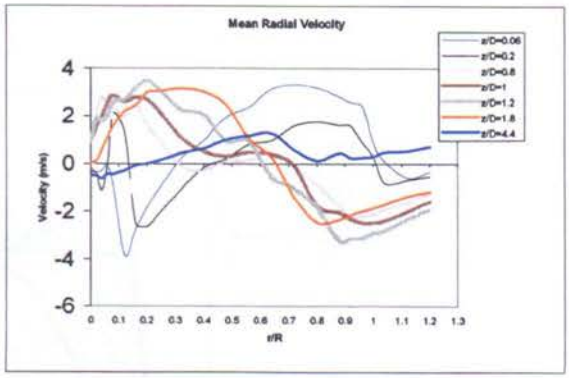

Fig. 5.15

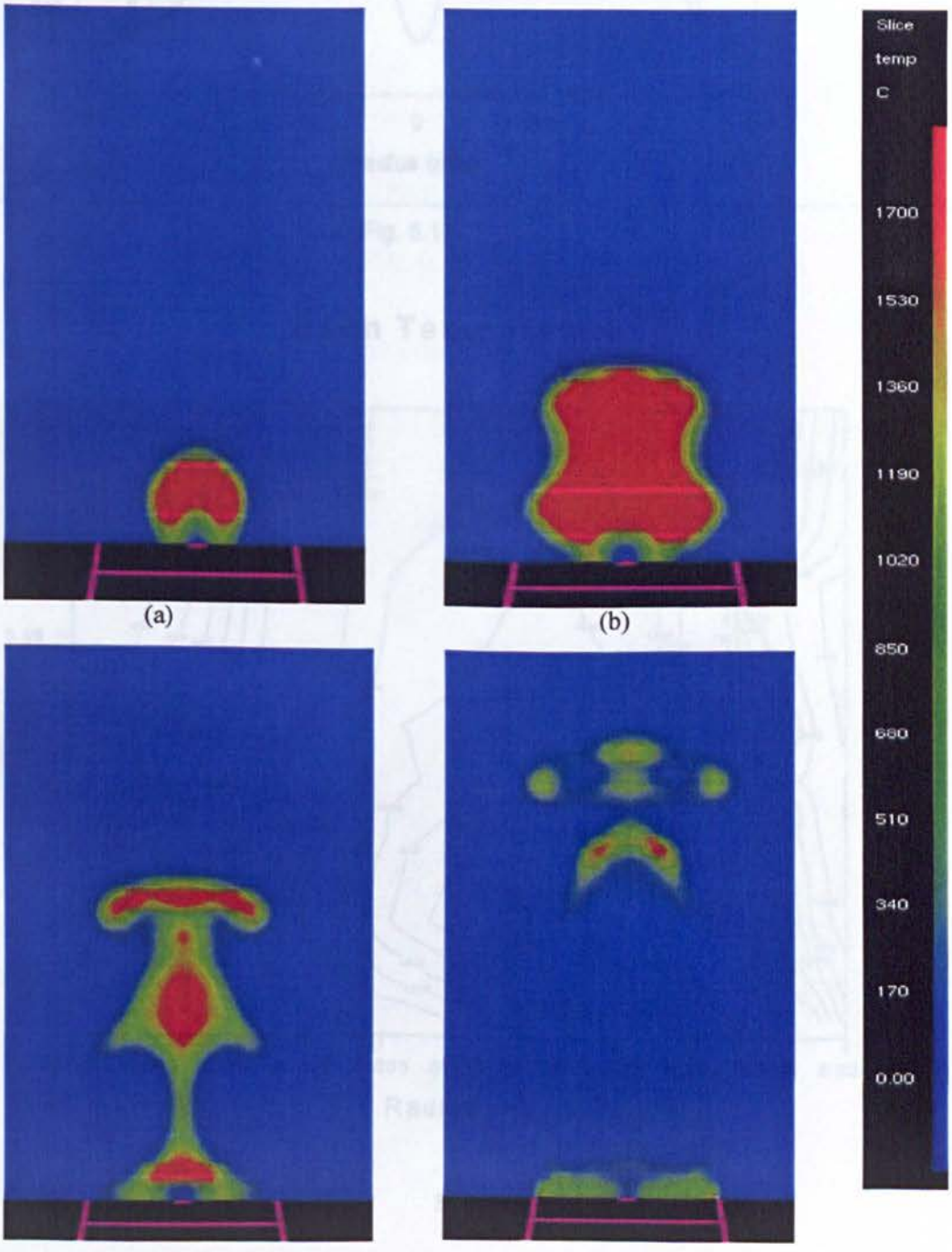

Fig. 5.16

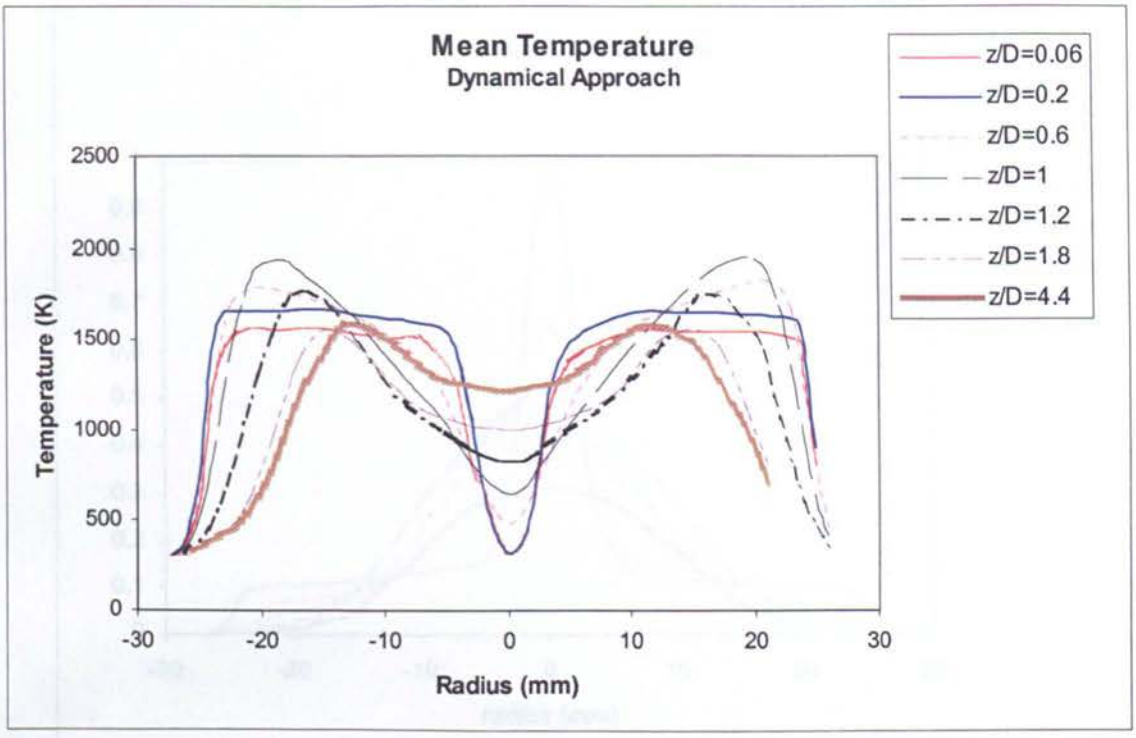

Fig. 5.17

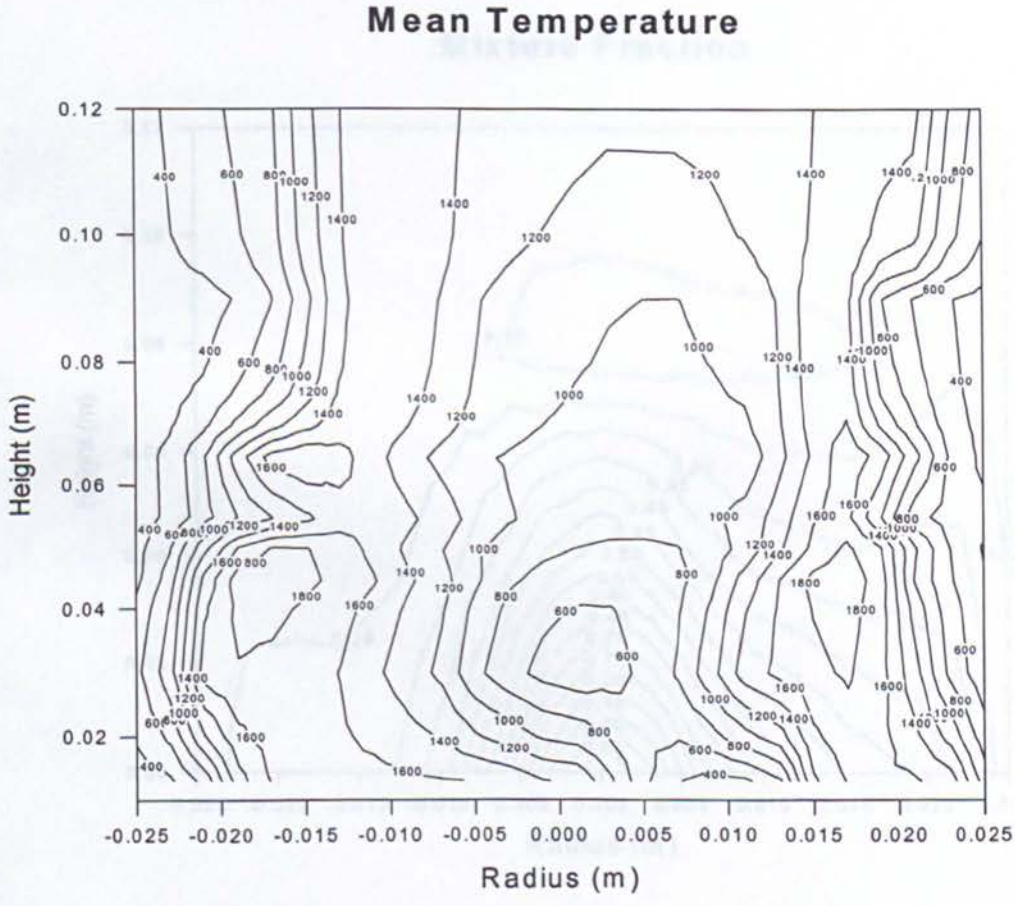

Fig. 5.18

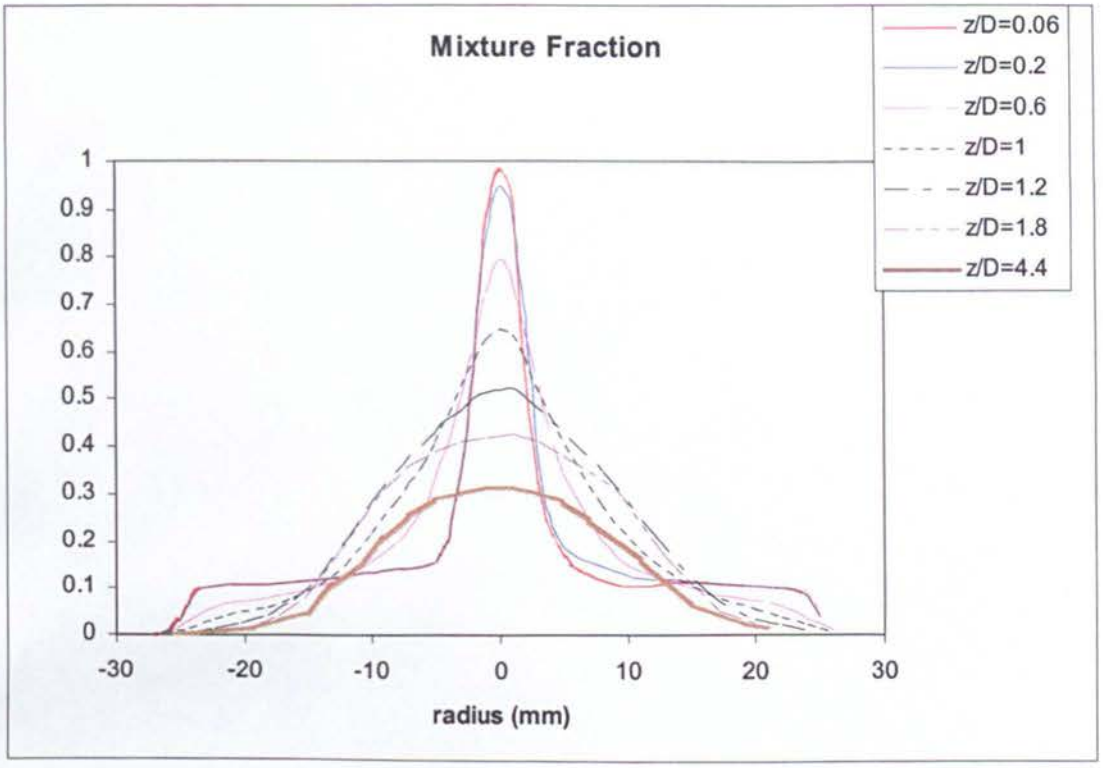

Fig. 5.19

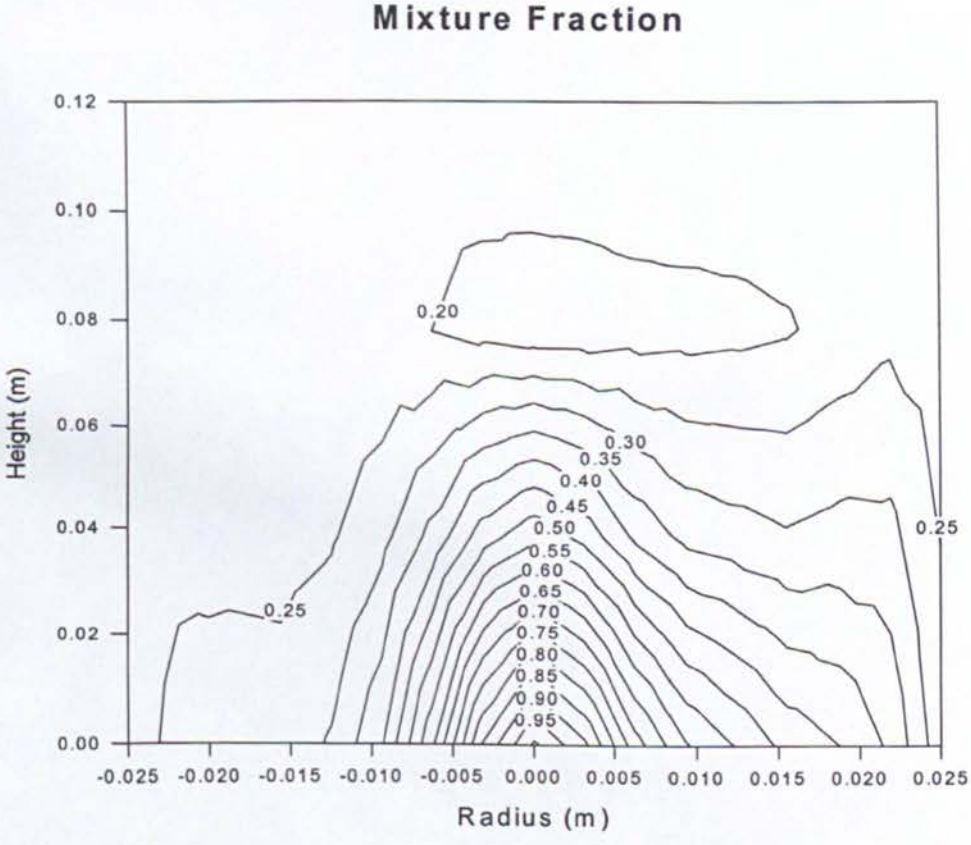

Fig. 5.20